Modelling and development of thermo-mechanical energy storage

Pau Farrés Antúnez
(P. Farres-Antunez)
Department of Engineering
University of Cambridge

This dissertation is submitted for the degree of
Doctor of Philosophy

Peterhouse

September 2018

Modelling and development of thermo-mechanical energy storage

Pau Farrés Antúnez

Pumped thermal energy storage (PTES) and liquid air energy storage (LAES) are two technologies that use mechanically-driven thermodynamic cycles to store electricity in the form of high-grade thermal energy, employing abundant materials that are kept in large insulated tanks. Both technologies are free from geographic constraints, providing a significant advantage over competing methods such as pumped hydro or compressed air energy storage. The focus of this thesis is on the analysis, modelling and development of these technologies.

A number of PTES systems have been proposed based on different thermodynamic cycles. A variant based on the Joule-Brayton cycle employing liquid storage media is studied here. An analytical study is presented that reveals how the performance of the cycle varies along a range of operating conditions. Generally, the same strategies that minimise compression/expansion losses also maximise heat exchanger losses, which results in optimal points at certain operating conditions. A numerical model is developed to find these optima while accounting for real fluid properties. Employing a regenerative heat exchanger is found useful to adapt the cycle to the operating temperature ranges of the storage liquids and to increase the performance of the cycle.

A new combined cycle that integrates PTES and LAES is presented. The fundamental advantage is that the cold thermal reservoirs that would be required by the separate cycles are replaced by a single heat exchanger that acts between them, thereby saving significant amounts of storage media per unit of energy stored. Several configurations are possible and these are studied and optimised. The most advanced configuration reaches a round-trip efficiency of 71 % under nominal conditions, compared to 65 % for stand-alone PTES and 61 % for LAES. A further adaptation of the combined cycle is presented which only employs water and liquid air as storage media, dramatically reducing the cost of energy capacity.

The performance of the heat exchangers is found to have a significant impact on the overall performance of the various cycles. For this reason, an optimisation procedure is developed to obtain heat exchanger designs that minimise entropy generation for a given amount of material. These designs are used when estimating the costs of energy capacity and power capacity of each cycle. Results indicate that the best cycle configurations would be competitive with reported costs for pumped hydro and compressed air energy storage.

A la Montserrat, el Josep Maria, l'Elisenda i la Tamara.

And to all those who believe in and work for
a kinder humankind and a sustainable future.

Declaration

I hereby declare that except where specific reference is made to the work of others, the contents of this dissertation are original and have not been submitted in whole or in part for consideration for any other degree or qualification in this, or any other University. This dissertation is the result of my own work and includes nothing which is the outcome of work done in collaboration, except where specifically indicated in the text and the acknowledgements. This dissertation contains fewer than 65,000 words including appendices, bibliography, footnotes, tables and equations and has less than 150 figures.

Pau Farrés Antúnez
September 2018

Acknowledgements

I would like to acknowledge my supervisor, Dr. Alex White, for inviting me to pursue this extremely interesting project under his supervision, and for his generous help and guidance since the very beginning. I specially appreciate his encouragement, his patience in sharing with me his knowledge and expertise in thermodynamics and engineering, and his prompt and thorough feedback whenever I needed it. I would also like to acknowledge my advisor, Prof. Stewart Cant, who provided me with precious encouragement and advice towards the end of my first year at CUED, and my old supervisor from Oldenburg University, Dr. Konrad Blum, who shared with me his passion for renewable energies and thermal energy storage many years ago and directed me towards the PTES research project at Cambridge.

I would also like to acknowledge the other people in the 'energy storage team', Dr. Caroline Willich, Dr. Josh McTigue and Haobai Xue for the many stimulating discussions about thermodynamics and energy storage, their willingness to help and the good times spent together at CUED and in conferences. I should also acknowledge Haobai for his contribution, as a co-author, in a journal paper on combined PTES and LAES cycles that we have recently published together. Haobai actively participated in the writing of the literature review on stand-alone LAES cycles that appears in the paper and in the first chapter of this thesis (section 1.4.2), and provided me with very useful knowledge regarding the functioning and modelling of LAES cycles. The newest member of the storage team, Antoine Koen, has given me a great lot of extra motivation during these last few months and has given me very useful comments and suggestions on some early drafts of this thesis, for which I am really thankful.

I would like to acknowledge the excellent assistance offered by Kate Graham and Peter Benie on all sorts of administrative and computational issues, respectively, and the great support offered by Sally Swain from the UCS, who introduced me to mindfulness meditation.

On a more personal note, I would like to thank my closest friends at CUED, José, Hans, Stefano, Francesco, Jack, Filip, Sebastian, Andrej, David, Leo, Giulio and Ale, and my friends in Cambridge, Alex, Natalia, Vik, Cris, Bern, Carolina, Bianca, Irene and Michael, without whom the last four years would not have been such a nice and memorable experi-

ence. I would like to give special thanks to Erika Teichert, for encouraging me more than anybody else during the last few months and turning this great challenge into a beautiful episode.

I am equally thankful to my friends in Brazil, specially Clau and the EPE crowd, for showing me an amazing world that I did not know and inspiring me to work for a better one; to my friends in the Basque Country (eskerrik asko por todo, Jone!); and to my friends in Catalonia, in particular Rebeca, Mar, Txus, Ruben, Josep Jaume, Laura, Cristina and Guillem, who make me feel at home every time I go back.

Finally, I could not say how grateful I am to my family, and very specially my wonderful parents and sisters, for their invaluable and unconditional support, encouragement and affection during the last four years and ever before.

Funding

This work was supported by Peterhouse, who provided me with a graduate studentship. Additional funding for travel and conferences was provided both by Peterhouse and the Engineering Department. This support is gratefully acknowledged.

Open source

This research project was performed with the extensive help of several open-source tools. I would like to acknowledge the people and organisations who develop and maintain open-source software, specially: Linux, Ubuntu, LaTeX, LyX, LibreOffice, CoolProp and Mozilla Firefox.

Publications

Some parts of the research contained in and resulting from this thesis have been brought to the public in the form of a journal paper and several conference presentations and posters. As of the date of submission of this thesis, another journal paper (on the topic of heat exchanger optimisation) is being prepared.

Journal paper

P. Farres-Antunez, H. Xue, and A. J. White, "Thermodynamic analysis and optimisation of a combined liquid air and pumped thermal energy storage cycle", *Journal of Energy Storage*, vol. 18, no. Offshore Energy Storage, pp. 90–102, 2018

Conference presentations

P. Farres-Antunez, H. Xue, and A. J. White, "Thermodynamic analysis of a combined pumped thermal and liquid air energy storage cycle", *Offshore Energy and Storage Symposium*, Cape Cod, 2017

P. Farres-Antunez and A. J. White, "A new combined cycle for large-scale energy storage", *Fluids, Energy and Turbomachinery Expo, CUED Graduate Conference*, Duxford, 2017

P. Farres-Antunez and A. J. White, "Thermodynamic strategies for Pumped Thermal Exergy Storage with liquid reservoirs", *UK Energy Storage Conference*, Birmingham, 2016

P. Farres-Antunez and A. J. White, "Optimization of heat exchangers operating with real fluids for thermo-mechanical energy storage", *Offshore Energy and Storage Symposium*, Malta, 2016

Posters

H. Xue, P. Farres-Antunez, A. J. White, “Comparative study of CAES and PTES systems”, *UK Energy Storage Conference*, Birmingham, 2016

P. Farres-Antunez, C. Willich, J. D. McTigue, A. J. White, “Optimisation of Pumped Thermal Energy Storage”, *SolaStor*, London, 2016

Contents

List of Figures

List of Tables

Nomenclature

Symbols

A	Heat transfer area [m^2]
a_L	Friction shape parameter (laminar flow)
A_*	Ratio of cross-sectional areas, $A_\mathrm{m}/A_\mathrm{f}$, see equation (4.26)
A_f	Flow (cross-sectional) area [m^2]
A_m	Material (cross-sectional) area [m^2]
b_L	Heat transfer shape parameter (laminar flow), equal to Nu.
β	Pressure ratio
c_p	Specific heat capacity [J/kg/K]
c_f	Friction coefficient
χ	Round-trip efficiency
D	Hydraulic diameter [m]
∂	Partial deritative
d	Differential
Δp	Pressure drop due to flow friction [Pa]
ΔT	Temperature difference between fluid and channel wall [K]
Δ	Finite increment
δ	Infinitesimal increment

Δp	Pressure loss [Pa]
ΔT	Stream-to-stream temperature difference [K]
e	Specific exergy [J/kg]
ε	Heat exchanger effectiveness, see equation (2.13)
η	Efficiency. Unless otherwise indicated by a subscript, symbol refers to polytropic efficiency, see equation (2.1)
f_p	Fractional pressure loss, see equation (2.22)
G	Mass flux, $\dot{m}/A_{\mathrm{f}}$ [kg/m^2/s]
γ	Ratio of specific heats, c_p/c_v
h	Specific enthalpy [J/kg]
$\mathrm{Q_R}$	Heat to work ratio
h_{t}	Convective heat transfer coefficient [W/m^2/K]
k	Thermal conductivity [W/m/K]
K_*	Dimensionless parameter relating D_1, D_2 and V_{R}, see equation (4.42)
$K_{\Delta p}$	Flow friction parameter [m^3], see equation (4.32)
$K_{\Delta T}$	Thermal resistance parameter [m], see equation (4.32)
K_λ	Axial conduction parameter [1/m], see equation (4.32)
L	Channel length [m]
λ	Axial conduction parameter, see equation (4.54)
$\dot{m}$	Mass flow rate [kg/s]
μ	Dynamic viscosity [Pa·s]
N	Number of channels of a heat exchanger stream
N_s	Entropy generation function (a.k.a. number of entropy units), see equation (4.21)
$N_{s\,\Delta p}$	Component of N_s due to flow friction.

$N_{s\,\Delta T}$	Component of N_s due to thermal resistance.
$N_{s\,\lambda}$	Component of N_s due to axial conduction.
NTU	Overall number of transfer units, see equation (4.51)
Ntu	Single-stream number of transfer units, see equation (4.52)
Nu	Nusselt number, $\frac{hD}{k}$
P	Channel perimeter [m]
p	Pressure [Pa]
ϕ	Polytropic exponent, see equation (2.3)
Pr	Prandtl number, $\frac{\mu c_p}{k}$
ψ	Dimensionless parameter, see equation (2.18)
$\dot{Q}$	Stream-to-stream heat transfer rate [W]
$\dot{Q}_\lambda$	Axial heat transfer rate [W]
R	Gas constant [J/kg/K]
R_t	Thermal resistance [K/W]
Re	Reynolds number, $\frac{GD}{\mu}$
ρ_E	Energy density [J/m^3]
ρ_P	Power density [W/(m^3/s)]
s	Specific entropy [J/kg/K]
$\dot{S}_\mathrm{irr}$	Entropy generation rate [W/K]
σ_max	Maximum allowable stress [Pa]
St	Stanton number, $\mathrm{St} = \frac{\mathrm{Nu}}{\mathrm{RePr}} = \frac{h_\mathrm{t}}{Gc_p}$
T	Temperature [K]
t	Pipe thickness [m]

t_{eff}	Effective thickness [m], see equation (D.2)
$T(\dot{Q})$	Temperature vs. heat transfer diagram
$T(x)$	Temperature vs. distance diagram
τ	In chapter 2, temperature ratio, T_2/T_1
τ	In chapter 4 only, temperature ratio, see equation (4.25)
θ	Temperature ratio, T_3/T_1
v	Specific volume [m^3/kg]
V	Volume [m^3]
V	In chapter 4 only, flow volume of a heat exchanger stream [m^3]
V_{R}	Volume ratio, $V_{\mathrm{m2}}/V_{\mathrm{m1}}$, see equation (4.43)
$\dot{W}$	Work [W]
w	Specific work [J/kg]
$\dot{W}_{\mathrm{L}}$	Lost Work [W]
$\mathrm{W_R}$	Work ratio

Subscripts

x	x-axis (axial) coodinate [m]
0	Ambient (dead state) conditions
1, 2, 3, 4	States of working fluid along the PTES cycle
air, He	Air, helium
c, e	Compressor, expander
C, H	Cold stream, hot stream (of a HEX)
ch, dis	Charge, discharge
cm, hm	Cold storage material, hot storage material
g	Gas (working fluid)

i	Numerical integration step
in, out	Inlet, outlet
is	Isentropic
LA	Liquid air
max	Maximum
min	Minimum
net	Net
opt	Optimal
rev	Reversible
s	Secondary stream

Superscripts

1, 2	Stream 1, stream 2
f	Fluid or flow
i	Component
m	Heat exchanger material (channel walls)
$'$	Discharge

Accronyms

CAES	Compressed air energy storage
CC	Combined cycle
CSP	Concentrated solar power
EGM	Entropy generation minimisation
GT	Gas turbine
HEX	Heat exchanger
LAES	Liquid air energy storage

LNG	Liquefied natural gas
ORC	Organic Rankine cycle
PCM	Phase change material
PHS	Pumped hydroelectrical storage
PTES	Pumped thermal energy storage
TES	Thermal energy storage

Chapter 1

Introduction

1.1 Context: the need for large-scale energy storage

Energy storage technologies have a wide range of forms and cover an equally wide range of applications. They are based on a number of different physical principles and contain energy in vastly different quantities. From tiny to gigantic in size, a few common examples include things as diverse as a mainspring for a mechanical watch, a cell-phone electrochemical battery, a pile of wood for heating and cooking, a biofuel tank for a car engine, a flywheel for frequency regulation, a large hot water tank for district heating, and a large water dam of a hydroelectric facility. They may also operate over very different time-scales (seconds to seasons), they may be portable, stationary or geographically constrained, and they may present very different characteristics in terms of efficiency, cost, energy density, lifetime or environmental footprint, among others [1, 2].

This work focuses on a branch of storage technologies that covers a very specific need: large-scale[1], grid-connected storage for energy management applications. The need for this kind of storage arises from the fact that, in the electrical power network, supply needs to meet demand at all times but production and demand may fluctuate over time [3]. In many traditional power networks, demand fluctuates in relatively predictable diurnal and seasonal patterns and production is adapted to it. The production curve consists of a combination of base-load plants, which have constant power output, with load-following and peaking power plants, which can adapt the power output and be turned on and off as demand requires [4]. Typically, base-load services are provided by nuclear and coal power plants, while load-following and peaking services are provided by natural gas and hydroelectric power plants [5]. However, because they only run part-time or at part load, load-following and peaking

---

[1] Either centralised or distributed, but in overall large quantities.

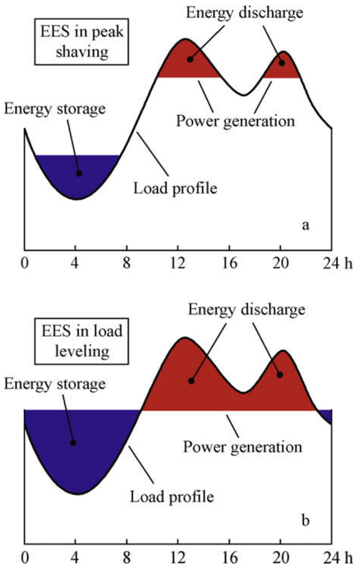

Figure 1.1: Energy storage delivering (a) peak shaving and (b) load levelling services. Reproduced with permission from source: [1].

plants tend to be inefficient, over-sized and expensive [1].

As shown in Fig. 1.1, load-following and peaking services can also be provided by energy storage plants, which consume electricity during demand valleys and transfer it back to the grid during peak demand. The most common technology employed for such application is pumped hydroelectric storage (PHS), which is similar to a normal hydroelectric plant but has two reservoirs (one at the top and one at the bottom) and pumping capabilities between the two. In contrast to dispatchable fossil-fuel plants, energy storage plants have the advantage of presenting no carbon emissions and low marginal costs (since the 'fuel' is bought from the grid during low demand periods). Furthermore, energy storage does not only supply power when it is needed, but also provides value to otherwise unwanted 'excess' power coming from non-dispatchable sources. This feature is particularly important for some renewable sources such as wind and solar energy, which are intermittent in nature. Because of the capability to control their fluctuations, energy storage may play a critical role in facilitating a deeper integration of such sources in modern power networks [6, 7].

During the last decades, growing amounts of renewable energy generation have been deployed worldwide in an effort to reduce greenhouse emissions and improve long-term security of the energy supply [5, 8]. It has been established that anthropogenic greenhouse gas emissions are behind the current rapid changes in climate [9], and historic international agreements are being made to try to limit global warming below 2 °C [10]. Energy consumption from fossil fuels constitutes a major source of greenhouse gas emissions (fossil fuel combustion and industrial processes account for about 65 % of anthropogenic greenhouse gas emissions [9]), while renewable energies offer a safe, clean and sustainable alternative. A number of other economic, environmental, social and political reasons, such as the increasing price of fossil fuels, high levels of pollution, and concerns for energy security are driving new policies in Europe and world-wide that promote and entail the use of renewable energies [10, 11]. Between 2010 and 2016, renewable power plants accounted for more than 50 % of all new installed power capacity, and this value is expected to increase to more than two thirds by 2040 [12].

Although the fluctuating nature of wind and solar energy (which are the two fastest growing renewable sources) poses a significant challenge to balancing production and demand in the power network, it is now well-established that large-scale storage —together with other control strategies, such as grid interconnection and demand response— can significantly contribute to mitigating the effects of renewable energy fluctuations [1, 2, 13]. Strbac et al. estimate that, in an scenario of high penetration of renewable energies (in line with the UK government's commitment to reducing greenhouse gas emissions by 80 % by 2050), having 25 GW of installed energy storage capacity (with 6 hours of storage or more) could amount to whole system savings of around £10bn per year [14]. These would come from various sources, including savings in generation capacity (due to higher security of supply), savings in interconnection, transmission and distribution networks (offsetting the need for further investment and reinforcement) and savings in operating costs (due to higher absorption of renewable generation and displacement of low load factor backup generation). Such values of storage capacity are significantly larger than those present nowadays, since the current accumulated capacity of the storage facilities in the UK adds up to less than 3.5 GW, the vast majority of it in the form of PHS [3, 15].

As mentioned above, this work deals with large-scale energy storage technologies. More specifically, the focus is on two relatively new thermo-mechanical energy storage technologies known as pumped thermal energy storage (PTES) and liquid air energy storage (LAES), and, in particular, the versions of these technologies that store thermal energy in the form of sensible heat, employing liquid storage materials and heat exchangers. The following sections review the current technologies for large-scale energy storage, the principles behind PTES and LAES, the most suitable liquids for thermal energy storage and the most relevant types of heat exchangers. The chapter concludes with a discussion on the aims and scope of this thesis.

1.2 Major large-scale energy storage technologies

Pumped hydroelectric storage (PHS) is by far the most mature and widely adopted large-scale storage technology: with about 130 GW of installed power capacity worldwide (2010 estimate), PHS constitutes around 99 % of the total large-scale energy storage capacity [16]. As shown in the diagram in Fig. 1.2, PHS resembles a production-only hydroelectric power plant but, apart from the upper reservoir, also contains a lower reservoir which stores the discharged water. During charge, the hydraulic turbines are operated in reverse mode, consuming electricity and pumping the water back to the upper reservoir. Typically, PHS has a high round-trip efficiency between 65 % and 85 %, fast response (reaching nominal discharge power in less than 1 min) and very large power and energy capacities [17] (the biggest facilities can reach up to 5 GW, and several facilities support discharge times longer than one day). The main disadvantages of PHS, however, are the limited number of adequate geographical sites and the large footprint of the water reservoirs [1].

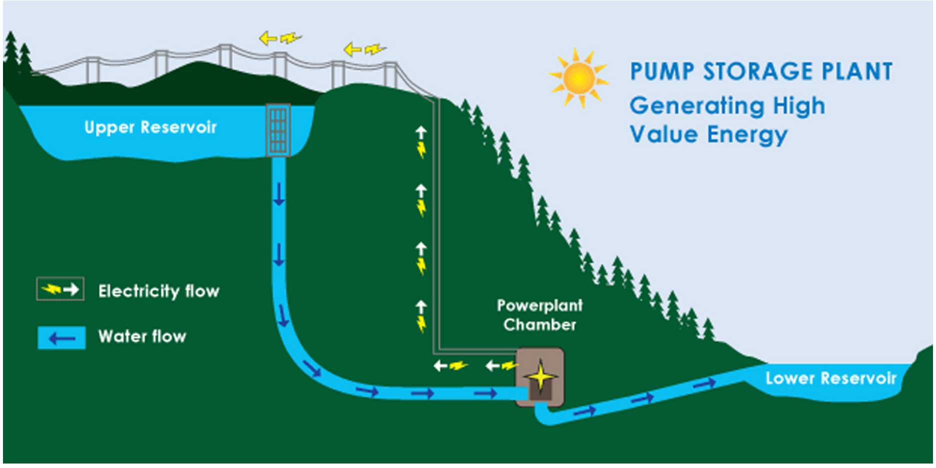

Figure 1.2: Layout of a PHS plant. Reproduced with permission from source: [17].

Another large-scale storage technology which is less mature than PHS but has received considerable attention during the last few decades is compressed air energy storage (CAES). A relatively high number of CAES varieties have been proposed and are being developed [2, 18]. The simplified layout of one of its most common forms, ‘adiabatic CAES’ is shown in Fig. 1.3. Different CAES forms treat the heat derived from the compression process in different ways. The first two CAES projects, built in 1978 and 1991 in Germany and the USA, having power capacities of 290 MW and 110 MW, respectively [19], reject the ‘heat of compression’ to the environment and use combustion from natural gas to heat up the air before expansion during discharge. However, since the combustion process carries CO_2 emissions and increases the operating costs, research is focusing on adiabatic CAES

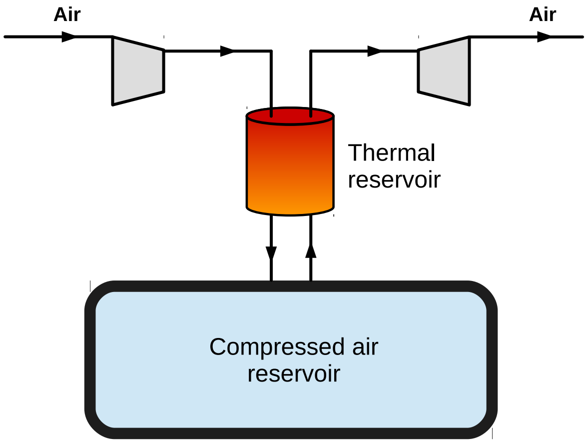

Figure 1.3: Simplified layout of an adiabatic CAES plant. Heat derived from the compression process is stored during charge, and returned to the air stream before expansion during discharge. In practice, two or more compression stages (each followed by thermal energy storage) may be employed before the air enters the reservoir.

[20] (where thermal energy is stored rather than rejected) and isothermal CAES [21] (where the air does not see a significant temperature increase during compression). Furthermore, different CAES schemes may use caverns or artificial tanks where the air is stored at constant volume, or underwater bags [22, 23] where the air is stored at constant pressure, among other options. While the round-trip efficiency of CAES varies considerably between different implementations, it is normally high, with values around $70-80\,\%$. Although the siting restrictions of CAES are not as strict as for PHS (because of the existence of many natural caverns and bodies of water with adequate characteristics), most CAES schemes suffer from geographical constraints at least to some extent, while those that employ artificial reservoirs are expensive due to the high cost per unit volume of high pressure vessels.

Other electrical storage technologies with potential applications for large-scale storage include electrochemical batteries based on several different chemistries and hydrogen energy storage [1, 2, 6, 7]. Electrochemical batteries are being used for energy management applications in some cases, but they are typically characterised by a low cost per unit power and a high cost per unit energy[2], which makes them more suitable for power management applications with shorter discharge times. This is also the case for flywheels, super-capacitors, and other technologies with fast discharge rates. On the other hand, metal-air batteries and hydrogen energy storage display lower costs per unit energy and are better suited for energy management and long-term storage, but they are still in the development

---

[2] According to the reviews in [1, 2, 17], the cost per unit energy of electrochemical batteries does not normally fall below $100-200\,\$/\mathrm{kWh}$, while PHS and CAES may reach values as low as $\sim 10\,\$/\mathrm{kWh}$ and below.

stage and have low round trip efficiencies, around or below 50 %.

Finally, pumped thermal energy storage (PTES) and liquid air energy storage (LAES) are two relatively new technologies with potential for large-scale energy management applications. They use mechanically-driven thermodynamic cycles to store electricity in the form of high-grade (hot and cold) thermal exergy, and fall (together with CAES) in the category of thermo-mechanical energy storage. Although they display lower efficiencies than PHS and CAES, they present higher energy densities and are free from geographical constraints [2, 24], providing a significant advantage in terms of expansion potential.

1.3 Pumped thermal energy storage

1.3.1 Basic principle

Pumped thermal energy storage stores electricity in the form of thermal exergy. The basic principle of the technology is depicted in Fig. 1.4. During charge, an electrically-driven heat pump is employed to transfer thermal energy from a cold reservoir to a hot reservoir. Energy is therefore stored in the form of a thermal potential. The thermal reservoirs are insulated as to minimise losses during the storage period, but leakage losses are normally unimportant for large insulated systems—since losses are proportional to the surface area, but energy content is proportional to the volume. During discharge, a heat engine is operated between the same reservoirs in order to recover the energy stored.

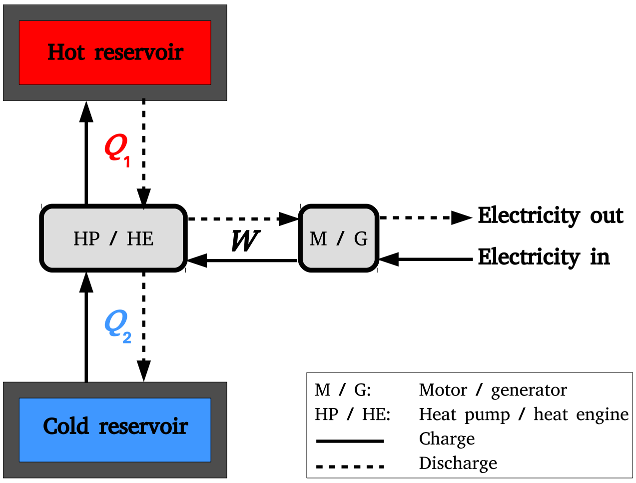

Figure 1.4: Basic principle of pumped thermal energy storage (PTES).

One of the main motivations behind such a scheme is that thermal storage materials provide high storage densities, are cheap and abundant and thus well suited for large-scale applications. The thermal energy may be stored in the form of sensible heat (with several candidate storage materials), or latent heat (typically using phase-change materials – PCMs). In some cases, the environment may also be employed as a heat source or sink, substituting either the hot or the cold reservoir.

One of the features of PTES which is perhaps most counter-intuitive is that, despite the conversion from electricity to heat and back to electricity, the theoretical limit on the round-trip-efficiency is 100 %, independently of the temperature of the thermal reservoirs. It can be easily shown that this is consequence of the round-trip efficiency, χ, being equal to the efficiency of the engine times the coefficient-of-performance (COP) of the heat pump, which are inversely proportional to each other in the ideal, reversible case:

$$\chi_{\text{ideal}} = \text{COP}_{\text{heat pump}} \times \eta_{\text{heat engine}} = \left(\frac{T_{\text{hot}}}{T_{\text{hot}} - T_{\text{cold}}}\right) \times \left(\frac{T_{\text{hot}} - T_{\text{cold}}}{T_{\text{hot}}}\right) = 1$$

In practice, however, the efficiency is affected by several loss mechanisms, the most important ones occurring during the compression, expansion and heat transfer processes that drive the heat pump and heat engine cycles. Therefore, ongoing research is focused on reducing such losses through optimisation of components and optimisation of the cycle operating conditions.

The technology has received growing attention during the last decade, with a number of research groups proposing different cycles under the same basic principle. These are reviewed below, after a brief discussion on the several criteria that are often used to assess the merit of the different cycles.

1.3.2 Rating criteria

The following criteria, among others, are often used to rate PTES systems and other thermo-mechanical energy storage storage technologies:

Round-trip efficiency The round-trip efficiency, χ, measures the fraction of work (W) consumed during charge that is returned during discharge,

$$\chi \equiv \frac{W_{\text{dis}}}{W_{\text{ch}}} \tag{1.1}$$

For an energy storage plant, it is an important index because it defines the minimum cost of the electricity that the plant can supply (during discharge) based on the cost of the electricity that the plant consumes (during charge):

$$\mathrm{C}_{\mathrm{el,\,dis}} = \frac{\mathrm{C}_{\mathrm{el,\,ch}}}{\chi}$$

where C_{el} is the cost per unit of electrical energy. In a power network where a significant part of the energy produced is stored and delivered at a different time, storage plants with high efficiency are preferred in order to avoid having significant overall losses (and a correspondingly larger amount of electricity production for a given electricity demand).

Energy density Energy density is normally defined as

$$\rho_{\mathrm{E}} \equiv \frac{W_{\mathrm{dis}}}{\sum V_{\mathrm{storage}}} \tag{1.2}$$

where the summation is for the volume of the storage tanks (or reservoirs). A high energy density is desirable to reduce the footprint of the plant. Furthermore, the energy density (or rather its inverse) may be sometimes used to provide a preliminary indication of the capital cost per unit of stored energy, since the quantity of storage material, insulation, containment, and space requirements decrease with increasing ρ_{E}. Apart from choosing storage materials with high density and high specific heat capacity, ρ_{E} can generally be improved by storing the thermal energy at very high temperatures (hot reservoir) and/or very low temperatures (cold reservoir).

Power density The power density is normally defined as

$$\rho_{\mathrm{P}} \equiv \frac{\dot{W}_{\mathrm{dis}}}{\dot{V}_{\mathrm{max}}} \tag{1.3}$$

where $\dot{W}$ denotes the power output and $\dot{V}_{\mathrm{max}}$ is the maximum volumetric flow rate of the working fluid along the cycle. A high power density is desired because it is associated with more compact (and generally cheaper) conversion devices.

Work ratio Most thermodynamic cycles consist of at least one compressor and one expander acting simultaneously. For a heat engine, the work ratio W_{R} is defined as the combined expander work output over the combined compressor work input,

$$\mathrm{W}_{\mathrm{R}} \equiv \frac{\sum W_{\mathrm{e}}}{\sum W_{\mathrm{c}}}$$

and vice-versa for a heat pump. For many cycles, only one compressor and one expander are present, and the summation signs become redundant. The net work (during discharge) is related to the work ratio by:

$$W_{\mathrm{net}} = \sum W_{\mathrm{e}} - \sum W_{\mathrm{c}} = (\mathrm{W_R} - 1) \sum W_{\mathrm{c}}$$

Therefore, a low work ratio should be avoided because it means that much larger machines are required to produce a given net work. Furthermore, a low $\mathrm{W_R}$ means that large amounts of work are being 'processed' for a given amount of net work, which increases the impact of compression/expansion losses on the efficiency of the cycle. In the case of a PTES cycle, it is possible to prove that the work ratio sets a maximum round-trip efficiency given by [25, 26]:

$$\chi_{\mathrm{max}} = \frac{\mathrm{W_R}\, \eta_{\mathrm{is}}^2 - 1}{\mathrm{W_R} - \eta_{\mathrm{is}}^2}$$

where η_{is} is the isentropic efficiency of the compressors and expanders. Note that $\chi_{\mathrm{max}} = 0$ when $\mathrm{W_R} = 1/\eta_{\mathrm{is}}$, and $\chi_{\mathrm{max}} = \eta_{\mathrm{is}}^2$ when $\mathrm{W_R} \to \infty$, which highlights the importance of having both a high work ratio and high-efficiency compressors and expanders.

Heat to work ratio A less often encountered but also important index is the heat to work ratio, $\mathrm{Q_R}$, which measures the amount of heat that is processed for a given amount of net work:

$$\mathrm{Q_R} = \frac{\sum |Q|}{W_{\mathrm{net}}}$$

where $\sum |Q|$ includes the contributions from all heat transfer processes in the cycle[3]. Generally, high heat to work ratios are not desired because they imply larger heat exchangers for a given performance and a given net work. High values of $\mathrm{Q_R}$ are also normally linked to low values of ρ_{E}, because more thermal energy needs to be stored per unit net work, which implies larger amounts of storage material needed.

Specific capital cost Apart from the thermodynamic criteria, there are also economic criteria which play an important role in determining the potential success of a given storage system. Two economic indices that are very often encountered in the literature are the cost per unit power capacity (typically \$/kW) and the cost per unit energy capacity (\$/kWh).

---

[3] Depending on the purpose, $\sum |Q|$ may be defined to include only those heat transfer processes linked with the hot and/or cold reservoirs, excluding any heat exchanged with the environment or within any regenerator in the cycle.

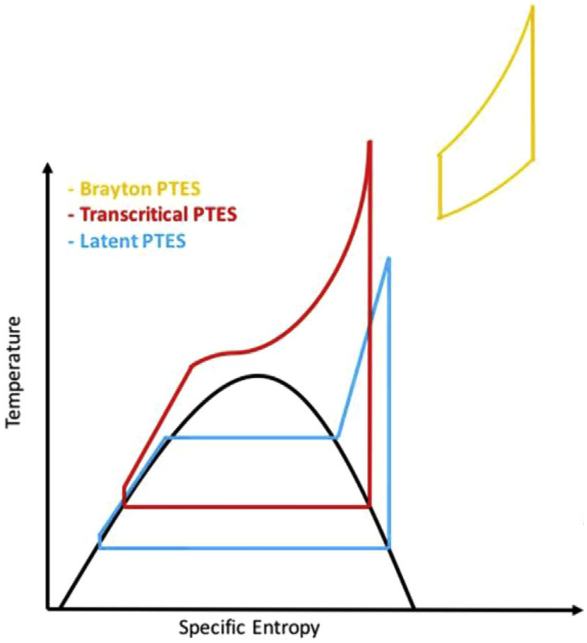

Figure 1.5: Ideal T-s diagrams (not to scale) of the three major cycles used for PTES systems: Joule-Brayton (yellow), Rankine (blue) and transcritical (red). Reproduced with permission from source: [28].

1.3.3 Review of major studies and proposed implementations

PTES systems can be broadly divided in three groups depending on the type of cycle that they are based on, although several variations have been proposed within each category: (i) Joule-Brayton (supercritical) cycles, (ii) Rankine (subcritical) cycles and (iii) transcritical (part supercritical, part subcritical) cycles. Representative T-s diagrams of the three categories are shown in Fig. 1.5. This section provides a review of the major systems in each category. For a more in-depth survey, the reader is referred to the recent review by Benato [27].

Joule-Brayton In the Joule-Brayton implementations of PTES, the working fluid always remains in the gas phase, and thermal energy is stored in the form of sensible heat. An example plant layout and T-s diagram are shown in Fig. 1.6. In this simple configuration, a compressor and an expander are used to drive a high temperature-ratio heat pump during charge, and a heat engine during discharge. The thermal energy is stored in the hot and cold stores, and two external heat exchangers (denoted A and B) are used to reject heat – which is derived from irreversible processes – during discharge.

Joule-Brayton PTES systems using argon as the working fluid have been proposed by

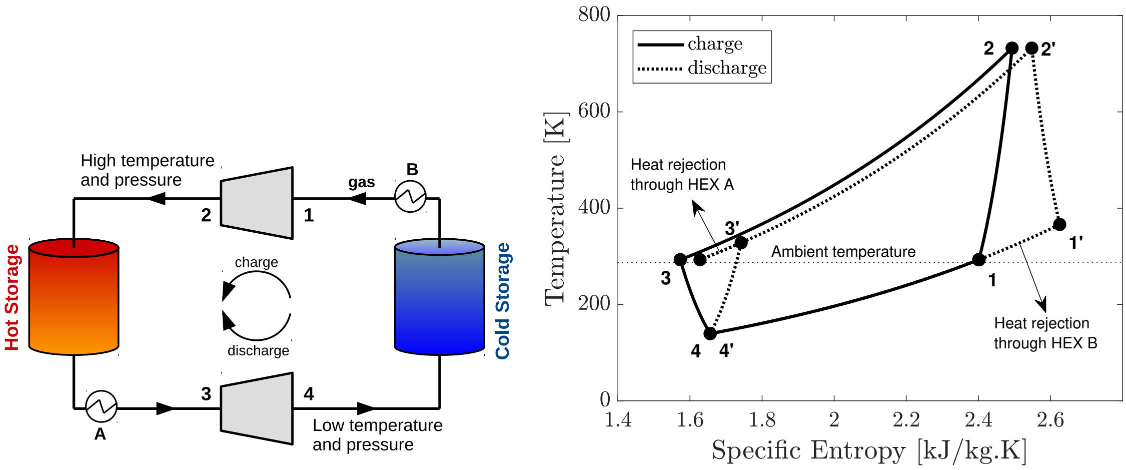

(a) Plant layout.

(b) T-s diagram.

Figure 1.6: Plant layout and T-s diagram of a Joule-Brayton PTES system employing solid storage media. In (a), arrows indicate the direction of the working fluid during charge. The gas flows in the reverse direction during discharge, which in practice requires another set of turbomachines (unless reciprocating devices are employed, in which case the same compressor and expander may be run backwards). In (b), cycle direction is 1-2-3-4-1 during charge and (1'-4'-3'-2'-1') during discharge.

Desrues et al. [29] (using turbomachinery) and Howes [30] (using reciprocating devices[4]). Simple cycle analysis of these systems (e.g., [25]) shows that they are particularly susceptible to compression and expansion losses because of the low work ratios inherent to the Joule-Brayton cycle. The mentioned systems use solid storage media such as packed beds or matrices of refractory materials. Argon (or another monatomic gas) is preferred to air in these schemes because its higher ratio of heat capacities means that a given temperature ratio can be achieved with a smaller pressure ratio; this is advantageous because the storage tanks need to be pressurised to the same pressure as the working fluid [25].

Storing the sensible heat in packed beds of solid particles is advantageous because the filling materials are cheap, can be operated over wide temperature ranges and present a large surface area available for heat transfer. On the other hand, thermal fronts propagate along the tanks as the system charges and discharges. The thermal fronts, which are a naturally unsteady process, make the operation of the system relatively complex, reduce the maximum utilisation of the tanks and increase self-discharge losses during storage periods. Analyses of these effects and numerical optimisation of packed beds for PTES applications, including the analysis of segmented reservoirs, have been presented by White and McTigue

---

[4] One of the potential advantages of using reciprocating devices is that the same machines may be used as both compressors and expanders by adjusting valve timings, thereby saving on the total number of components and allowing faster reversal between charge and discharge.

et al. [31–35]. A trade-off between exergetic efficiency and utilisation of the packed-beds (which is proportional to energy density) is found in those works, as well as in the analytical study by Ni and Caram [36].

An economic analysis of Joule-Brayton PTES has been presented by Smallbone et al. [37]. The analysis uses data from the development of a demonstration plant (not yet commissioned) which is based on the system described in [30]. The plant employs packed beds as storage media and reciprocating devices as compression and expansion machinery. The study finds that PTES can achieve costs per unit power and costs per unit energy which are comparable to PHS and CAES.

Joule-Brayton PTES cycles may also use liquid storage media and gas-to-liquid heat exchangers instead of solid (direct heat exchange) reservoirs, as proposed by Farres-Antunez [38–43] and Laughlin [44]. Doing so allows the gas circuit to be pressurised (thereby increasing power density) whilst keeping the reservoirs at ambient pressure (thereby reducing cost per kWh storage relative to pressurised packed-beds). Each storage tank is also kept at a single temperature, thus avoiding thermal equilibration (mixing) losses during long storage periods. A regenerative heat exchanger may also be incorporated into the cycle in order to adapt cycle temperatures to suit different liquid storage media (which have more limited temperature ranges than most solid materials). Regeneration also has benefits in terms of efficiency and energy and power density, as it increases the work-ratio. Further details of regenerative PTES, including an assessment of thermodynamic, economic and safety aspects, are given in a recent paper by Laughlin [44].

Depending on the cycle operating conditions and on the assumptions of component performances, the previous Joule-Brayton PTES systems have round-trip efficiencies ranging between 55 % and 70 %.

Rankine A PTES system based on the steam Rankine cycle was proposed by Steinmann [24, 45]. The cycle, shown in Fig. 1.7, has a much higher work ratio (> 20) than the Joule-Brayton schemes (typically around $2-4$), meaning that the round-trip efficiency is less affected by compression/expansion losses. Furthermore, the system uses the environment as heat source during charge and heat sink during discharge, meaning that a cold thermal store is not needed. On the other hand, because of the extremely low vapour pressure of water at temperatures below ambient temperature, it is not practicable to use the environment as a direct heat source for the evaporator during charge, and a secondary ammonia heat pump – acting between the environment and the ‘reverse-Rankine’ heat pump – is required. Because of the phase change between water and steam at the high pressure side of the cycle, thermal energy is stored both in the form of sensible heat and in the form of latent heat. The

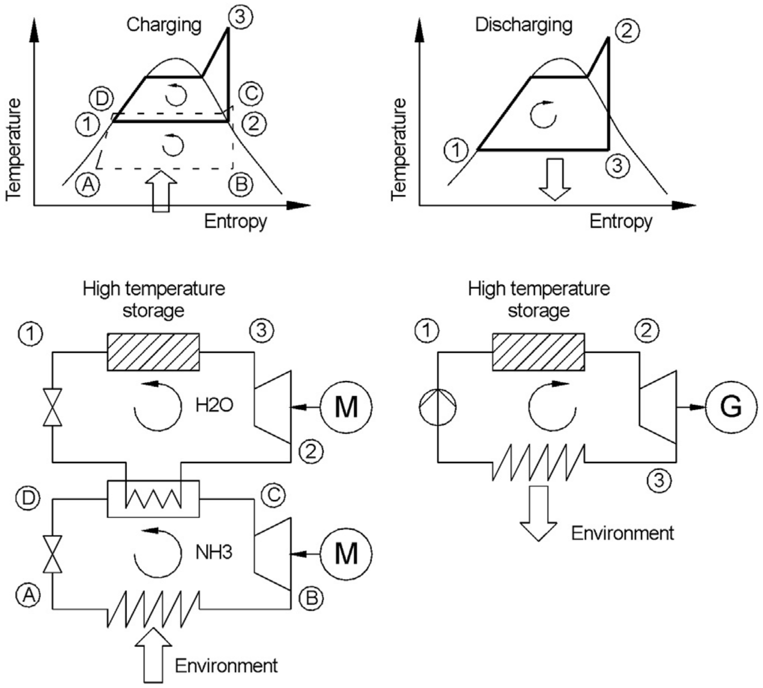

Figure 1.7: Rankine-based PTES system, employing a secondary ammonia heat pump during charge to absorb heat from the environment. The high temperature storage system consists of three different stores, one storing latent heat and two storing sensible heat. Reproduced with permission from source: [45].

main disadvantage of current latent heat storage units (consisting of phase-change materials – PCMs – with embedded heat exchangers) is that they prevent an independent sizing of power and energy capacity. However, alternative PCM pumping strategies which have the potential to overcome this drawback are being investigated [46, 47]. The cycle is estimated to have an efficiency around 70 %.

A number of other PTES systems have also been proposed which are based on organic Rankine cycles (ORCs) [48–52]. Such systems can normally be built in small units for distributed generation and have low material requirements (because they have maximum temperatures around 150 °C or below), but obtain significantly lower performances unless they are coupled with an external source of heat or cold.

Transcritical At least two types of transcritical PTES systems have been proposed so far, one using carbon dioxide (CO_2) and one using ammonia (NH_3) as working fluid. The transcritical cycles resemble the Rankine cycle in that they have an evaporation/condensation phase at the low pressure side, but, because they reach supercritical conditions, they do not display a phase-change at the high pressure side. This allows the thermal energy to be stored fully as sensible heat in the hot reservoir.

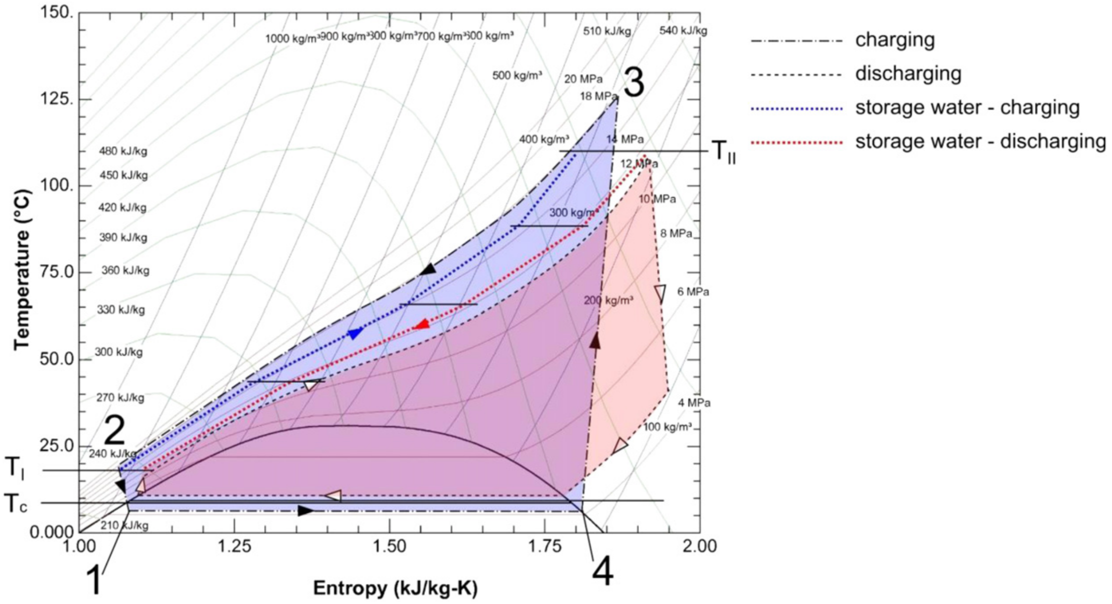

Figure 1.8: T-s diagram of a transcritical CO_2 PTES cycle. Reproduced with permission from source: [53].

A T-s diagram of the CO_2 implementation, proposed by Morandin and Mercangöz et al. [53–56], is shown in Fig. 1.8. The cycle operates over low temperature ratios, which have the disadvantage of a low energy density and a higher impact of heat-exchange losses, but allow the use of inexpensive storage media such as hot water. The environment can in principle be used as source/sink for the evaporation/condensation phases, but it has also been suggested to use a salt-water/ice slurry as cold store. This has the effect of lowering the bottom temperature and improving the work ratio, which lies somewhere between the values of the Joule-Brayton and the Rankine cycles.

One general disadvantage of the transcritical cycles is that the working fluid experiences strong specific heat capacity variations when being heated up/cooled down along the supercritical isobar. This makes the heat transfer process in the heat exchanger less efficient, although it can be partially counter-acted by having different levels of mass flow rate of the storage fluid, as shown in Fig. 1.8. The CO_2 PTES cycle is expected to have an efficiency around 60 % [54]. Comparisons between efficiencies claimed for different PTES systems in the literature must be taken with caution, however, as different authors base their calculations on different assumptions. Other studies done on the CO_2 PTES cycle include: (i) a thermo-economic analysis by the same authors [56], (ii) an analysis that proposes employing an isothermal compression/expansion stage and a regenerative process instead of the adiabatic compression/expansion stage, by Kim et al. [26] , (iii) an experimental study by Tauveron et al. [57] and (iv) several other parametric and control studies [58–61].

The NH_3 implementation, proposed by Abarr et al. [28, 62], operates at higher temperatures and is designed to be able to function either independently or as a bottoming cycle coupled to a gas peaker plant. The authors suggest employing blocks of concrete (with an embedded heat exchanger) as thermal reservoir, and present experimental results of the thermal stores that are used to validate the numerical method that they employ to study the performance of the plant, which achieves stand-alone storage efficiencies between 51 % and 66 % under varying levels of power rate and utilisation of the stores.

1.4 Liquid air energy storage

1.4.1 Classification

Liquid air energy storage (LAES) is a technology highly related to PTES, in the sense that it stores energy in the form of thermal exergy and that it is geographically unconstrained. The main difference between the two is that, while in PTES the working fluid flows in a closed circuit, in LAES the working fluid (air) is used both as a working fluid and as storage medium. Despite this difference, some authors (such as Steinmann [24] and McTigue [34]) consider that LAES can be understood as a special form of PTES operating at cryogenic temperatures. Other authors (such as Kantharaj et al. [63] and Budt et al. [18]), on the other hand, point out that LAES is also very related to CAES, since the first stage of both systems consists of the compression (to high pressures) of atmospheric air. In this sense, LAES may also be understood as a variant of CAES where, after compression, the air is not stored right away but cooled down and liquefied instead.

The following brief review on LAES is an adaptation of the review presented in [43], which was written in collaboration with Xue and White.

1.4.2 Basic principle and review

Liquid air energy storage, as the name suggests, involves liquefying air so that it can be stored at near-ambient pressure in insulated tanks. One possible implementation, shown in Figure 1.9, resembles the Linde cycle with the addition of ‘cold recycling’, as described below. During charge, air is first compressed (using off-peak electricity) in several intercooled stages, meanwhile transferring heat to thermal energy stores (in this case, employing a thermal oil). The compressed air is further cooled via a cold store which has been pre-charged during the discharge phase of the previous cycle. This is the ‘cold recycling’ process, which is essential for achieving acceptable round-trip efficiencies [64]. In the example shown it is implemented via tanks of liquid methanol and propane, similarly to the scheme by Guizzi et al. [65], but other storage media are also possible. The final process during charge is expansion of the cold compressed air back to ambient pressure through a throttle or a cryo-expander. The resulting two-phase mixture is separated with the 'flash gas' being recirculated (dashed line in the figure) whilst the liquid air is transferred to cryogenic tanks. During discharge the liquid air is pumped back up to high pressure, heated by the cold store (thereby recharging it) and then further heated in the hot store. Finally it is expanded through turbines (with intermediate reheat) to generate electricity.

The concept of LAES was first proposed by Smith in 1977 [66] but later developed by both academic and industrial groups, the latter including Mitsubishi [67], Hitachi [68] and Highview [64]. Early this century, an integrated LAES and gas turbine (GT) system was proposed to reduce the GT compression work by compressing liquid rather than ambient air. The liquid air in this case was obtained via the Linde process (exploiting off-peak electricity), and the power output of the GT was more than doubled relative to that of a conventional cycle [67, 68].

A key milestone for LAES was the completion and testing of a 350 kW / 2.5 MWh demonstration plant by Highview, based on the Claude liquefaction cycle (charge) and the Rankine cycle (discharge), as described by Morgan et al. [64]. During discharge, some of the exergetic content of the liquid air is stored by cooling a quartz-based packed bed for later use during the next charge. The measured round-trip efficiency was only 8% but it is expected that larger-scale plants and process improvements will enable efficiencies above 50% to be attained [64, 69]. A more recent milestone was the launch in June 2018 of the first grid-scale plant (a 5 MW / 15 MWh system located near Manchester, also developed by Highview Power [70]), which will help to better assess the performance of large LAES systems.

Ongoing research activity in LAES includes analyses of systems exploiting liquid stores [65, 71], pinch point analysis, parametric studies, economic studies [72, 73] and integration with both nuclear and renewable generation [74, 75]. Additionally, a number of hybrid cycles involving LAES have been proposed. A hybrid CAES / LAES cycle which combines the low cost of LAES with the relatively high efficiency of CAES was introduced by Kantharaj et al. [63, 76], aiming at maximising profits in energy markets where storage is required at different time-scales. Furthermore, two different hybrid PTES / LAES cycles (one described in a patent by Isentropic Ltd [77], and the other one presented in [43] by Farres-Antunez et al.) have been proposed, aiming at improving energy density by making the PTES system provide most of the cooling load required by the LAES plant, therefore removing the need for cold storage tanks.

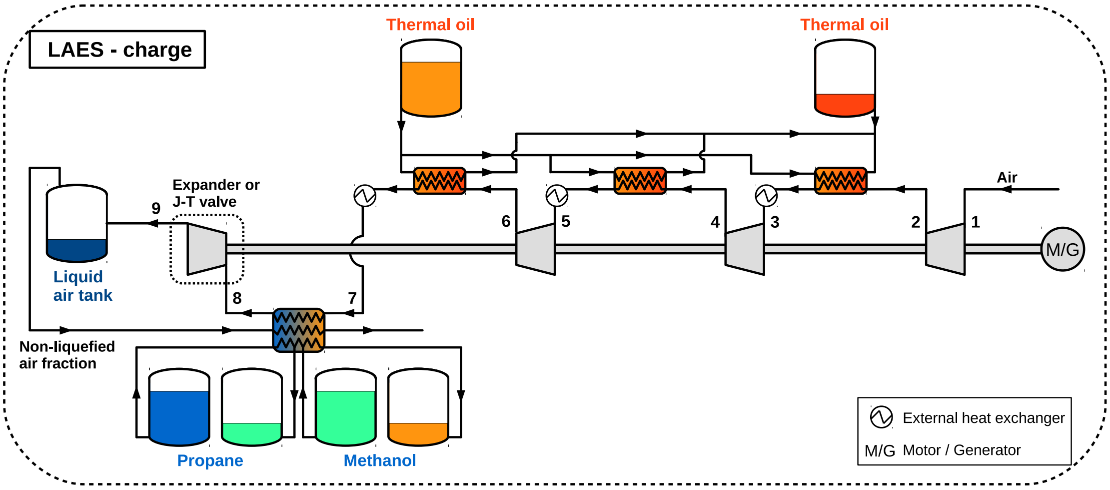

(a) Plant layout during charge.

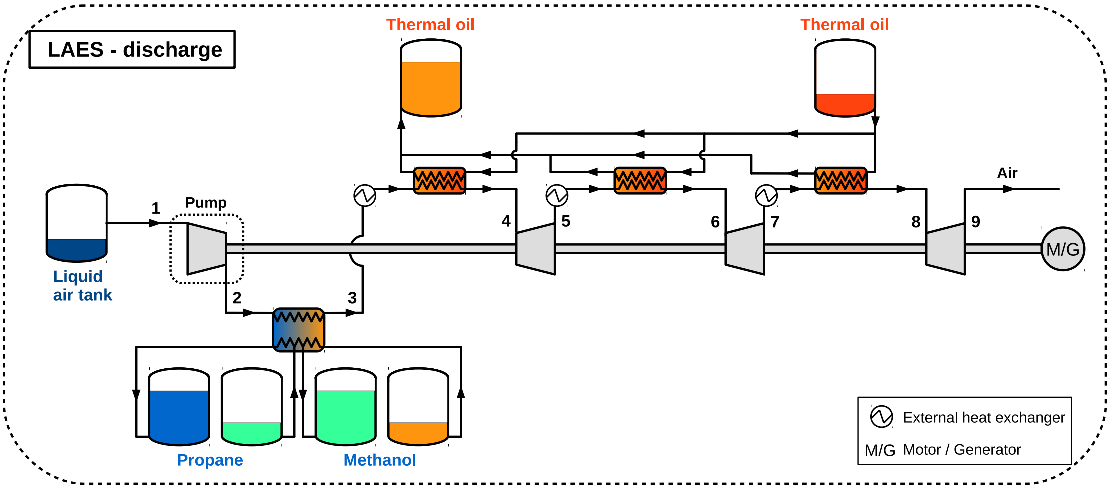

(b) Plant layout during discharge.

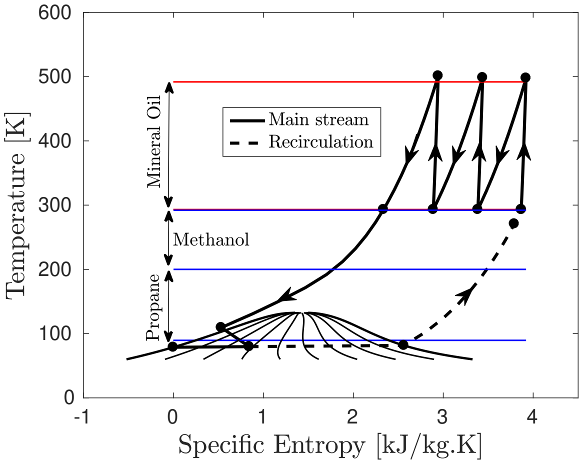

(c) T-s diagram (shown during charge).

Figure 1.9: Plant layouts and T-s diagram of an illustrative LAES cycle, based on an adaptation of the Linde cycle using cold recycling between discharge and charge, similarly to the scheme presented by Guizzi et al. [65].

1.5 Liquid materials for thermal energy storage

As mentioned above, the focus of this thesis is on PTES and LAES cycles that store thermal exergy in the form of sensible heat. Sensible heat storage can be achieved with either solid or liquid media. Solid stores will normally be in the form of packed beds with direct heat transfer between the working fluid and the solid particles. For systems operating at high pressures, however, the packed-bed containment vessel becomes very expensive. Alternatives include the use of a heat exchanger embedded within a solid block [28] or a packed bed with indirect heat transfer, employing a secondary heat exchange fluid [78]. For the first of these, the heat exchanger size is linked to the energy (rather than power) capacity, such that it is likely to be prohibitively expensive for systems with long discharge duration. The second approach may well prove cost effective, but would introduce additional heat exchange and pressure losses. Liquid thermal storage can be realised with a simple two-tank scheme (or even a single tank with a movable piston-like partition), providing efficient and simple operation compared with the management of thermal fronts within packed beds. Liquid tanks are the current standard in most concentrated solar power (CSP) plants [79] and this approach has been adopted here. The best option for thermal storage does, however, require a full cost analysis, which has yet to be undertaken for the systems currently being considered.

Table 1.1 presents a list of candidate liquids for thermal storage applications in the form of sensible heat, collected from a range of sources. Thermophysical properties are presented alongside with estimates of specific cost. The values of specific exergy have been computed using:

$$\Delta e = h_2 - h_1 - T_0(s_2 - s_1) \simeq c_p \left[T_2 - T_1 - T_0 \ln\left(T_2/T_1\right)\right]$$

where the subscripts 1 and 2 refer to discharged and charged conditions respectively and the right hand approximation is based on averaged isobaric heat capacities (used only whenever h and s tables for a given fluid were not available). T_0 is taken as 15 °C, whilst T_1 and T_2 are set to the values of T_{min} and T_{max} specified in the table. Note that the following constraints were applied: (i) for cold storage materials, $T_{\mathrm{max}} \leq T_0$, and (ii) for hot storage materials, $T_{\mathrm{min}} \geq T_0$ and $T_{\mathrm{max}} \leq 600\,^{\circ}\mathrm{C}$ (this upper limit corresponds to an approximate mechanical limit applicable to the most common alloys employed to build tanks, heat exchangers and pipes, as discussed in [44]). Cost data was gathered from various sources:

- The costs of oxygen and nitrogen were obtained from a British manufacturer. Their values are found to be consistent with the cost of the electricity required for air liquefaction: 0.20 kWh/kg (minimum liquefaction work) and 0.20 USD/kWh (estimated electricity price) at 50 % efficiency leads to 0.08 USD/kg.

	Storage material	$T_{\min}$ °C (K)	$T_{\max}$ °C (K)	c_p kJ/kg K	ρ t/m^3	k W/m K	μ mPa s	$\frac{c_{p,\max}}{c_{p,\min}}$	Ref.	Exergy Wh/kg (kWh/m^3)	Cost USD/kg	Cost/exergy USD/kWh
Cold storage	Oxygen	-219 (54)	-183 (90)	1.68	1.23	0.18	0.34	1.02	[80]	51 (63)	0.20	3.9
	Nitrogen	-210 (63)	-196 (77)	2.01	0.84	0.16	0.22	1.02	[80]	25 (21)	0.13	5.2
	N-propane	-188 (86)	-42 (231)	2.02	0.66	0.17	0.55	1.17	[80]	78 (51)	0.50	6.4
	Isopentane	-160 (113)	15 (288)†	1.85	0.71	0.14	0.56	1.29	[80]	47 (33)	1.20	25.5
	N-pentane	-130 (143)	15 (288)†	2.04	0.7	0.14	0.40	1.15	[80]	31 (22)	1.40	45.2
	Ethanol	-114 (159)	15 (288)†	2.01	0.85	0.18	6.59	1.31	[80]	23 (20)	0.50	21.7
	Methanol	-98 (176)	15 (288)†	2.26	0.85	-	1.83	1.13	[80]	19 (16)	0.30	15.8
Hot storage	Water	15 (288)†	100 (373)	4.18	0.98	0.65	0.49	1.01	[80]	12 (12)	0.002	0.2
	Ethylene glycol	15 (288)†	197 (470)	2.81	1.05	0.22	1.80	1.39	[81]	32 (34)	0.80	25.0
	Sunflower oil	15 (288)†	250 (288)	2.52	0.85	0.16	4.16	1.34	[82, 83]	44 (38)	0.30	6.8
	Mineral oil	15 (288)†	300 (573)	2.35	0.78	0.13	1.70	1.56	[84]	57 (44)	1.60	28.2
	Hitec XL	120 (393)	500 (773)	1.45	-	0.20	3.16	-	[85]	75 (-)	0.50	6.7
	Solar salt	230 (503)	600 (873)	1.55	1.82	0.55	1.80	1.00	[86]	91 (166)	0.50	5.5
	Sodium	98 (371)	600 (873)†	1.25	-	46.00	0.21	-	[85]	89 (-)	2.00	22.5
	Eutectic Na-K	15 (288)†	600 (873)†	0.87	0.75	26.20	0.18	-	[85, 87]	64 (72)	2.00	31.1

Table 1.1: Selection of liquid materials for sensible thermal energy storage. The values of the thermophysical properties correspond to intermediate temperatures between $T_{\min}$ and $T_{\max}$. References indicate the sources of the thermophysical data only. Cost values were obtained from different sources, as specified in the text of this section. Exergy and cost per unit exergy have been computed here. Cost values to be taken with caution. †The following constraints were applied: (i) for cold storage materials, $T_{\max} \leq 15\,°\mathrm{C}$, and (ii) for hot storage materials $T_{\min} \geq 15\,°\mathrm{C}$ and $T_{\max} \leq 600\,°\mathrm{C}$.

- The market price of propane was obtained from the online platform Trading Economics for July 2018 [88]. However, it is important to note that the price of propane (like most fossil fuels) is extremely volatile. According to the same source, it has reached a maximum of 0.75 USD/kg and a minimum of 0.15 USD/kg within the last 10 years.
- The cost of water is as reported by a domestic water British provider [89].
- The cost of 'solar salt' has been derived from the CSP inventory costs presented by Herrmann et al. [90]. The value is consistent with the cost reported by Vignarooban et al. [85] and the cost of the constituent components of the salt (which is 60 wt.% $NaNO_3$ and 40 wt.% KNO_3). Hitec XL, which is the commercial name of a ternary mixture made of 7 wt.% $NaNO_3$, 45 wt.% KNO_3 and 48 wt.% $Ca(NO_3)_2$ has been assumed to be manufacturable at a similar price, considering the market price of the constituent components.
- The cost of sodium and Na-K eutectic (which is 22 wt.% sodium and 78 wt.% potassium) are from Vignarooban et al. [85]. However, while the reported cost of sodium metal seems to agree with the lower end of the market price, the reported similar cost for potassium metal could not be verified, since quotes from Chinese manufacturers indicate a price about 10 times higher.
- The costs of all other storage materials (isopentane, n-pentane, ethanol, methanol, ethylene glycol, sunflower oil and mineral-oil-based heat transfer fluid) were obtained by requesting quotes (for bulk quantities) from international manufacturers, mostly from China but also from South Africa (ethanol and methanol), Thailand (ethanol), Turkey (methanol) and Ukraine (sunflower oil). Although in most cases several quotes were obtained for each material, an exhaustive market analysis was not performed, and therefore the cost values shown in the table should be taken with caution.

While examining Table 1.1, one may note the relatively high thermal exergy density of some common liquid materials. Even water, which presents the lowest value in the table, is able to store about $12\,\mathrm{kWh/m^3}$ (exergy, not heat) when operating between ambient temperature and $100\,^{\circ}\mathrm{C}$. This is a remarkably high value compared to the energy density of any pumped hydro facility (for instance, a height difference of 500 m between the two reservoirs corresponds to about $1.4\,\mathrm{kWh/m^3}$) and provides a very strong argument in favour of thermo-mechanical energy storage.

The table represents a useful source of data that will be used along the following chapters to select the most cost-effective liquid materials for different thermodynamic cycles. Note, however, that higher risks and uncertainties will be linked with those materials that have not been used for similar applications yet. For instance, there is abundant experience using water, ethylene glycol, mineral oil and molten salts as heat transfer fluids and/or for thermal energy storage applications. On the other hand, there seems to be little experience using vegetable oils for sensible heat storage, although the low cost and good thermal properties of refined sunflower oil (and other vegetable oils) are very promising if their resistance to thermal cycling and long-term degradation can be proven to be satisfactory. Experience using liquid metals also seems to be more limited, and one must consider the potential impact of corrosion on the heat exchangers, pipes and tanks. For the cold storage, the list includes liquid oxygen and liquid nitrogen, which are very well known, together with hydrocarbons and alcohols that present no major risks as long as they are kept below boiling temperature and standard precautions are taken regarding their flammability.

1.6 Heat exchangers

1.6.1 Major heat exchanger types

The field of heat exchanger design is vast and complex. Heat exchangers (HEXs) have been developed for several different industries and a wide range of applications. Different HEXs can employ different kinds of fluids, under very different operating conditions and be designed to achieve different thermo-hydraulic performances. The book by Shah and Sekulić, *Fundamentals of Heat Exchanger Design* [91], provides an in-depth presentation of the major types of heat exchangers. The following brief descriptions (organised from less to more compact designs) were synthesised and adapted from Shah and Sekulić's work, except when indicated otherwise.

Double-Pipe This is probably the simplest type of heat exchanger. As shown in Fig. 1.10a, it consists of two concentric pipes, within which the two fluids flow in either parallel or counterflow directions. It is particularly suited to applications where one or both fluids are at very high pressures and temperatures. It is also suited to applications where there is high fouling or where the flows are slurries as it may be disassembled for cleaning. The biggest limitation of this type of HEX is its low compactness, making it inadequate for large-scale (and high-performance) applications.

Shell-and-Tube This is the most common heat exchanger in the process and petrochemical industries, because of its capacity to handle a wide range of operating conditions and the high maturity of the technology. Similarly to the double-pipe exchanger, it can withstand very high pressures (generally limited to 300 bar at the shell side and

(a) Double-pipe heat exchanger.

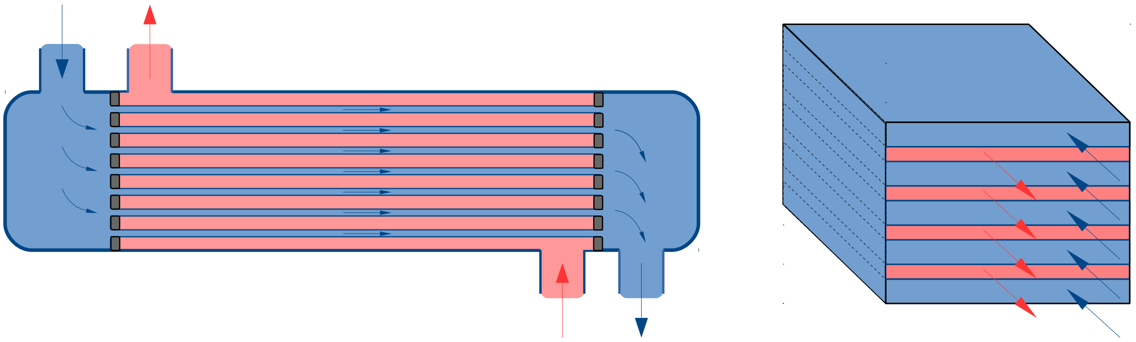

(b) Shell-and-tube heat exchanger.

(c) Generic heat exchanger core based on parallel plates.

Figure 1.10: Layouts of three common heat exchanger types. The tubes in (a) and (b) can be plain or incorporate fins. Similarly, the parallel plates in (c) could be flat or contain channels (or fins) with a vast number of possible geometries. Additionally, the heat exchanger in (c) could belong to different families (plate-and-frame, plate-fin, printed-circuit, or other micro-channel HEXs) depending on the construction features.

1400 bar at the tube side) and very high temperatures, depending on the materials employed. It consists of a bundle of tubes contained within an external shell, as shown in Fig. 1.10b, with the highest-pressure fluid normally flowing inside the tubes. It has a higher surface-to-volume ratio than the double-pipe exchanger but it still is large and heavy compared to other designs. It may operate in parallel-flow, counter-flow, cross-flow and cross-counter-flow configurations. However, a configuration that approaches a pure counter-flow design may be hard to achieve because of the cross-flow regions that occur close to the entrance and exit of the shell-side stream. While smaller hydraulic diameters provide higher heat transfer coefficients and permit more compact exchangers, tubes with larger hydraulic diameters are more robust, and the most common tube sizes have an external diameter of at least 15 mm (corresponding to a surface-to-volume ratio of less than $250\,\mathrm{m}^2/\mathrm{m}^3$ for plain tubes).

Plate-and-frame These consist of a stack of rectangular plates (as in Fig. 1.10c) held together by an external frame. Each plate is stamped with a wavy surface which creates narrow, interrupted and tortuous flow passages, promoting turbulence and significantly increasing the heat transfer rate. This allows a plate-and-frame HEX to be compact, and weigh as little as one-sixth of an equivalent shell-and-tube design. If the plates are sealed with gaskets then the unit can be easily dismounted, facilitating inspection and cleaning. Although the maximum operating temperatures and pressures of gasketed exchangers are relatively low and do not generally exceed 250 °C and 30 bar, more challenging operating conditions can be met by substituting the gaskets for welded or brazed plates.

Plate-fin These are similar to the plate-and-frame HEXs but containing vertical fins between the plates instead of corrugated patterns on the plate surfaces. The fins provide robustness and, more importantly, form a collection of very small passages which can bring the surface-to-volume ratio up to about $1500\,\mathrm{m}^2/\mathrm{m}^3$, depending on the design.

Printed-circuit and micro-channel Originally developed by Heatric Ltd. in the 1980s, the printed-circuit exchanger consists of a stack of diffusion-bonded flat plates on which narrow channels are created by chemical etching. The diffusion-bonding process provides an interface-free joint between the plates, base material strength and high pressure containment capability [92]. It can also withstand high temperatures and be made with materials with good corrosion resistance. The channel depth normally ranges from 0.1 mm to 2 mm, although hydraulic diameters as small as $40\,\mu\mathrm{m}$ have been reported [93], allowing high-effectiveness units to be built at a small fraction of the weight and size of an equivalent shell-and-tube unit. While the channel shape of printed-circuit HEXs tends to be semi-circular, the processes of photo-etching and diffusion bonding have also been used to manufacture long rectangular channels for micro-parallel-plate exchangers [94]. A number of other manufacturing techniques, such as LIGA (German acronym for lithography, moulding and electroplating), stereolithography, and micro-machining can also be employed to construct highly-compact exchangers with channel sizes of 0.1 mm and below [95]. Additionally, additive manufacturing technology is also being proposed to build heat exchangers of complex geometries and very small channel sizes [96].

1.6.2 Flow arrangement

Depending on the geometrical configuration of the heat exchanger channels and on the inlet and outlet positions of each stream, one may encounter three basic kinds of flow arrangements: parallel flow (i.e. both flows in the same direction), counter flow (flows in opposite

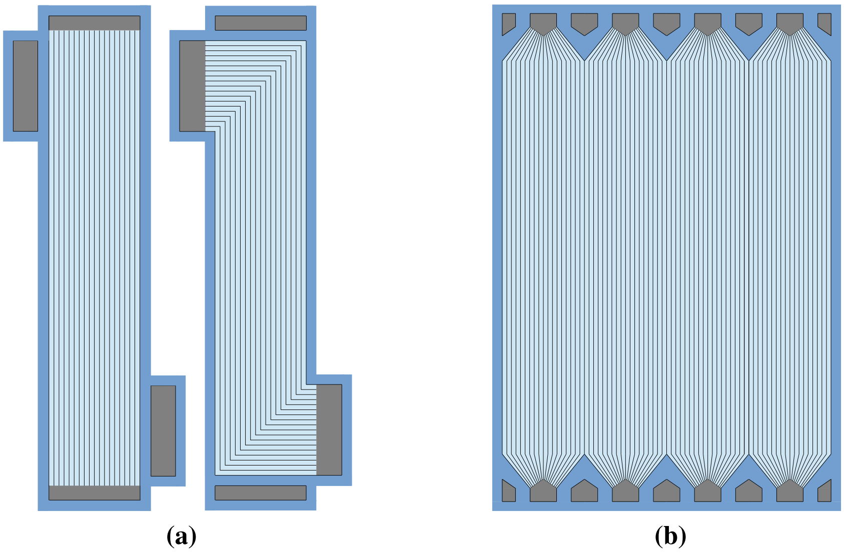

Figure 1.11: Two possible port configurations for parallel plate exchangers. (a) Two adjacent plates of a typical plate-stack for printed circuit heat exchangers, with counter-flow core but cross-flow arrangement at the inlet and outlet regions. (b) One single plate employing the 'platelet' design, in which the cross-flow region at the inlet and outlet ports is minimised.

directions) and cross flow (flows orthogonal to each other). More complex flow arrangements are also possible, but they essentially consist of a combination of the more basic arrangements and present intermediate characteristics. The flow arrangement is important because it has an effect on the performance of the heat exchanger.

As shown in standard heat transfer textbooks (see e.g. Incropera et al. [97]), the counter-flow arrangement is thermodynamically superior because it allows to achieve the highest effectiveness for a given mass flow rate and heat transfer area. On the other hand, a heat exchanger which operates purely in the counter-flow regime is difficult to construct, because a cross-flow region normally occurs when the heat exchanger ports distribute the flow from the source pipe into the channels of the heat exchanger core. For example, Figure 1.11a shows two adjacent plates of a typical printed-circuit HEX. While one stream may have ports aligned with the flow, the ports that collect and distribute the other fluid must be placed orthogonally to the main direction of the flow, creating a cross-flow region. Nevertheless, smart port configurations, such as those employed in the *platelet* design of Fig. 1.11b have been developed which greatly minimise the extent of the cross-flow region and approximate a pure counter-flow arrangement [98].

Apart from the flow configuration, one must consider whether the heat exchanger has *balanced* or *imbalanced* flows. It is said that the flows are balanced when the two streams have the same *heat capacity rate*, i.e. $(\dot{m}c_p)_1 = (\dot{m}c_p)_2$, while the flows are imbalanced if

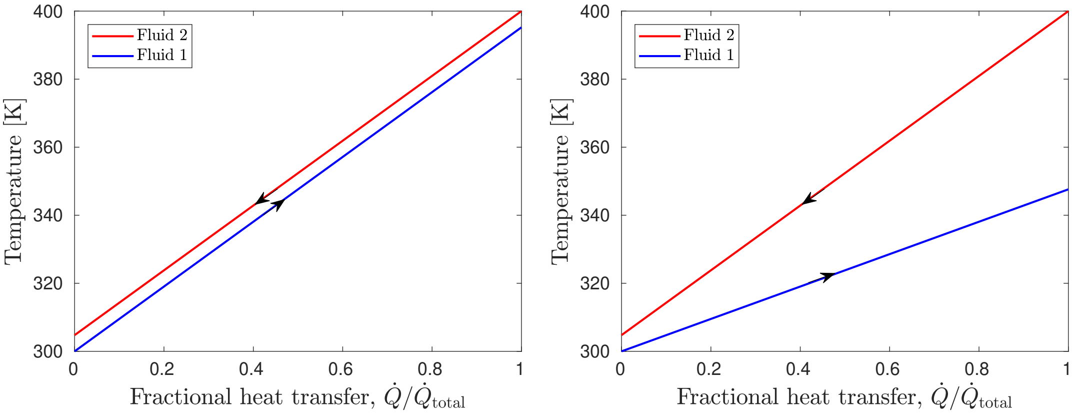

(a) Balanced HEX, $(\dot{m}c_p)_1 = (\dot{m}c_p)_2$ **(b)** Imbalanced HEX, $(\dot{m}c_p)_1 = 2\,(\dot{m}c_p)_2$

Figure 1.12: Temperature distributions in a balanced HEX (a) and an imbalanced HEX (b). The heat exchanger effectiveness is 95 % in both cases. The distribution in (b) minimises irreversible heat transfer and maximises exergy transfer.

the heat capacity rate of one stream is higher than the other. Balanced flows are necessary to minimise temperature differences (see Fig. 1.12) and maximise exergy transfer [99]. On the other hand, in applications where the goal is only to heat up or cool down one of the two fluids, and exergy considerations are not important, imbalanced configurations allow to reach a certain thermal duty with a much lower heat transfer area [97].

In the thermodynamic cycles studied here there are three different types of heat exchangers: gas-gas exchangers acting as regenerators, gas-liquid exchangers that transfer thermal exergy between the working fluid and the storage medium, and ‘external’ heat exchangers that reject heat from the working fluid to the environment. For the first two types of exchanger, minimising irreversibility is extremely important and a high-performance and balanced counter-flow design must be employed. On the other hand, the exchangers for heat rejection only have the purpose to bring the working fluid in thermal equilibrium with the environment, and in that case the most cost-effective solution is to employ an imbalanced configuration with a much higher mass flow rate for the external cooling fluid than for the working fluid, such that a small heat transfer area results in high effectiveness (independently on the flow arrangement).

1.7 Aims and scope of this work

This thesis has two different aims that go hand in hand. The first and foremost is to gain an understanding on the fundamental trends controlling the performance of PTES and LAES, and to analyse, model, develop and optimise new cycle configurations in an attempt to find those that have a higher efficiency or are more cost-effective, thereby instructing future research in the field. The second is to gain an understanding of the fundamental thermodynamic aspects of heat exchanger design, and to develop an optimisation procedure to obtain preliminary designs that maximise exergy transfer and minimise the amount of material needed. This is important because, as will become apparent later on, the performance of heat exchangers can have a large impact on the overall performance of PTES and LAES cycles, and high-performance heat exchangers tend to be large and expensive.

The focus of this thesis is thermodynamics, but, since economics plays such a significant role in the success of storage technologies, some time is spent estimating the costs of energy capacity and power capacity of the different cycles using simplified tools.

Apart from the introduction (the current chapter, number 1), the thesis has four ‘work chapters’ and the conclusions. In chapter 2 a Joule-Brayton PTES cycle using liquid storage media and regeneration is analysed in detail, following a research path that had been proposed in the author’s first year report, *Modelling of Thermal Energy Storage for Bulk Electricity Storage* [38]. In chapter 3, several configurations of a new combined cycle that integrates Joule-Brayton PTES with Linde-based LAES are studied and optimised, with the aim of improving performance and energy density. The chapter is an extended version of the research presented in [43]. Following this, chapter 4 deals with the thermodynamic optimisation of heat exchangers, while in chapter 5 the estimated costs of the most promising cycle configurations are derived. Finally, chapter 6 briefly summarises the main conclusions from this work and suggests a few guidelines for future research.

Chapter 2

Developments of pumped thermal energy storage

2.1 Introduction

As discussed in chapter 1, a number of PTES systems have been proposed so far, based on different thermodynamic cycles. Unlike most of its competitors, the Joule-Brayton implementation has the advantage of relying only on sensible heat storage and employing working fluids that present low variation in specific heat capacity. This allows the thermal energy to be transferred efficiently and the energy and power capacity of the storage system to be independent (which is not normally true for latent heat storage).

While most of the research in Joule-Brayton PTES has focused on schemes using packed beds as thermal reservoirs, this chapter studies an implementation that employs liquid storage media. The layout of the baseline configuration of the cycle is presented in Figure 2.1a, and the corresponding T-s diagram (assuming real compression/expansion machines but ideal heat transfer processes) is shown in Fig. 2.1b. More advanced configurations including regeneration will be presented in section 2.4. Substituting packed beds for liquid storage media has the disadvantage that liquid materials normally tend to have a more limited operating temperature range (and be more expensive) than solid materials. Additionally, heat exchangers are required in order to transfer the thermal energy between the working fluid and the storage media. However, the scheme also presents significant advantages. First, the pressure of the tanks is not bound to the pressure of the working fluid. This allows to use relatively cheap unpressurised tanks[1], while the working fluid (which always remains in the gas phase) can be pressurised, meaning more compact compression and expansion

---

[1] Pressurised tanks are costly because the amount of metal required increases linearly with pressure [32]. This is an important economic consideration for PTES systems employing packed bed reservoirs.

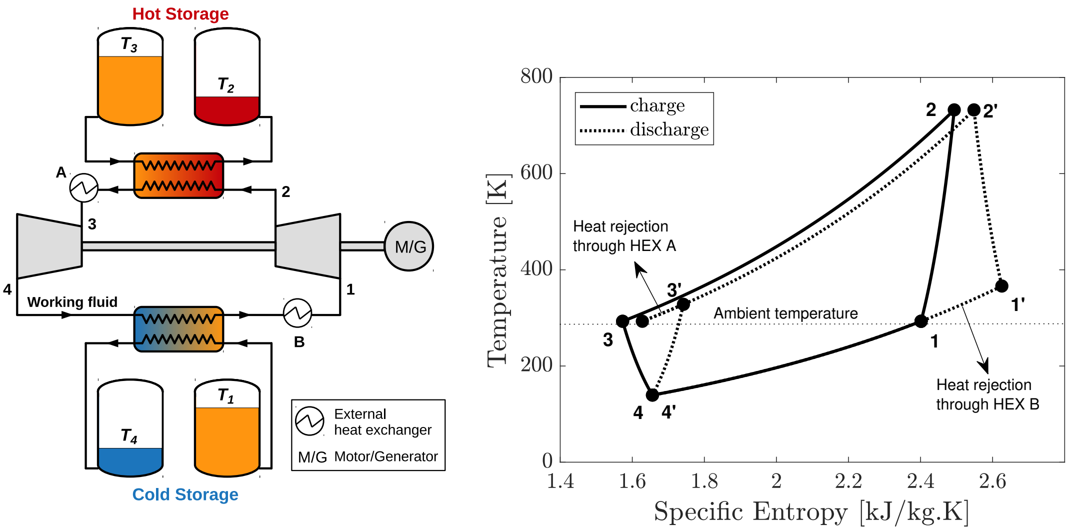

(a) Plant layout (charge).

(b) T-s diagram.

Figure 2.1: Plant layout and T-s diagram of a Joule-Brayton-based PTES cycle employing liquid storage media. In (a), arrows indicate the direction of the working fluid during charge. In (b), cycle direction is 1-2-3-4-1 during charge and (1'-4'-3'-2'-1') during discharge.

machines and also lower pressure losses throughout the cycle. Second, the storage media remain at a single temperature in each tank (as opposed to the thermal front that is created in packed beds), which decreases self-discharge losses and simplifies operation.

Note that the T-s diagram in Fig. 2.1b shows a situation where $T_1 = T_0$ and $T_3 = T_0$, but situations with $T_1 > T_0$ and $T_3 < T_0$ are also possible. The two external heat exchangers (referred to as 'A' and 'B') are used to reject heat to the environment (mostly during discharge), but, depending on the configuration, only one of them may be used.

This chapter presents analytical and numerical studies of the proposed cycle. Ultimately, cycle performance is determined by the complex interaction between loss parameters, operating conditions and variable thermophysical properties. Therefore, numerical methods are required to obtain accurate predictions, but simplified analytical methods are still useful to identify the underlying trends. In section 2.2, the impact that the different components have on the cycle's efficiency is investigated analytically. It will be shown that operating conditions have a significant effect on the different losses and on the energy and power densities, which are examined in section 2.3. Section 2.4 explores the compatibility between the cycle operating conditions and the temperature ranges at which several liquid storage media can be operated, and proposes a number of configurations that satisfy material requirements. Finally, section 2.5 describes a numerical model which was developed to study the performance of the different cycle configurations, and section 2.6 presents the results of the model. The algebraic results presented in section 2.2 were checked against the numerical method described in section 2.5 and yield the same results when employing the same assumptions.

2.2 Impact of component performance on round-trip efficiency

2.2.1 Compressors and expanders

As seen in chapter 1, the Joule-Brayton implementation of the PTES concept has a particularly poor work ratio, which makes the efficiency of the cycle very susceptible to losses in the compression and expansion machines. It is therefore important to understand how to minimise these losses. In this section, the impact of compression and expansion losses will be studied by assuming that the other components (the heat transfer components) are ideal. Because of this assumption, the analysis is relevant to any Joule-Brayton PTES, independently on whether it operates with solid or liquid storage media.

The analysis presented here (i.e. section 2.2.1) follows those by Desrues et al. [29] and White et al. [25] but has been extended to find how efficiency varies with the discharge temperature ratio, find its optimal value, and see how the (maximised) efficiency behaves under certain constraints, such as fixed top temperature but varying charge temperature ratio, or fixed charge temperature ratio but varying bottom temperature.

In order to ensure a valid comparison when studying the effect of different pressure ratios on the overall performance, compressors and expanders are characterised using a *polytropic* (rather than *isentropic*) efficiency [100]. This is defined in the usual fashion as an infinitesimal stage efficiency. Thus, for a compressor ‘c’ and an expander ‘e’ :

$$\begin{aligned} \eta_\mathrm{c} &\equiv \frac{\delta w_\mathrm{c,rev}}{\delta w_\mathrm{c}} = \frac{v\,\mathrm{d}p}{\mathrm{d}h} \\ \eta_\mathrm{e} &\equiv \frac{\delta w_\mathrm{e}}{\delta w_\mathrm{e,rev}} = \frac{\mathrm{d}h}{v\,\mathrm{d}p} \end{aligned} \tag{2.1}$$

Relationships between inlet and outlet conditions are then obtained by integrating the previous equations at constant polytropic efficiency. In the following, the working fluid (a diatomic or monatomic gas such as air or argon) is treated as a perfect gas, i.e. an ideal gas with constant specific heat capacity, in which case $\mathrm{d}h = c_p \mathrm{d}T$. Furthermore, the compression/expansion process is assumed to be adiabatic. This leads to [101]:

$$\begin{aligned}\tau_\mathrm{c} &= \beta_c^{\phi_\mathrm{c}}\\ \tau_\mathrm{e} &= \beta_\mathrm{e}^{\phi_\mathrm{e}}\end{aligned} \tag{2.2}$$

with

$$\begin{aligned}\phi_\mathrm{c} &\equiv \tfrac{\gamma-1}{\eta_\mathrm{c}\gamma}\\ \phi_\mathrm{e} &\equiv \tfrac{\eta_\mathrm{e}(\gamma-1)}{\gamma}\end{aligned} \tag{2.3}$$

where β is the pressure ratio of the compression/expansion, τ is the corresponding temperature ratio, and $\gamma \equiv c_p/c_v$ is the ratio of specific heats. An upper-limit of the round-trip efficiency can be obtained by assuming that there are no storage losses (i.e. the tanks are perfectly insulated), and that all the thermal energy stored during charge can be depleted during discharge (converting part of it into useful work, and rejecting another part to the environment). The round-trip efficiency can then be expressed as the ratio between net specific works during discharge and charge [25]:

$$\chi = \frac{w_\mathrm{net,dis}}{w_\mathrm{net,ch}} = \frac{(T_{2'} - T_{1'}) - (T_{3'} - T_{4'})}{(T_2 - T_1) - (T_3 - T_4)} \tag{2.4}$$

where the temperature points are taken with reference to Figure 2.1b and the primes ($'$) indicate conditions during discharge. Note that, typically, $T_1 \geq T_3$ (for performance reasons that will become obvious later), and either $T_1 \simeq T_0$ or $T_3 \simeq T_0$ (or both), in order to be able to reject heat more efficiently (close to ambient temperature). During charge, τ is defined as the compressor temperature ratio $\tau \equiv \tau_\mathrm{c} = T_2/T_1$, while the expander temperature ratio is $\tau_\mathrm{e} = T_3/T_4$. During discharge, $\tau' \equiv \tau'_\mathrm{e} = T_{2'}/T_{1'}$ and $\tau'_\mathrm{c} = T_{3'}/T_{4'}$. Neglecting pressure losses, the pressure ratios of expander and the compressor have to be the same in each case: $\beta_\mathrm{e} = \beta_\mathrm{c}$ and $\beta'_\mathrm{e} = \beta'_\mathrm{c}$. Thus, according to (2.2):

$$\begin{aligned}\tau_\mathrm{e} &= \tau_\mathrm{c}^{\phi_\mathrm{e}/\phi_\mathrm{c}} = \tau^{\eta^2}\\ \tau'_\mathrm{c} &= {\tau'}_\mathrm{c}^{\phi_\mathrm{c}/\phi_\mathrm{e}} = {\tau'}^{1/\eta^2}\end{aligned} \tag{2.5}$$

where, for simplicity, it has been assumed that compressors and expanders have the same polytropic efficiency, $\eta_\mathrm{e} = \eta_\mathrm{c} \equiv \eta$. Substituting into Eq. (2.4),

$$\chi = \frac{T_{1'}(\tau' - 1) - T_{3'}\left(1 - {\tau'}^{-1/\eta^2}\right)}{T_1(\tau - 1) - T_3\left(1 - \tau^{-\eta^2}\right)} \tag{2.6}$$

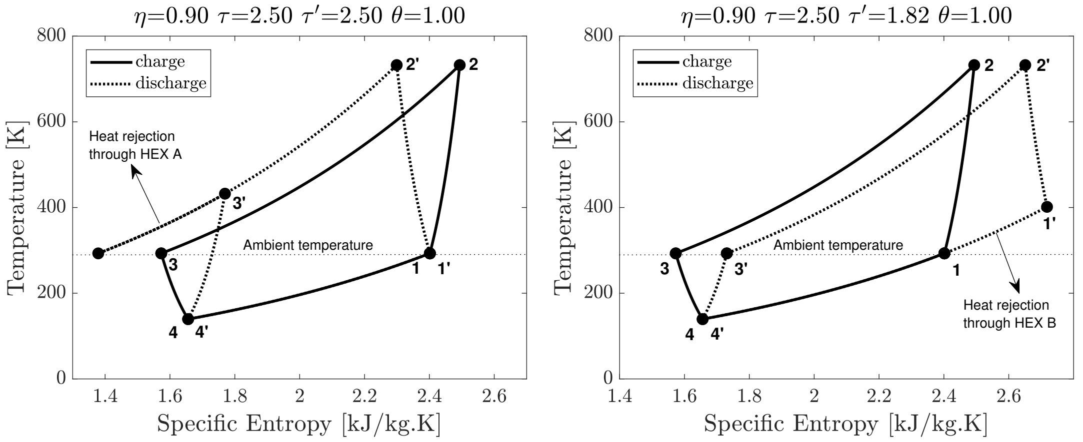

(a) Heat rejection through HEX A. **(b)** Heat rejection through HEX B.

Figure 2.2: (a): T-s diagram for $\tau' = \tau'_{\text{max}}$, with all heat rejection through the external heat exchanger A. (b): T-s diagram for $\tau' = \tau'_{\text{min}}$, with all heat rejection through the external heat exchanger B. The optimal value of τ' lies somewhere in between.

Furthermore, if the heat exchanger processes are ideal, then $T_{2'} = T_2$ and $T_{4'} = T_4$, which means that $T_{1'}/T_1 = \tau/\tau'$ and $T_{3'}/T_1 = \theta\tau'^{1/\eta^2}\tau^{-\eta^2}$, where $\theta \equiv T_3/T_1$. Substituting and rearranging,

$$\chi = 1 - \frac{\tau/\tau' - 1 - \theta\left(1 - \tau'^{1/\eta^2}/\tau^{\eta^2}\right)}{(\tau - 1) - \theta\left(1 - 1/\tau^{\eta^2}\right)} \tag{2.7}$$

Equation (2.7) is a more general version of two similar equations found in the works of Desrues et al. [29] and White et al. [25] (where a certain relationship between τ and τ' has already been specified). The equation shows that χ depends on η and on three *operating* parameters, the charge temperature ratio (τ), the ratio between T_3 and T_1 (θ), and the discharge temperature ratio (τ'). While τ and θ define the shape of the cycle during charge, τ' defines where heat is to be rejected during discharge. Heat may be rejected either through the external heat exchanger A, through the external heat exchanger B, or through both. If all the heat is to be rejected through A (see Fig. 2.2a), then $T_{1'} = T_1$ and

$$\tau' = \tau'_{\text{max}} = \tau \tag{2.8}$$

which, after substitution in Eq. (2.7), leads to the result presented in [29]. On the other hand, if all the heat is to be rejected through B (Fig. 2.2b), then $T_{3'} = T_3$ or, equivalently,

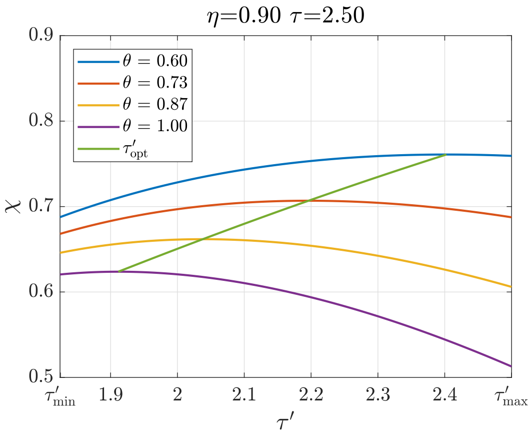

Figure 2.3: Plot of the round-trip efficiency, χ, as a function of the discharge temperature ratio, τ', for fixed values of η and τ and three values of θ.

$\tau'_c = \tau_e$. From Eq. (2.5), this implies

$$\tau' = \tau'_{\mathrm{min}} = \tau^{\eta^4} \tag{2.9}$$

which, after substitution in Eq. (2.7), leads to the result presented in [25]. It can be shown that all practicable stand-alone systems require $\tau'_{\mathrm{min}} \leq \tau' \leq \tau'_{\mathrm{max}}$. The optimal value of τ', however, lies somewhere in between τ'_{min} and τ'_{max}, and can be found by differentiating Eq. (2.7), i.e.

$$\frac{\partial \chi}{\partial \tau'} = 0 \;\Rightarrow\; \tau'_{\mathrm{opt}} = \left(\frac{\eta^2}{\theta}\right)^{\frac{\eta^2}{1+\eta^2}} \tau^{\eta^2} \tag{2.10}$$

Figure 2.3 shows how χ varies with τ' within $\tau'_{\mathrm{min}} \leq \tau' \leq \tau'_{\mathrm{max}}$ and indicates the optimal points. The impact of being far from τ'_{opt} is significant. Also, χ rapidly increases as θ decreases (i.e. as T_1 increases). This can be understood by noticing that, for the ideal cycle, the work ratio is proportional to τ and inversely proportional to θ:

$$\mathrm{W}_{\mathrm{R,rev}} = \left(\frac{w_{\mathrm{c}}}{w_{\mathrm{e}}}\right)_{\mathrm{ch,rev}} = \left(\frac{T_2 - T_1}{T_3 - T_4}\right)_{\mathrm{rev}} = \frac{T_1}{T_4} = \frac{\tau}{\theta} \tag{2.11}$$

From Fig. 2.3, one may also note that τ'_{opt} moves from nearby τ'_{min} to nearby τ'_{max} as θ decreases. This has to do with the fact that there is an exergy loss associated with rejecting heat at temperatures above T_0, and it is more efficient to reject heat through the heat exchanger A (rather than B) when $T_1 > T_3$ (assuming $T_3 \geq T_0$).

From Eq. 2.7, it is found that the efficiency improves when τ increases and when θ decreases. However, both things have the effect of increasing T_2, which is the top temperature of the cycle. In practice, T_2 will be limited by material constraints. For instance, pressurised steel components (such as heat exchangers) are generally limited to temperatures around 600 °C [44], although much higher temperatures may be achieved with ceramic devices. A limit also applies to compressors, which have not yet been developed to operate at the same temperature regimes that turbines normally operate. Nevertheless, it is estimated that, employing Nickel-based alloys, compressors could be developed to operate with outlet temperatures up to 800 °C and above without the need for blade-cooling [102]. Because of these limits, it is interesting to rewrite χ as a function of T_2 and T_3 instead of θ:

$$\chi = 1 - \frac{T_2\left(1/\tau' - 1/\tau\right) - T_3\left(1 - \tau'^{1/\eta^2}/\tau^{\eta^2}\right)}{T_2\left(1 - 1/\tau\right) - T_3\left(1 - 1/\tau^{\eta^2}\right)} \tag{2.12}$$

Using this equation, χ has been plotted in Fig. 2.4a as a function of τ for different values of T_2, while setting $T_3 = T_0$ and using the optimal values of τ' given by Eq. (2.10) (but imposing $\tau' \leq \tau'_{\mathrm{max}}$). Interestingly, when T_2 and T_3 are fixed, χ *decreases* with τ. Again, this may be explained from Eq. (2.11), which can be rewritten to read: $\mathrm{W}_{\mathrm{R,rev}} = T_2/\left(T_3\tau^2\right)$. However, this decrease is limited. When τ is small, T_1 is high (close to T_2) and all the heat must be rejected through the heat exchanger A. However, as τ approaches its maximum value (i.e. when $T_1 \to T_0$), heat can be rejected both through HEX A and HEX B, which lowers the average rejection temperature and reduces the associated exergetic loss, creating a plateau where χ is almost independent of τ.

Another scenario worth considering is that in which T_1 and T_2 (and therefore τ) are fixed but T_3 is allowed to fall to temperatures below T_0. In this case, the work ratio increases as T_3 decreases, but τ' has to be kept equal to τ'_{min} because no heat rejection may occur through HEX A. A plot of χ as a function of T_3 is shown in Fig. 2.4c, from which the benefits of reducing T_3 (particularly for low T_2) are evident, and a T-s diagram of a cycle operating with $T_3 < T_0$ is displayed in Fig. 2.4d for reference. Interestingly, this strategy allows high values of τ to be maintained, which, as will be shown later, has a positive effect on the energy density.

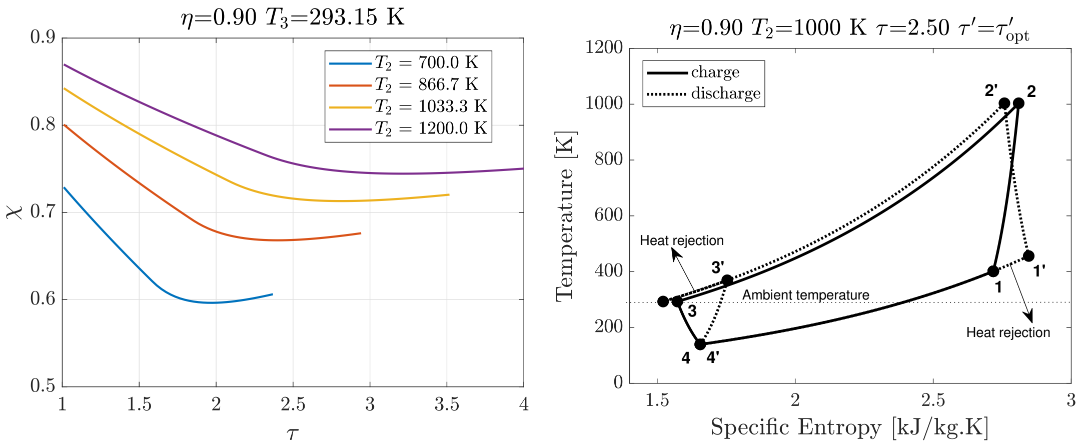

(a) Efficiency as a function of τ.

(b) T-s diagram.

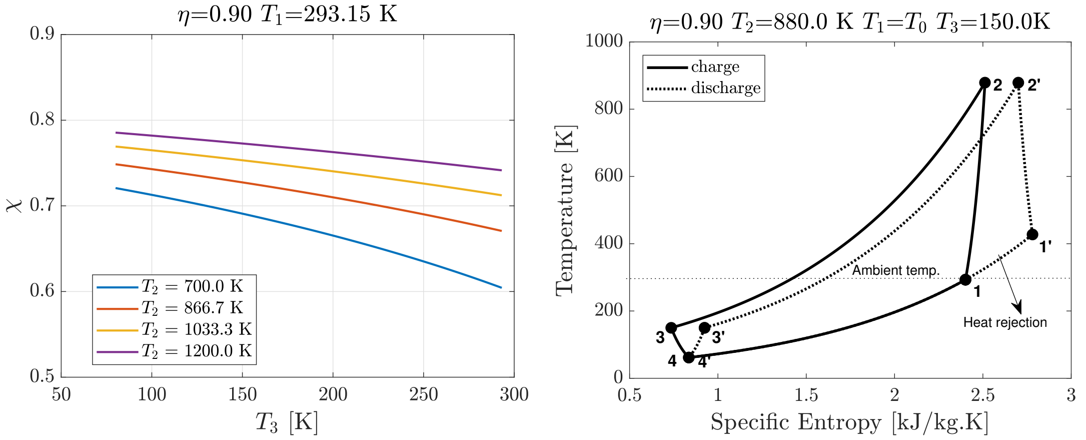

(c) Efficiency as a function of T_3.

(d) T-s diagram.

Figure 2.4: (a) and (b): cycle with $T_1 > T_0$ and $\tau' = \tau'_{\mathrm{opt}}$. (c) and (d): cycle with $T_3 < T_0$ and $\tau' = \tau'_{\mathrm{min}}$.

2.2.2 Heat exchangers

Heat exchangers are traditionally described with an effectiveness that characterises thermal performance and a pressure loss factor that characterises hydraulic performance. In this section, the impact of these parameters on the cycle efficiency are studied separately, assuming ideal compression and expansion machines. An in-depth analysis on the different sources of loss in heat exchangers, and on the minimisation of entropy generation for a given cost, is presented in chapter 4.

2.2.2.1 Thermal performance

The heat exchanger effectiveness is commonly defined as [97, 103]:

$$\varepsilon \equiv \frac{\dot{Q}}{\dot{Q}_{\max}} = \frac{(\dot{m}c_p)_{\mathrm{H}}\left(T_{\mathrm{H,in}} - T_{\mathrm{H,out}}\right)}{(\dot{m}c_p)_{\min}\left(T_{\mathrm{H,in}} - T_{\mathrm{C,in}}\right)} = \frac{(\dot{m}c_p)_{\mathrm{C}}\left(T_{\mathrm{C,out}} - T_{\mathrm{C,in}}\right)}{(\dot{m}c_p)_{\min}\left(T_{\mathrm{H,in}} - T_{\mathrm{C,in}}\right)} \tag{2.13}$$

where the right-hand-side equalities are only valid if c_p is constant for both fluids. In order to minimise irreversible heat transfer, heat exchangers in PTES systems must be of the counter-flow type and are operated with balanced heat capacity ratios, i.e. $(\dot{m}c_p)_{\min} = (\dot{m}c_p)_{\mathrm{H}} = (\dot{m}c_p)_{\mathrm{C}}$, which means that (unless c_p variation is significant) the stream-to-stream temperature difference is the same everywhere along the device. Thus, $\Delta T = T_{\mathrm{H,out}} - T_{\mathrm{C,in}} = T_{\mathrm{H,in}} - T_{\mathrm{C,out}}$, and

$$\Delta T = (1/\varepsilon - 1)\left(T_{\mathrm{H,in}} - T_{\mathrm{H,out}}\right) \tag{2.14}$$

In a PTES cycle, each heat exchanger operates twice. First during charge, when the working fluid transmits thermal energy to the storage media. Second during discharge, when the thermal energy is returned by the storage media to the working fluid. As illustrated in Figure 2.5a, this implies that, at each heat exchanger, a temperature difference equal to $2\Delta T$ occurs between the inlet temperature of the working fluid during charge and its outlet temperature during discharge. As shown in Figure 2.5b, this reduces the value of $T_{2'}$ and increases the value of $T_{4'}$, which limits the discharge temperature ratio and reduces the opportunity to extract mechanical work during discharge. The new values of these temperatures are,

$$T_{2'} = T_2 - 2\Delta T = T_2 - 2\left(1/\varepsilon - 1\right)\left(T_2 - T_3\right) \tag{2.15}$$

and

$$T_{4'} = T_4 + 2\Delta T = T_4 + 2\left(1/\varepsilon - 1\right)\left(T_1 - T_4\right) \tag{2.16}$$

Substituting Eqs. (2.15) and (2.16) into Eq. (2.4), and rearranging, the round-trip effi-

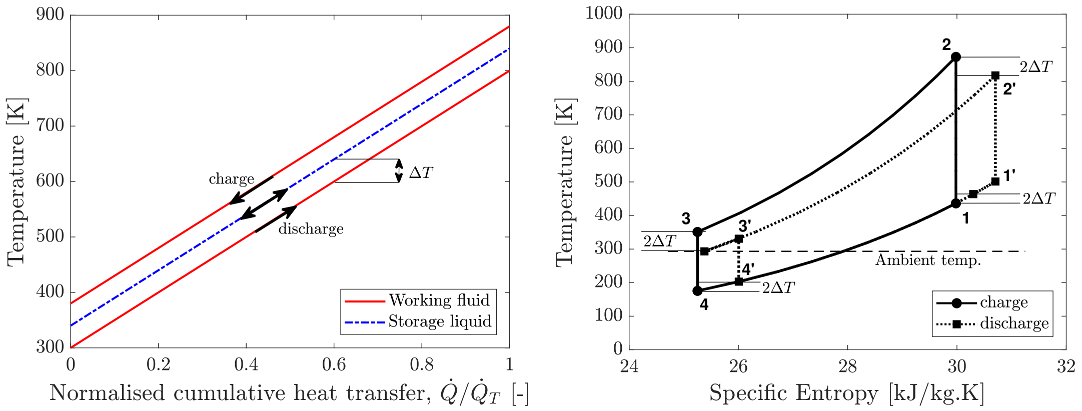

(a) Temperature distribution in HEX.

(b) T-s diagram.

Figure 2.5: Effect of non-ideal heat transfer on (a) Temperature distribution inside the HEX, during charge and discharge, and (b) T-s diagram of the PTES cycle (assuming ideal compression and expansion machines).

ciency becomes,

$$\chi = \frac{\left[(1-\psi)/\tau' - (\theta/\tau+\psi)\right](\tau'-1)}{(1-\theta/\tau)(1-1/\tau)} \tag{2.17}$$

$$\psi \equiv 2(1/\varepsilon - 1)(1-\theta/\tau) \tag{2.18}$$

where $\tau = T_2/T_1 = T_3/T_4$ and $\tau' = T_{2'}/T_{1'} = T_{3'}/T_{4'}$ (because the compression and expansion processes are assumed to be ideal). The optimal discharge temperature ratio is found by differentiation:

$$\frac{\partial\chi}{\partial\tau'} = 0 \Rightarrow \tau'_{\text{opt}} = \tau\left(\frac{1-\psi}{\theta+\psi\tau}\right)^{1/2} \tag{2.19}$$

As in the previous section, maximum and minimum values of τ' can be defined according to the conditions in which all heat is rejected through one of the external heat exchangers. If all heat is rejected through HEX A,

$$\tau' = \tau'_{\text{max}} = \frac{T_{2'}}{T_1 + 2\Delta T} = \frac{\tau(1-\psi)}{(1+\psi)} \tag{2.20}$$

while, if all heat is rejected through HEX B,

$$\tau' = \tau'_{\text{min}} = \frac{T_3 - 2\Delta T}{T_{4'}} = \frac{\tau(\theta-\psi\tau)}{(\theta+\psi\tau)} \tag{2.21}$$

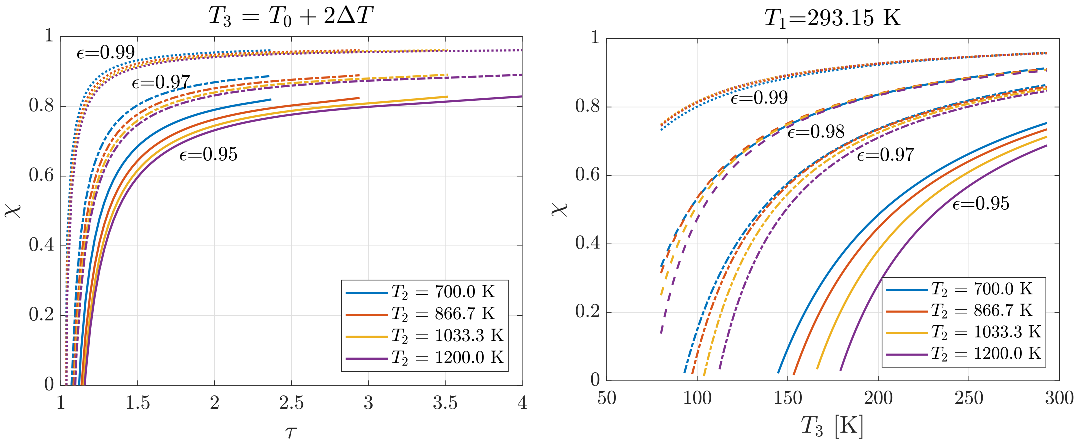

(a) Efficiency as a function τ.

(b) Efficiency as a function of T_3.

Figure 2.6: (a) Efficiency as a function of the charge temperature ratio τ, with $\tau' = \tau'_{\text{opt}}$. (b) Efficiency as a function of T_3, with $\tau' = \tau'_{\text{min}}$. Both graphs present curves corresponding to different values of the top temperature T_2 and effectiveness ε.

The impact of irreversible heat transfer on the round-trip efficiency will depend on the configuration of the cycle. If the configuration is similar to the one in Fig. 2.5b, where T_3 remains close to T_0 and heat may be rejected through both of the external heat exchangers, the cycle can be operated at $\tau' = \tau'_{\text{opt}}$, and the effect of τ on χ is as shown in Fig. 2.6a. Remarkably, the efficiency decreases when τ decreases, which is opposed to the effect of compression/expansion losses that was seen in Fig. 2.4a. This happens because as τ decreases the net work decreases, but the heat transfer rate does not.

If, on the other hand, τ is fixed but T_3 is allowed to fall below T_0, τ' must be operated at τ'_{min} because no heat rejection can occur through HEX A. As shown in Fig. 2.6b, χ decreases as T_3 decreases, which is, again, opposed to the effect of compression/expansion losses. Furthermore, the loss is quite dramatic unless very high values of ε are specified. This is found to be a consequence of the ratio τ'_{min}/τ rapidly decreasing as T_3 decreases, which significantly reduces the opportunity of work recovery during discharge.

It should be expected that this trade-off between compression/expansion losses and heat exchanger losses leads to optimal points, as will be shown numerically in section 2.6.

2.2.2.2 Pressure losses

The pressure loss that the working fluid undergoes between inlet and outlet of a HEX is normally expressed as a fraction of the inlet pressure,

$$f_p \equiv \frac{\Delta p}{p} \tag{2.22}$$

Considering the charge cycle, the following relationships apply regarding the pressure levels at the different points of the cycle: $p_2 = \beta_c p_1$, $p_3 = p_2 (1 - f_p)$, $p_4 = p_3/\beta_e$ and $p_1 = p_4 (1 - f_p)$. Therefore,

$$\beta_e = (1 - f_p)^2 \beta_c \tag{2.23}$$

which means that the expander work is reduced relative to the compressor work, diminishing the amount of work that is recovered. Using (2.2) with $\eta = 1$ (i.e. $\phi_c = \phi_e \equiv \phi$),

$$\tau_e = (1 - f_p)^{2\phi} \tau \tag{2.24}$$

Similarly, for the case of the discharge cycle,

$$\tau'_c = (1 - f_p)^{-2\phi} \tau' \tag{2.25}$$

Employing these expressions in Eq. (2.4) and imposing that $T_{2'} = T_2$ and $T_{4'} = T_4$ (i.e. assuming that pressure losses are the only source of loss) leads to:

$$\chi = \frac{T_2 (1 - 1/\tau') - T_3 \left((1 - f_p)^{-2\phi} \tau' - 1 \right) / \left[(1 - f_p)^{2\phi} \tau \right]}{T_2 (1 - {}^1\!/_\tau) - T_3 \left(1 - 1/ \left[(1 - f_p)^{2\phi} \tau \right] \right)} \tag{2.26}$$

where the optimal, maximum and minimum values of τ' are found as in the previous sections:

$$\frac{\partial \chi}{\partial \tau'} = 0 \Rightarrow \tau'_{\text{opt}} = \frac{(1 - f_p)^{2\phi} \tau}{\theta^{1/2}} \tag{2.27}$$

$$\tau'_{\text{max}} = \tau \tag{2.28}$$

$$\tau'_{\text{min}} = (1 - f_p)^{4\phi} \tau \tag{2.29}$$

The two graphs in Fig. 2.7 show the impact of f_p on the round-trip efficiency. If T_2 and T_3 are fixed (Fig. 2.7a, with $\tau' = \tau'_{\text{opt}}$), χ decreases as τ decreases. This occurs, again, because the net work rapidly decreases when $\tau \to 1$. If, on the other hand, T_2 and T_1 are fixed but T_3 is allowed to fall below ambient temperature (Fig. 2.7b, with $\tau' = \tau'_{\text{min}}$), χ presents a slight increase when T_3 decreases. This occurs because the net work increases as T_3 decreases, and the ratio τ'_{min}/τ is in this case independent of T_3. In both cases, however, the impact of f_p on χ is small compared to the more dramatic impacts of η and ε, especially if f_p can be kept to values below 1 %.

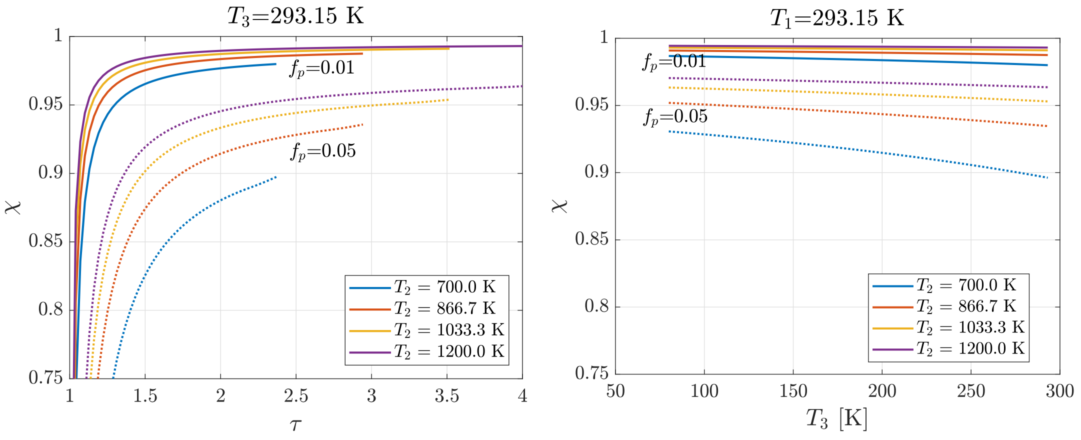

(a) Efficiency as a function τ.

(b) Efficiency as a function of T_3.

Figure 2.7: (a) Efficiency as a function of the charge temperature ratio τ, with $\tau' = \tau'_{\mathrm{opt}}$. (b) Efficiency as a function of T_3, with $\tau' = \tau'_{\mathrm{min}}$. Both graphs present curves corresponding to different values of the top temperature T_2 and pressure loss f_p.

2.3 Energy and power densities

As discussed in chapter 1, the energy density and the power density are two parameters often used to compare different storage technologies. A high energy density is desirable to reduce the footprint and the cost associated with the storage media, while a high power density is associated with more compact (and generally cheaper) conversion devices.

The analysis in this section follows the one in [25], but generalises the expression of energy density to cases where the hot and the cold storage materials are not the same, and shows how to maximise the power density when the top pressure and the top temperature are limited.

In the case of the (ideal) PTES cycle, the energy density is

$$\rho_{\mathrm{E}} = \frac{\dot{W}_{\mathrm{net}}}{\dot{V}_{\mathrm{hm}} + \dot{V}_{\mathrm{cm}}} = \frac{(\dot{m}c_p)_{\mathrm{g}}(T_2 - T_1) - (\dot{m}c_p)_{\mathrm{g}}(T_3 - T_4)}{\left(\dfrac{\dot{m}}{\rho}\right)_{\mathrm{hm}} + \left(\dfrac{\dot{m}}{\rho}\right)_{\mathrm{cm}}} \tag{2.30}$$

where the subscripts ‘hm’, ‘cm’ and ‘g’ refer to the hot storage material, the cold storage material and the gas (working fluid), respectively. Noting that $(\dot{m}c_p)_{\mathrm{g}} = (\dot{m}c_p)_{\mathrm{hm}} = (\dot{m}c_p)_{\mathrm{cm}}$ and rearranging,

$$\rho_{\mathrm{E}} = \frac{(T_2 - T_3)(1 - 1/\tau)}{\left(\dfrac{1}{\rho c_p}\right)_{\mathrm{hm}} + \left(\dfrac{1}{\rho c_p}\right)_{\mathrm{cm}}} \tag{2.31}$$

i.e., the energy density increases with the ρc_p factors of the storage media and is pro-

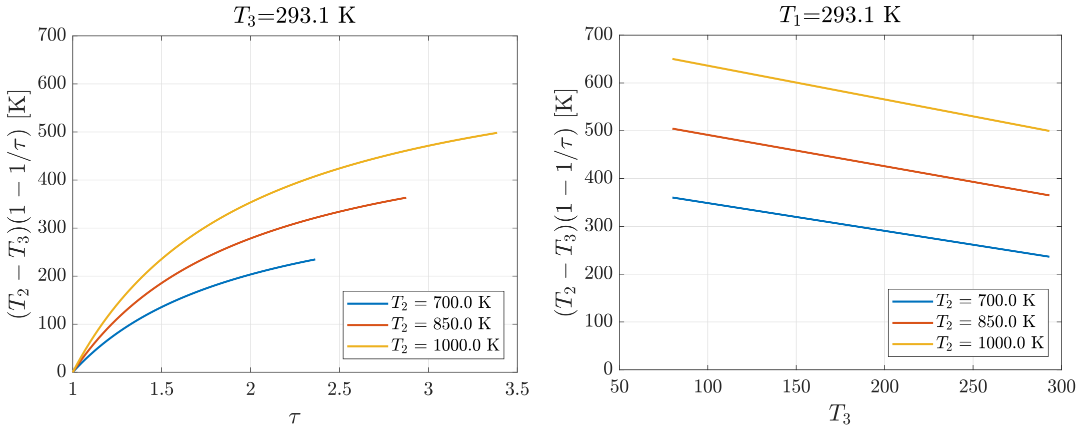

(a) Varying τ.

(b) Varying T_3.

Figure 2.8: Temperature function in Eq. (2.31), which is proportional to the energy density.

portional to the temperature function $(T_2 - T_3)(1 - 1/\tau)$. This function has been plotted in Figs. 2.8a and 2.8b, from where the benefits of having a high τ and a small T_3 (for a given maximum T_2) are evident. The exact value of ρ_E depends on the combination of materials selected for the hot store and the cold store. Nevertheless, a *crude* estimate may be obtained, for instance, by assuming that $\rho c_p \simeq 2\,\mathrm{MJ}/\left(\mathrm{m}^3\mathrm{K}\right)$ (which is a rough approximation for several liquids, including oils and alcohols). If one also assumes that $(T_2 - T_3)(1 - 1/\tau) \simeq 300\,\mathrm{K}$, then Eq. (2.31) leads to $\rho_\mathrm{E} \simeq 80\,\mathrm{kWh}/\mathrm{m}^3$. Actual values, however, will normally be lower than this, as the temperature ranges must be reduced to fit within the limits of the liquid materials or additional materials have to be used in series (see the following section, 2.4, for a discussion on this). Furthermore, Eq. (2.31) corresponds to the ideal cycle, but in practice ρ_E is reduced by the efficiency of the cycle (because the recoverable energy during discharge is the one that really matters).

The power density is, again for the ideal cycle,

$$\rho_\mathrm{P} = \frac{\dot{W}_\mathrm{net}}{\dot{V}_\mathrm{max}} = \rho_1 c_{p,\mathrm{g}} (T_2 - T_3)(1 - 1/\tau) \tag{2.32}$$

where ρ_1 indicates the density at point 1, the point with lowest density in the cycle. The previous equation was shown by White et al. in [25] expressed in terms of the pressure at point 1. Nevertheless, since the system is likely to be limited by material requirements at point 2 (where the maximum temperature and pressure occur), it is interesting to rewrite the expression in terms of p_2 and T_2. Using the ideal gas law and Eq. (2.3),

$$\rho_\mathrm{P} = \frac{\gamma}{\gamma - 1} p_2 (1 - T_3/T_2)(1 - 1/\tau)/\tau^{\frac{1}{\gamma-1}} \tag{2.33}$$

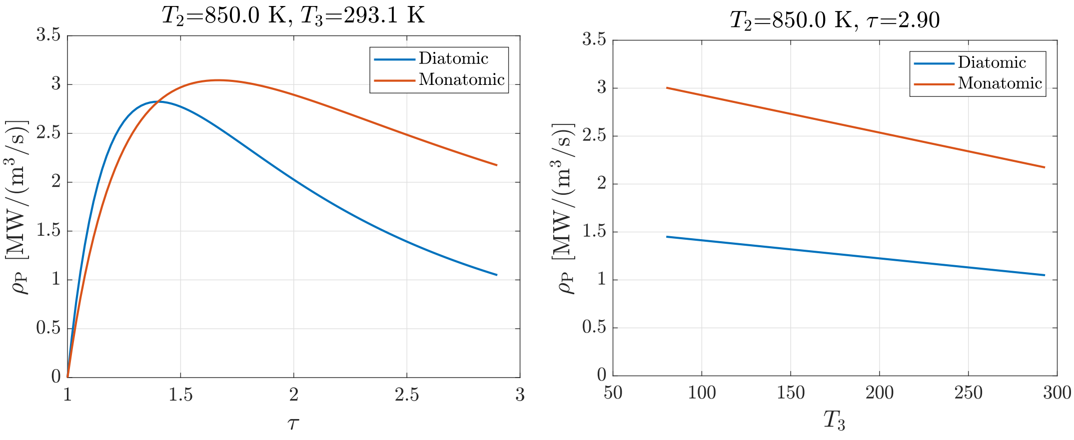

(a) Varying τ. **(b)** Varying T_3.

Figure 2.9: Power density according to Eq. (2.33), assuming $p_2 = 100\,\text{bar}$.

It is now possible to find the optimal τ for which ρ_P is maximised, which happens to have a remarkably simple expression and depend only on the ratio of heat capacities of the gas,

$$\frac{\partial \rho_P}{\partial \tau} = 0 \Rightarrow \tau_{\text{opt}} = \gamma \tag{2.34}$$

Thus, the maximum power density is

$$\rho_{P,\max} = \frac{p_2 \left(1 - T_3/T_2\right)}{\gamma^{\frac{1}{\gamma-1}}} \tag{2.35}$$

where $\gamma^{\frac{1}{\gamma-1}} \simeq 2.15$ for monatomic gases and $\gamma^{\frac{1}{\gamma-1}} \simeq 2.32$ for diatomic gases. Equation (2.33) was plotted in Fig. 2.9a as a function of τ, assuming a maximum allowable pressure $p_2 = 100\,\text{bar}$. The plot shows only a small difference between the two kinds of gas at the optimal point, but a significant advantage in employing monatomic gases when operating at larger values of τ. This is because, as τ increases, p_1 and ρ_1 decrease much faster for a diatomic gas than they do for a monatomic gas. Apart from varying τ, it is also possible to increase ρ_P by decreasing T_3, as shown in Fig. 2.9b. Nevertheless, independently of the specific operating conditions, assuming a value of around $2.5\,\text{MW}/\left(\text{m}^3/\text{s}\right)$ means that the power density can easily be 10 times larger than values for unpressurised systems employing packed beds, which have an estimated $\rho_P = 240\,\text{kW}/\left(\text{m}^3/\text{s}\right)$ [25]. Even if lower maximum values of p_2 are assumed, this is expected to be a critical factor in reducing the cost per unit power of the turbomachines [44].

Accurate predictions of energy and power densities require knowledge of the liquid media employed and the operating conditions of the system, as will be shown.

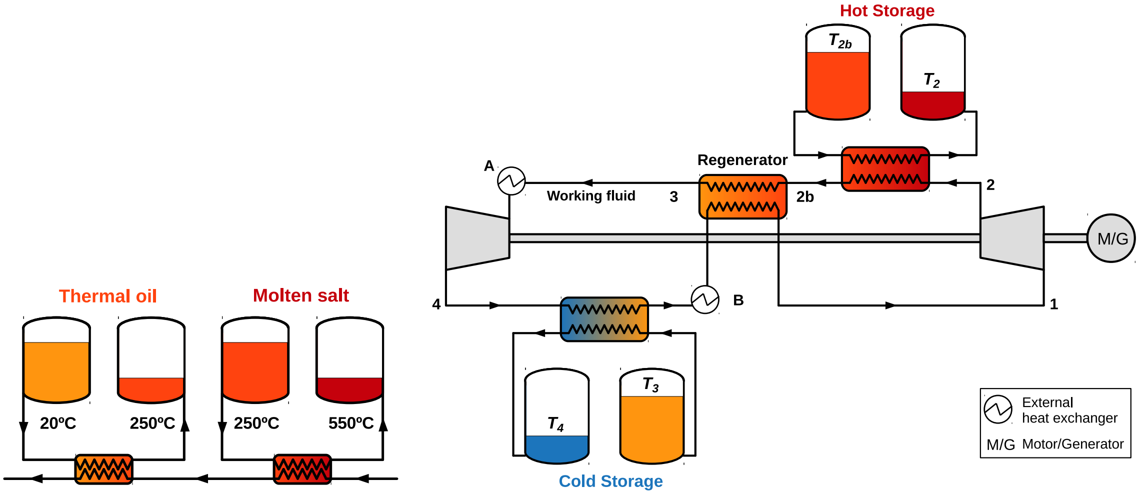

(a) Two storage liquids in series.

(b) Regenerated system.

Figure 2.10: Adaptations of the PTES plant layout to match the temperature ranges of liquid storage media.

2.4 Compatibility with liquid storage media

As mentioned in chapter 1, liquid materials tend to have more limited operating temperature ranges than solid storage materials. From Table 1.1, only the eutectic sodium-potassium mixture is able to span the full temperature range required for the hot store (which typically covers from ambient to $> 500\,^\circ$C), but its relatively high cost and low heat capacity imply a high cost per unit of exergy stored. Furthermore, there seems to be little experience on using this material for thermal energy storage applications and no corrosion data available in the literature [85].

The easiest solution to this problem is to use two or more materials in series, as depicted in Fig. 2.10a. For example, a molten salt may be used in combination with thermal oil or ethylene glycol. In the case of using ‘solar salt’, thermal oil would be preferred because the boiling point of ethylene glycol (around $200\,^\circ$C) is below the freezing point of solar salt (around $220\,^\circ$C). Alternatively, ethylene glycol could be stored in a pressurised tank (at around 3 bar) at higher temperature or a molten salt formulation with a lower freezing point could be employed. Nevertheless, pressurised tanks imply a higher cost, and molten salt formulations with lower freezing points also tend to have lower maximum temperatures before decomposition initiates. For the cold store, a number of alcohols and hydrocarbons may be employed. A T-s diagram of a PTES charge cycle employing solar salt and thermal oil in series for the hot store, and isopentane (which matches well the required temperature range) for the cold store, is shown in Fig. 2.11a. This implementation will be referred to as

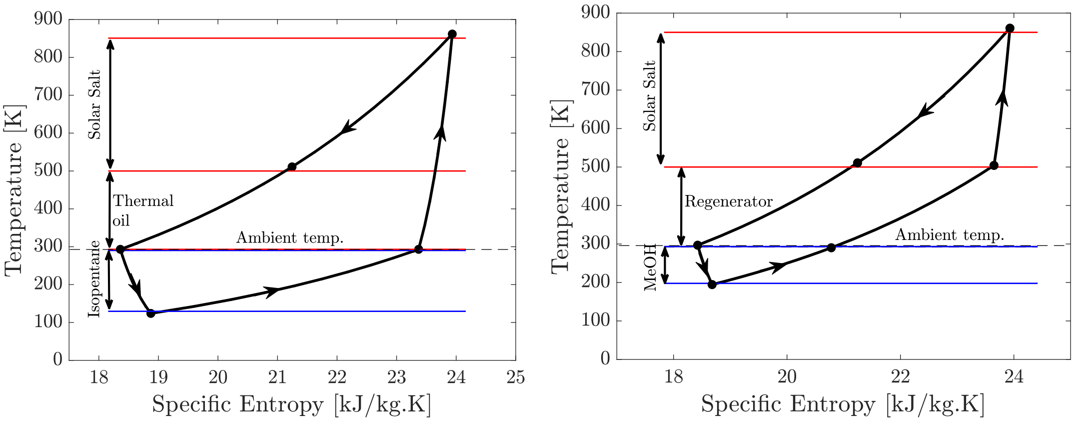

(a) Cycle with two hot store in series, 'no-regen.'.

(b) Cycle with above-ambient regeneration, 'high-regen.'.

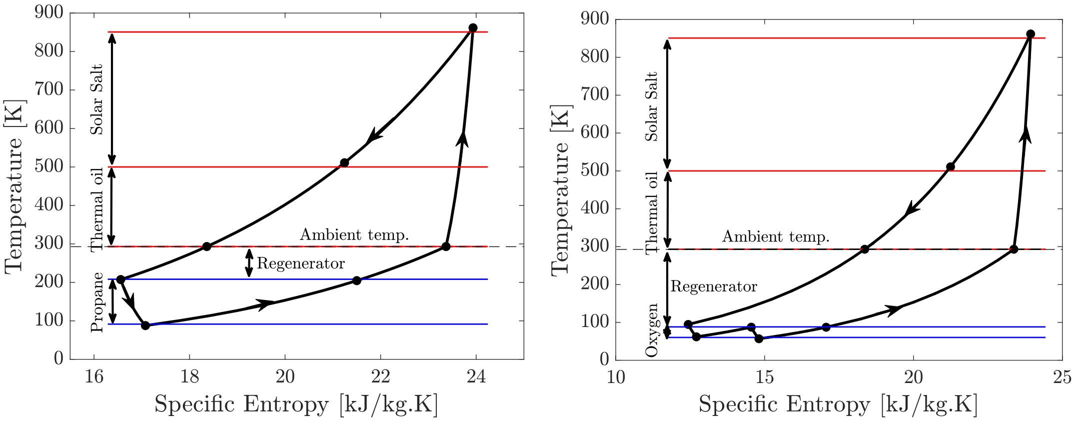

(c) Cycle with sub-ambient regeneration, 'low-regen.'.

(d) Cycle with sub-ambient regeneration and two expansion processes 'low-regen.(2)'.

Figure 2.11: T-s diagrams of several adaptations of the PTES cycle designed to match the temperature ranges of suitable liquid storage media. The diagrams are shown during charge.

the 'no-regen.' implementation, for reasons that will immediately become obvious.

A second solution consists of employing a regenerated cycle, as shown in the layout of Fig. 2.10b. The regenerator creates a temperature gap between the hot stores and the cold store, which permits a more flexible selection of the temperature ranges and improves the work ratio. Regeneration may take place either above or below ambient temperature (but regeneration both above and below ambient is not recommended because it prevents heat rejection at temperatures close to ambient). A cycle with above-ambient regeneration will be referred to as 'high-regen.', while a cycle with below-ambient regeneration will be referred to as 'low-regen.'. However, note that 'high' or 'low' indicates whether regeneration happens at a high or low temperature and not 'how much' regeneration takes place.

A T-s diagram of a 'high-regen.' cycle is shown in Fig. 2.11b. Assuming that T_2 is fixed at around 850 K (an approximate limit for the most common molten salt formulations and stainless steels) and that T_3 is fixed at ambient temperature, regeneration has the effect of reducing τ, which, as discussed before, reduces the impact of compression/expansion irreversibility. Noticeably, such a system may be adapted to employ only solar salt at the hot store, avoiding the use of thermal oil (which is relatively expensive). At the cold side, T_4 is higher than in the non-regenerated case, which allows methanol (which is relatively cheap and widely used by the chemical industry) to be employed instead of isopentane.

Figure 2.11c shows the T-s diagram of a 'low-regen.' cycle. In this case, T_1 is fixed at ambient temperature, and regeneration has the effect of lowering T_3, which also increases the work ratio. It is, however, relatively hard to find fluids that stay in the liquid form along the required temperature range as T_3 decreases. Figure 2.12 shows how the bottom temperature, T_4, varies with T_3. If T_3 falls between $200 \sim 240$ K, then propane (which has a low melting point at around 85 K) can be used as cold storage fluid in unpressurised tanks. At significantly lower temperatures, liquid oxygen becomes an attractive candidate. However, O_2 has a relatively narrow liquid temperature range, between 55 K (melting point) and 90 K (boiling point), which is too short to match the range between T_3 and T_4 at any point. This may be solved by pressurising the oxygen tanks up to 10 bar or, alternatively, by dividing the expansion into two sub-expansions with intermediate heating, as shown in Fig. 2.11d. Since the cold store must cover approximately the same temperature range as the charge expander[2], the subdivision of the expansion process allows the temperature range to be reduced enough to be able to employ O_2 as storage fluid in unpressurised form —N_2 could also be considered, but it has an even narrower range. Such a scheme (which will be referred to as a 'low-regen.(2)' cycle) allows very low temperatures to be reached and the work ratio to be further increased, but also makes the cycle particularly sensitive to losses in the regenerator.

Another aspect that must be considered when comparing the different potential configurations is the choice of working fluid, which must always remain in the gas phase. Typical candidates are air (or nitrogen) and monatomic gases such as argon, helium or neon. Hydrogen, which has outstanding heat transfer properties (as will be shown in chapter 4), could also be considered, but presents the challenges of leakage and high flammability. The 'non-regen.' and 'high-regen.' systems can potentially employ any of the mentioned gases, but air or argon would be preferred over helium or neon because of cost considerations, and air would be preferred over argon because of its superior heat transfer properties and the higher market availability of suitable turbomachinery[3]. In the case of the 'low-regen.' and 'low-

---

[2] The same applies between the hot store and the charge compressor.

[3] Note that this is opposed to PTES systems using packed-bed reservoirs, where argon (or another monatomic gas) is preferable to air because the smaller pressure ratios imply a lower top pressure and therefore a

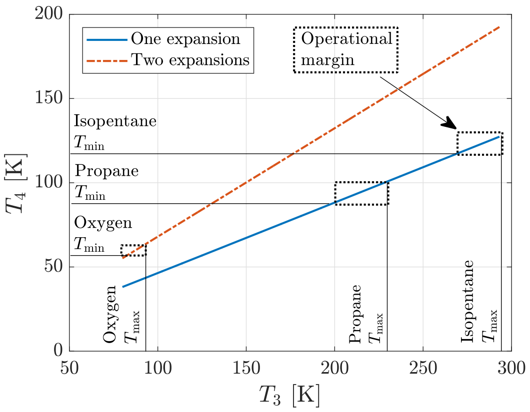

Figure 2.12: Relationship between the temperatures T_3 and T_4, between which the cold storage liquid must operate. Plot corresponds to $\tau = 2.9$ and $\eta = 0.9$.

regen.(2)' implementations, however, the very low bottom temperatures require the usage of either helium or neon as working fluid. Helium tends to be cheaper than neon and has superior heat transfer properties, but its very high c_p makes it unsuitable for turbomachines (see chapter 5 for more details on this). Alternatively, neon may be employed, or helium may be compressed/expanded using positive displacement devices.

Finally, note that the four proposed configurations have a larger number of components than the simpler system that was studied analytically in the previous sections. Since, except for the 'low-regen.(2)' configuration, the number of compressors/expanders is still the same, the impact of compression/expansion losses will remain unchanged. However, the larger number of heat exchangers means that pressure losses will increase, while losses due to irreversible heat transfer will decrease. This is because placing two identical counter-flow heat exchangers in series (instead of one) between given inlets is equivalent to placing a single longer heat exchanger, which has a higher heat transfer area and thus higher pressure losses but operates under smaller temperature differences. Nevertheless, the general trends (i.e. what operating conditions increase or decrease the impact of a certain type of loss) remain unchanged.

2.5 Numerical modelling

In order to predict how the interactions between the several components affect the cycle performance and to be able to account for real fluid properties, it is necessary to employ numerical tools. A numerical model of the PTES cycle (in its various configurations) was developed. As detailed below, the model relies on 'design point' calculations using fixed

---

lower cost of the hot reservoir.

values of component performance parameters, such as compression and expansion efficiencies, fractional pressure losses and heat exchanger effectivenesses.

2.5.1 Implementation

The cycle model was implemented in Matlab R2017. The CoolProp library [80] was employed to evaluate the thermodynamic properties of the working fluids and of the storage materials, with the exceptions of molten salt and thermal oil. The thermodynamic properties of Solar Salt were obtained from a study by Bauer et al. [86], while the properties of thermal oil were interpolated from the values reported by a commercial manufacturer[4] [84].

The code follows the steps below:

- Pre-specified variables, such as the performance of the different components, the mass flow rate of the working fluid, the maximum charge pressure, the charge pressure ratio and the discharged temperatures of the hot and cold storage liquids, are taken as inputs.
- The code makes an initial guess of the state of the working fluid at one point in the cycle, e.g. the compressor inlet (the pressure at that point is given but the temperature may not be accurately known).
- Conditions at the subsequent points are computed component by component. For instance, the compressor outlet state is computed according to the inlet state, the pressure ratio and the polytropic efficiency. The hot HEX takes this state as inlet condition and computes outlet conditions according to the inlet temperature and mass flow rate of the storage liquid, the heat exchanger effectiveness and the pressure drop. The outlet conditions of the storage liquid are ‘stored’ in the charge tank, while the outlet conditions of the working fluid are taken as inlet for the following component.
- Processes in subsequent components are computed similarly, and the work, heat and entropy flows in each component are recorded and used to check the first law and second law balances in the end.
- When the working fluid returns to the initial point of the cycle, conditions are compared with those of the initial guess and, if necessary, the process is repeated until convergence (which typically is reached in a few repetitions, depending on whether the cycle contains a regenerator or not).

---

[4] The data corresponds to a thermal oil made of refined mineral oils which can operate at temperatures up to 320 °C in closed-circuit heat transfer systems, and has thermodynamic properties that fit well within the range of values reported for similar oil-based heat transfer fluids [104].

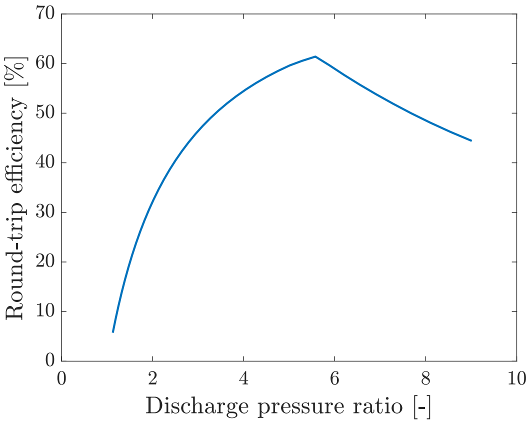

Figure 2.13: Cycle efficiency as a function of the discharge pressure ratio for the 'low-regen.' configuration.

- Steady state operation is assumed throughout and the charge cycle is operated for a pre-specified time, while the discharge cycle is continued until one of the storage tanks is completely discharged —in most configurations, all tanks are depleted simultaneously if the mass flows are balanced correctly.

- The discharge cycle is always operated at the optimal discharge pressure ratio, using the same pressure at the low pressure line as during charge. Since the round-trip efficiency is an unimodal function of the discharge pressure ratio (i.e. it has a single maximum), the optimal point is found via an efficient golden-section search method. Figure 2.13 shows this dependency for the 'low-regen.' configuration. The discharge pressure ratio controls the inlet temperature of the gas at the cold heat exchanger: if it is too low, leftover exergy stays in the tanks, but if it is too high, the mass flow rate of the cold tanks must be increased to ensure that their final temperature is not higher than their initial temperature, which reduces the discharge time and leaves the hot tanks under-discharged. These conflicting phenomena result in the sharp efficiency maximum shown in the plot.

- Once the optimal conditions have been found, the outcomes from the charge and discharge cycles are used to compute relevant parameters, such as round-trip efficiency, energy and power densities and loss distributions.

In interpreting round-trip efficiencies it is important to note that some sources of loss are not taken into account. The main omissions are (i) storage (i.e., heat leakage) losses from the reservoirs; (ii) mechanical and electrical conversion losses; (iii) pumping losses for the liquid storage media.

2.5.2 Compressors and expanders

As previously explained in section 2.2.1, compressors and expanders are modelled by a polytropic efficiency. The total change in enthalpy is found via numerical integration of Eq. (2.1) at constant efficiency. In order to compute the integral, an array of pressure points is created between the pre-specified inlet and outlet pressures. Since the conditions at the inlet point are known, the conditions at each subsequent point are found from (for a compressor):

$$h_{i+1} = h_i + \frac{v_i\left(p_{i+1} - p_i\right)}{\eta_\mathrm{c}} \tag{2.36}$$

$$v_{i+1} = v\left(h_{i+1}, p_{i+1}\right) \tag{2.37}$$

and similarly for an expander. Note that Eq. (2.36) is computed using v_i on the integration step that advances from i to $i+1$, because v_{i+1} is not known a priory. However, once v_{i+1} has been computed, h_{i+1} is re-evaluated using $\overline{v} = 0.5\left(v_{i+1} + v_i\right)$ instead. Since the pressure range is typically of the order of 10:1, computational efficiency is improved (i.e. smaller number of steps required) by using an array of pressure points which is logarithmically spaced rather than linearly spaced.

For baseline calculations, a value of $\eta_\mathrm{e} = \eta_\mathrm{c} = 0.9$ is employed, but the effect of higher and lower values is also considered. A 90% efficiency is realistic for state-of-the-art turbomachinery. Note also that future generations of reciprocating devices might be able to offer higher efficiencies than turbomachinery for gas compression/expansion, but this is as yet unproven. (See for example [30, 101].)

2.5.3 Heat exchangers

Employing the definition of heat exchanger effectiveness (Eq. (2.13)), the enthalpy change of the working fluid on a heating/cooling process is computed as

$$\dot{m}\Delta h = \dot{Q} = \varepsilon\,\dot{Q}_\mathrm{max} \tag{2.38}$$

where $\dot{Q}_\mathrm{max}$ represents the maximum possible heat transfer rate, i.e. that of an infinitely large heat exchanger. In order to find Δh, one must find $\dot{Q}_\mathrm{max}$ first. While, for constant c_p scenarios, the value of $\dot{Q}_\mathrm{max}$ is simply equal to $\left(\dot{m}c_p\right)_\mathrm{min}\left(T_\mathrm{H,in} - T_\mathrm{C,in}\right)$, the value for non-constant c_p scenarios is non-trivial and depends on the location of the pinch point. As depicted in Fig. 2.14, the pinch point may happen:

(a) At the cold inlet.

(b) At the hot inlet.

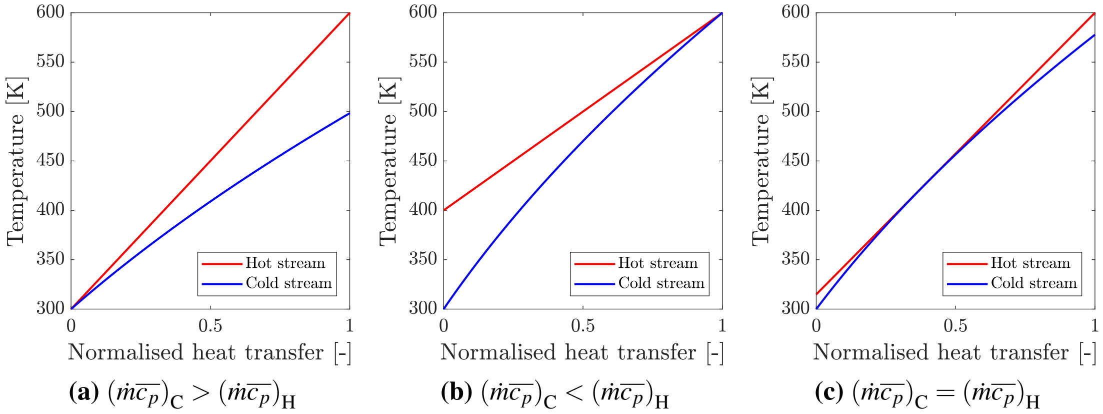

(a) $(\dot{m}\overline{c_p})_{\mathrm{C}} > (\dot{m}\overline{c_p})_{\mathrm{H}}$ **(b)** $(\dot{m}\overline{c_p})_{\mathrm{C}} < (\dot{m}\overline{c_p})_{\mathrm{H}}$ **(c)** $(\dot{m}\overline{c_p})_{\mathrm{C}} = (\dot{m}\overline{c_p})_{\mathrm{H}}$

Figure 2.14: Possible temperature distributions in a HEX with $\varepsilon = 1$.

(c) Somewhere in the middle of the HEX.

In the case of Fig. 2.14c, the two flows have equal *averaged* heat capacity rates (i.e., the flows are 'balanced') and the effectiveness of the HEX is 100 %. If the specific heat capacities of both fluids were constant, the temperature difference everywhere on the exchanger would be zero and the process would be reversible. But because c_p is a function of T, finite temperature differences appear outside the pinch point and heat transfer becomes irreversible.

If the pinch point happens in the middle (as in Fig. 2.14c), then ΔT has a local minimum at that point. Since $\Delta T = T_{\mathrm{H}} - T_{\mathrm{C}}$, this implies,

$$\frac{\mathrm{d}(\Delta T)}{\mathrm{d}\dot{Q}} = 0 \Rightarrow \frac{\mathrm{d}T_{\mathrm{H}}}{\mathrm{d}\dot{Q}} = \frac{\mathrm{d}T_{\mathrm{C}}}{\mathrm{d}\dot{Q}} \tag{2.39}$$

Using the steady-flow energy equation and neglecting changes in kinetic and potential energy within each stream:

$$\mathrm{d}\dot{Q} = \dot{m}\,\mathrm{d}h = \dot{m}\left(\left(\frac{\partial h}{\partial T}\right)_p \mathrm{d}T + \left(\frac{\partial h}{\partial p}\right)_T \mathrm{d}p\right) \simeq \dot{m}c_p\,\mathrm{d}T \tag{2.40}$$

where the last approximation is exact for perfect and semi-perfect gases, and a good approximation for any fluid as long as the pressure loss is small. Equations (2.39) and (2.40) imply that the local heat capacity rates of both streams must be equal at the pinch point:

$$(\dot{m}c_p)_{\mathrm{C}} = (\dot{m}c_p)_{\mathrm{H}} \quad \text{at } T = T_{\mathrm{pinch}} \tag{2.41}$$

which means that T_{pinch} may be found by numerically solving Eq. (2.41) for each pair of

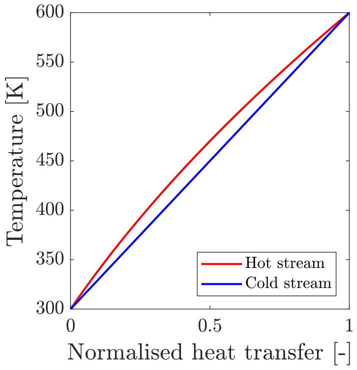

Figure 2.15: Temperature distribution in a HEX with $\varepsilon = 1$, $(\dot{m}\overline{c_p})_{\mathrm{C}} = (\dot{m}\overline{c_p})_{\mathrm{H}}$ and a pinch point occurring at the inlets.

$c_p\,(T)$ functions.

PTES systems normally operate with balanced flows because this minimises exergy destruction. Nevertheless, as shown in Fig. 2.15, balanced flows do not ensure that the pinch point will occur in the middle of the HEX, as it can still occur at one (or both) of the inlets, depending on the shape of the c_p functions. In order to determine where the pinch point occurs in each case and find the value of $\dot{Q}_{\mathrm{max}}$, one must compute the three following integrals:

$$\dot{Q}_{(\mathrm{a})} = \dot{m}_{\mathrm{H}} \int_{T_{\mathrm{C,in}}}^{T_{\mathrm{H,in}}} c_{p\mathrm{H}}\,\mathrm{d}T \tag{2.42}$$

corresponding to $T_{\mathrm{pinch}} = T_{\mathrm{C,in}}$,

$$\dot{Q}_{(\mathrm{b})} = \dot{m}_{\mathrm{C}} \int_{T_{\mathrm{C,in}}}^{T_{\mathrm{H,in}}} c_{p\mathrm{C}}\,\mathrm{d}T \tag{2.43}$$

corresponding to $T_{\mathrm{pinch}} = T_{\mathrm{H,in}}$, and

$$\dot{Q}_{(\mathrm{c})} = \dot{m}_{\mathrm{C}} \int_{T_{\mathrm{C,in}}}^{T_{\mathrm{pinch}}} c_{p\mathrm{C}}\,\mathrm{d}T + \dot{m}_{\mathrm{H}} \int_{T_{\mathrm{pinch}}}^{T_{\mathrm{H,in}}} c_{p\mathrm{H}}\,\mathrm{d}T \tag{2.44}$$

where T_{pinch} is obtained from Equation (2.41). For a given set of inlet conditions and mass flow rates, the maximum possible heat transfer rate must be the minimum of the three previous integrals, i.e.

$$\dot{Q}_{\mathrm{max}} = \min\left(\dot{Q}_{(\mathrm{a})}, \dot{Q}_{(\mathrm{c})}, \dot{Q}_{(\mathrm{c})}\right) \tag{2.45}$$

Note that, if $\dot{Q}_{\text{max}}$ was larger, then the temperature curves of the hot and the cold streams would cross each other. Furthermore, finding $\dot{Q}_{\text{max}}$ from Eq. (2.45) corresponds to computing $(\dot{m}c_p)_{\text{min}}\left(T_{\text{H,in}} - T_{\text{C,in}}\right)$ in constant c_p scenarios.

Once $\dot{Q}_{\text{max}}$ has been found, $\dot{Q}$ (the actual heat transfer rate) is found by applying the selected level of effectiveness according to Eq. (2.38). Then, the changes in enthalpy and outlet conditions for both fluids are determined. Baseline calculations assume 97% effectiveness, but ε is varied to assess its impact. Although this value might seem optimistic, measured effectivenesses as high as $97-98\,\%$ have been reported for compact counterflow heat exchangers (specially in the context of cryogenic applications), and higher efficiencies can be achieved if a careful design that minimises axial conductivity and flow maldistribution is employed [93, 94, 105].

Finally, a 1% pressure loss is assumed for the working fluid side of all heat exchangers except those rejecting heat to the environment, for which pressure losses are neglected on the grounds that they require smaller surface areas[5].

2.5.4 First and second law analyses

Once the thermodynamic states of the working fluid at the inlets and outlets of each component have been determined, the work and heat flows are computed and a first law balance is made for both the charge and discharge cycles. A graphical representation of the different energy flows is shown in Fig. 2.16, while the gas states and the first law balance for the 'high-regen.' cycle are shown in Appendix A.

A second law analysis is also applied to determine the distribution of exergetic losses. The "lost work" due to irreversibility within the i-th component (i.e., heat exchanger, compressor etc.) is given by

$$\dot{W}^{i}_{\text{L, irr}} = T_0\,\dot{S}^{i}_{\text{irr}} \tag{2.46}$$

where $\dot{S}^{i}_{\text{irr}}$ is the entropy generation by irreversibility (per unit time). Table 2.1 summarises how this quantity is computed in each case. Note that, although the external heat exchangers are treated as ideal, they also contribute to the overall entropy generation because they reject heat at temperatures above T_0.

---

[5] The external heat exchangers, whose function is to reject heat to the environment, will typically employ a higher $\dot{m}c_p$ for the external fluid (the coolant) than for the internal working fluid. According to the standard NTU-effectiveness model (see e.g. [97]), a HEX with $\varepsilon = 99\,\%$ will require 95.0 transfer units if the flows are balanced, but less than 7.8 transfer units if the $\dot{m}c_p$ of the coolant is at least twice that of the working fluid. The number of transfer units is proportional to the heat transfer area.

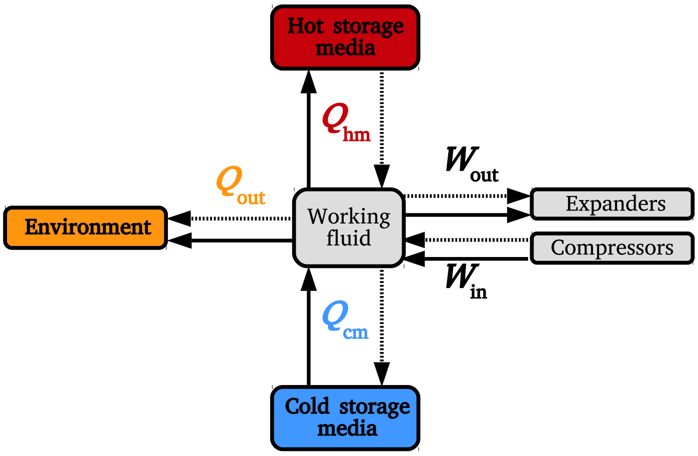

Figure 2.16: Work and heat flows on a PTES system. Solid lines refer to charge. Dashed lines refer to discharge.

The different losses relate to the round-trip efficiency through

$$\chi = 1 - \frac{\sum W^{i}_{\mathrm{L,irr}}}{W_{\mathrm{ch}}} \tag{2.47}$$

where W_{ch} is the net work input during charge. Efficiencies computed in this manner are identical to the values found through a First Law approach, thereby providing a check on the consistency of the cycle model.

Table 2.1: Entropy generation formulas.

Component	$\dot{S}_{\mathrm{irr}}$
Compressor/expander	$\dot{m}\left(s_{\mathrm{out}} - s_{\mathrm{in}}\right)$
Heat exchanger/regenerator	$\dot{m}_{\mathrm{H}}\left(s_{\mathrm{out}} - s_{\mathrm{in}}\right)_{\mathrm{H}} + \dot{m}_{\mathrm{C}}\left(s_{\mathrm{out}} - s_{\mathrm{in}}\right)_{\mathrm{C}}$
Heat exchanger (external)	$\dot{m}\left(s_{\mathrm{out}} - s_{\mathrm{in}} - \left[h_{\mathrm{out}} - h_{\mathrm{in}}\right]/T_0\right)$

2.6 Comparative study of potential configurations

The numerical model described above was employed to study the four cycle configurations shown in Figure 2.11. One important trend that was identified earlier in this chapter is that the operating conditions that reduce the impact of compression/expansion losses tend to increase the impact of heat exchanger losses, suggesting that optimal points are likely to occur. This is confirmed with the numerical model.

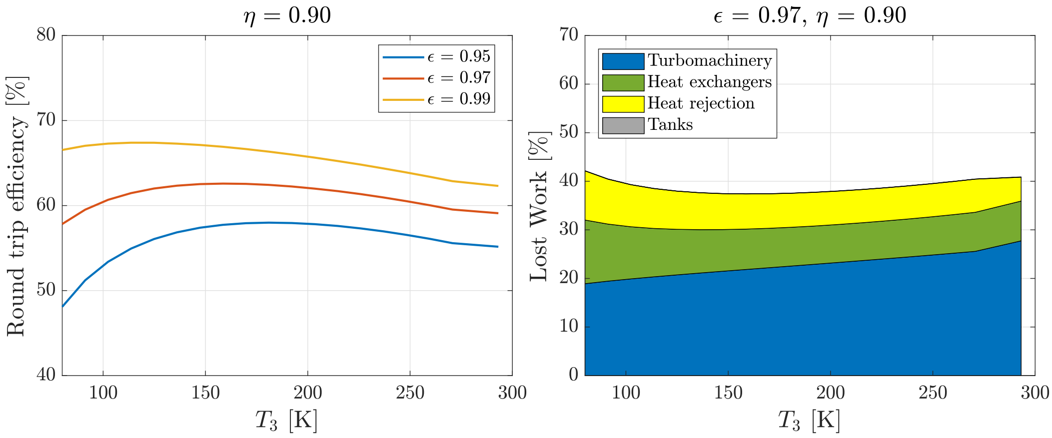

(a) Cycle with sub-ambient regeneration (Fig. 2.11c).

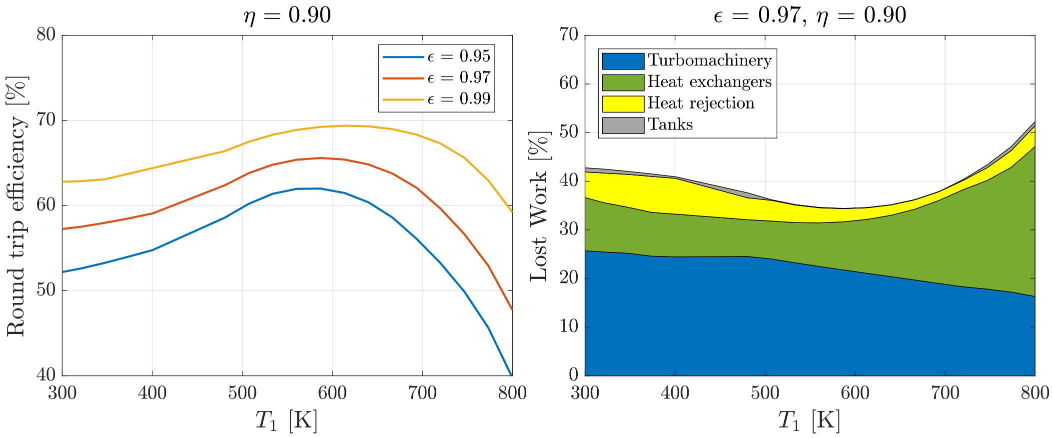

(b) Cycle with above-ambient regeneration (Fig. 2.11b).

Figure 2.17: Round-trip efficiency (left) and loss distribution (right) for two different cycle configurations with $T_2 = 850\,\mathrm{K}$.

Figure 2.17a shows the round-trip efficiency and the loss distribution for the ‘low-regen.’ configuration as a function of the temperature T_3 (while $T_1 = T_0$ and $T_2 = 850\,\mathrm{K}$). As T_3 decreases, turbomachinery losses decrease (because the work ratio increases), but losses in the regenerator increase. Furthermore, as losses in the regenerator increase, the optimal discharge pressure ratio decreases, which increases the heat rejection losses. This results in an optimal T_3 value, which depends on the polytropic efficiency of the turbomachines and the effectiveness of the HEXs. For $\eta = 0.9$ and $\varepsilon = 0.97$, the optimal value is not far below $200\,\mathrm{K}$, which is the minimum possible value if propane is to be used as cold storage medium (see Fig. 2.12). In the case of the ‘low-regen.(2)’ configuration, the optimal T_3 lies above $90\,\mathrm{K}$, which is the maximum possible value for oxygen as storage medium.

Figure 2.17b shows the round-trip efficiency and the loss distribution for the ‘high-regen.’ cycle as a function of the temperature T_1 (while $T_3 = T_0$ and $T_2 = 850\,\mathrm{K}$). Again,

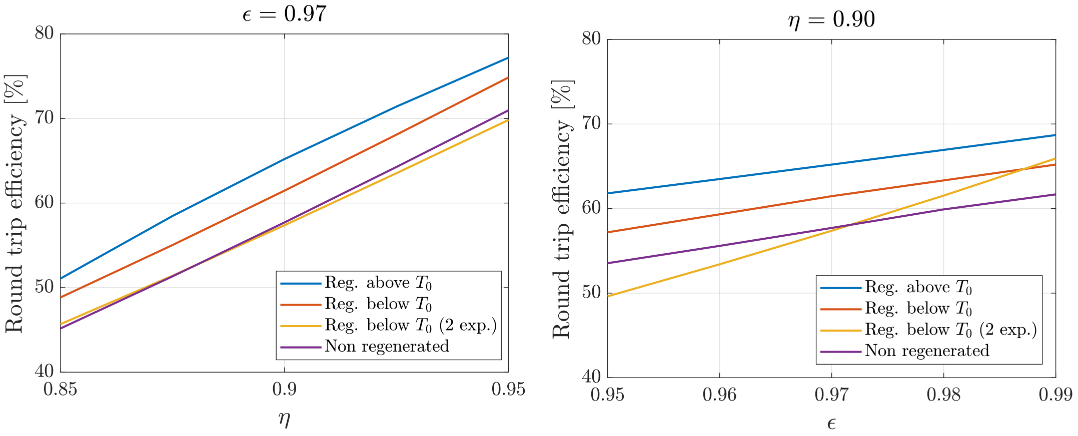

(a) Sensitivity to polytropic efficiency. **(b)** Sensitivity to heat exchanger effectiveness.

Figure 2.18: Sensitivity of the round-trip efficiency to η and ε for the different cycle configurations.

the same conflict between turbomachine and heat exchanger losses occurs. In this case, the optimal T_1 is found close to 600 K. However, reducing T_1 from 600 K to 550 K has a minor negative impact on the round-trip efficiency while it allows the energy density to be increased by more than 15 % (due to a higher utilisation of the molten salt). Thus, $T_1 = 550\,\mathrm{K}$ is selected for subsequent calculations employing this cycle configuration.

Once the operating conditions have been established according to the different storage media, it is possible to compare the different cycles. Figure 2.18a shows the sensitivity of the round-trip efficiency to polytropic efficiency (for fixed ε) for the different cycles, while Fig. 2.18b shows the sensitivity to heat exchanger effectiveness (for fixed η). In general, η has a larger impact than ε, and all cycle configurations are affected similarly by both parameters. This is with the exception of the 'low-regen.(2)' configuration, where the regenerative process extends to very low temperatures and implies a higher sensitivity to ε.

Finally, Table 2.2 presents a summary of relevant parameters for the different configurations at baseline conditions[6]. Round-trip efficiency, energy density and power density are shown along with the required amount of storage materials and the estimated cost of storage capacity. The cost of storage capacity is obtained by adding the cost of the storage materials (see Table 1.1) and the cost of the storage tanks. For molten salts, the cost of the tanks (which have to withstand high temperatures and corrosion) is estimated at 150 \$/m^3 from existing CSP power plants [90]. For the other fluids a cost of 50 \$/m^3 is estimated for large carbon-steel tanks with a design temperature of 340 °C [106]. The cost of insulation is accounted for by adding a factor of 20 % to the cost of the tanks —this factor has also been

---

[6] Top temperatures and pressures of 850 K and 100 bar (during charge). $\eta = 0.9$, $\varepsilon = 0.97$ and $f_p = 0.01$.

Table 2.2: Summary of relevant parameters for the different cycle configurations.

	Configuration			
Parameters	'No-regen.'	'High-regen.'	'Low-regen.'	'Low-regen.(2)'
Working fluid	Nitrogen	Nitrogen	Neon	Helium
Efficiency [%]	**57.7**	**65.2**	**61.3**	**57.6**
ρ_{E} [kWh/m^3]	38.9	46.2	46.4	42.1
$\rho_{\mathrm{P,ch}}$ [MW/$\left(\mathrm{m}^3/\mathrm{s}\right)$]	1.74	3.77	3.44	3.76
$\rho_{\mathrm{P,dis}}$ [MW/$\left(\mathrm{m}^3/\mathrm{s}\right)$]	0.72	2.45	1.36	1.50
Solar salt [t/MWh]	10.0	15.7	8.3	8.0
Mineral oil [t/MWh]	6.8	-	5.7	5.5
Cold store [t/MWh]	7.7 (Isopentane)	10.4 (Methanol)	6.5 (Propane)	15.0 (Oxygen)
Cost materials [$/kWh]	25.1	11.0	16.5	15.8
Cost tanks [$/kWh]	4.3	4.6	3.7	3.9
Total cost [$/kWh]	**29.4**	**15.5**	**20.2**	**19.7**

derived from the tables presented by Herrmann et al. [90]. Furthermore, note that two tanks are required for each storage material.

According to Table 2.2, the 'no-regen.' and 'low-regen.(2)' configurations are found to be the least efficient, at 58 % efficiency. Following them comes the 'low-regen.' cycle, at 61 % efficiency, and the 'high-regen.' cycle, at 65 % efficiency. This last cycle also presents the lowest cost of storage capacity, at around 16 $/kWh, which is due to the relatively low costs of solar salt and methanol. The other cycles, however, employ mineral oil, which has a high specific cost. If the mineral oil could be replaced by a cheaper alternative such as sunflower oil, the marginal costs of the 'low-regen.' and 'low-regen.(2)' cycles would fall to about 13 $/kWh.

The power densities were computed separately during charge and discharge. During charge, all the regenerated cycles have power densities above 3.4 MW/$\left(\mathrm{m}^3/\mathrm{s}\right)$. During discharge, the power densities drop significantly. The relatively high value for the 'high-regen.' configuration is due to its high discharge pressure ratio, which is higher than its charge pressure ratio (because, in optimal conditions, all heat is rejected through HEX A during discharge).

Note that the 'low-regen.' and 'low-regen.(2)' cycles were computed using neon and helium as working fluids, respectively. In the case of the ‘low-regen.’ system, the choice between neon or helium has negligible impact on the round-trip-efficiency (or any other parameters). However, in the case of the ‘low-regen.(2)’ system, the temperatures are low enough for the properties of neon to significantly depart from ideal behaviour, reducing the efficiency by about 4 percent points, and therefore helium is preferred.

Because of its higher round-trip-efficiency and lower cost of energy capacity, the ‘high-regen.’ cycle is recommended over the other configurations presented in this chapter, and will be used for comparison in the following chapters in this work.

2.7 Concluding remarks

In this chapter, a Joule-Brayton PTES system which employs liquid storage media instead of packed-bed reservoirs has been presented and studied. The following points may be concluded:

- In contrast to systems employing packed-bed reservoirs, using liquid storage media allows the system to simultaneously have unpressurised tanks and a pressurised working fluid. This has important practical and economic implications, since it reduces the cost of the storage tanks and the cost of the turbomachines (which become more compact). Furthermore, each tank remains at a single temperature (i.e. it has no thermal fronts), which decreases self-discharge losses and simplifies operation.

- The round-trip-efficiency of the cycle is very susceptible to compression/expansion losses. These can be minimised by increasing the work ratio of the cycle. Two different strategies have been identified that achieve this purpose: (i) reducing the temperature ratio while keeping the maximum temperature fixed, and (ii) lowering the minimum temperature of the cycle while keeping the temperature ratio fixed.

- The same strategies that minimise compression/expansion losses maximise heat exchanger losses. This results in optimal points at certain operating conditions.

- The cycle can be adapted to the limited temperature ranges of liquid storage media by either employing two (or more) liquids in series or by employing a regenerator, or both. Based on this, four possible cycle configurations that employ specific storage materials have been proposed and numerically studied.

- From the four proposed configurations, a system that employs molten salt for the hot store, methanol for the cold store and a regenerator acting between ambient temperature and the hot store is found to be the most promising. The regenerator improves the work ratio of the cycle, which reaches 65 % round-trip-efficiency based on the performance assumptions made for the different components —90 % polytropic efficiency for compressors/expanders, 97 % effectiveness and 1 % pressure drop for the heat exchangers. Because of the low cost of solar salt and methanol, the cycle has an estimated cost of energy capacity of about 16 $/kWh. Note, however, that there is significant uncertainty in the cost values of the materials and storage tanks on which this figure is based. The mentioned cycle displays an energy density of $46\,\mathrm{kWh/m^3}$ and a power density of $\sim 3\,\mathrm{MW}/\left(\mathrm{m^3/s}\right)$ when the top pressure of the cycle is $\sim 100\,\mathrm{bar}$.

Chapter 3

Combined pumped thermal and liquid air cycles

3.1 Introduction

Pumped thermal energy storage and liquid air energy storage are two strongly related technologies, since both of them store electricity in the form of thermal exergy. Differences arise from the fact that PTES stores the exergy in thermal reservoirs which are filled with external material, while in LAES most of the exergy is stored in the liquid air, which acts both as working fluid and storage material. Furthermore, while PTES transfers exergy to the cold reservoir during charge (and extracts it during discharge), LAES extracts exergy from the cold reservoir during charge in order to perform the liquefaction process (and returns it during discharge). These opposing flows of exergy between the two cycles present a significant opportunity which is explored in here.

This chapter describes a novel, combined system in which PTES operates as a topping cycle and LAES as a bottoming cycle. The fundamental advantage is that the cold thermal reservoirs that would be required by the two separate cycles are replaced by a single heat exchanger that acts between them, thereby saving significant amounts of storage media per unit of energy stored. In order to reach cryogenic temperatures, the PTES cycle employs helium or neon as the working fluid, while the LAES cycle uses supercritical air (at around 150 bar) which is cooled sufficiently to be fully liquefied upon expansion. Importantly, this avoids recirculation of leftover vapour, which enables a better integration with the hot stores (because the same quantity or air is processed during charge and discharge) and simplifies the design and operation of the LAES subsystem.

A thermodynamic study of a baseline configuration of the combined cycle is presented and results are compared with those of the separate systems. These indicate that the new cycle has a similar round-trip efficiency to that of the separate systems while providing a significantly larger energy density. Furthermore, a number adaptations of the base-case combined cycle are proposed and optimised. Most of the adaptations focus on increasing thermodynamic efficiency (the best adaptation significantly exceeds the individual cycles in both energy density and efficiency), while the last adaptation focuses on employing water as the only external storage material (thereby greatly decreasing the cost of storage capacity and enabling storage in much longer time-scales than usual).

In section 3.2, the fundamental aspects of the baseline combined cycle are presented and analysed. The thermodynamic model and underlying assumptions are described, and the nominal operating conditions are selected according to material constraints. A distribution of exergy losses is shown, and the main results of the numerical model are presented in comparison with separate PTES and LAES models based on the same assumptions. Then, in section 3.3, three variations of the combined cycle which aim at further increasing its efficiency are proposed and studied. Since two of these variations introduce new degrees of freedom, a multi-variable optimisation routine is employed to maximise performance within the cycle constraints. Finally, another adaptation which aims at enabling longer storage time-scales is presented and discussed in section 3.4.

3.2 Baseline combined cycle

3.2.1 Motivation

One of the appeals of LAES is its ostensibly high available energy density: the maximum work that can in principle be extracted from liquid air in returning it to ambient conditions is roughly 170 kWh m^{-3} (this compares with 16–26 kWh m^{-3} for compressed air stored at pressures of 120–180 bar). However, a significant fraction of this is required during discharge for the cold recycling process, as described above. To highlight this point, Table 3.1 shows the specific exergy of air ($e = b - b_0$ where $b \equiv h - T_0 s$ is the steady flow availability function and subscript 0 denotes the dead state) at typical conditions for three points in a LAES plant (see Fig. 1.9b for reference). It is striking that roughly half the initial exergetic content of the liquid air is removed in charging the cold store, which, when combined with the additional space requirements of the cold store itself, leads to a very much lower storage density than might originally be expected. This provides the motivation for the proposed combined cycle: rather than storing ‘cold exergy’ during discharge, the additional cooling required prior to liquefaction is provided by the cold side of a PTES topping cycle. There is therefore no need for a cold store for either the LAES or for the PTES plant, and, crucially, these two cycles operate in the same direction (i.e., they are both either charging or discharging together).

Table 3.1: Flow exergy of air at different points of a LAES cycle (see Fig. 1.9b for reference). $T_0 = 290\,\mathrm{K}$ and $p_0 = 1\,\mathrm{bar}$.

Location, discharge	State	T [K]	p [bar]	Exergy [Wh/kg]
Cryogenic tank (1)	Liquid air	78.8	1	195.2
Pump outlet (2)	Supercritical, cryogenic	82	100	197.1
Cold store outlet (3)	Supercritical, ambient	290	100	105.9

3.2.2 Concept and layout

The layout of the proposed combined cycle is shown in Fig. 3.1, together with representative *T*-*s* diagrams of the two subsystems (the operating conditions of which are detailed in Tables 3.2 and 3.3). Helium is assumed as the working fluid for the PTES cycle in here because it is one of the few substances that remains gaseous at air-liquefaction temperatures. Furthermore, it is cheap and has good heat transfer vs. pressure loss characteristics relative to alternatives. On the other hand, due to its low molecular weight, many compression stages are required to achieve a sufficient pressure ratio or temperature rise when using traditional turbomachinery. In this respect, neon may prove a better choice. However, no significant differences in terms of efficiency, energy density or power density were observed between cycle calculations employing helium and neon.

Both the LAES and PTES cycles are assumed to start at ambient temperature and pressure at point 1.[1] Both flows enter a compression process followed by cooling, where the working fluids transfer heat to the storage media. Similarly to the PTES systems in chapter 2, the storage media are assumed to be liquid and heat transfer occurs in counter-flow heat exchangers, but schemes using solid storage (e.g., packed beds) are also possible. As noted in chapter 1, the best option for thermal storage requires a full cost analysis which has yet to be undertaken for the systems currently being considered. For the purposes of this study, and considering the required temperature ranges, a combination of molten salt and thermal oil in series is assumed for the PTES side, while only thermal oil is employed at the LAES

---

[1] It will be seen that, in the baseline combined cycle, the PTES subsystem requires an overall pressure ratio above 100:1. Therefore, pressurising the PTES subsystem would lead to impractically high top pressures. However, some of the adaptations presented later in this chapter require a much lower overall pressure ratio, in which case the PTES subsystem may be pressurised in order to improve its power density.

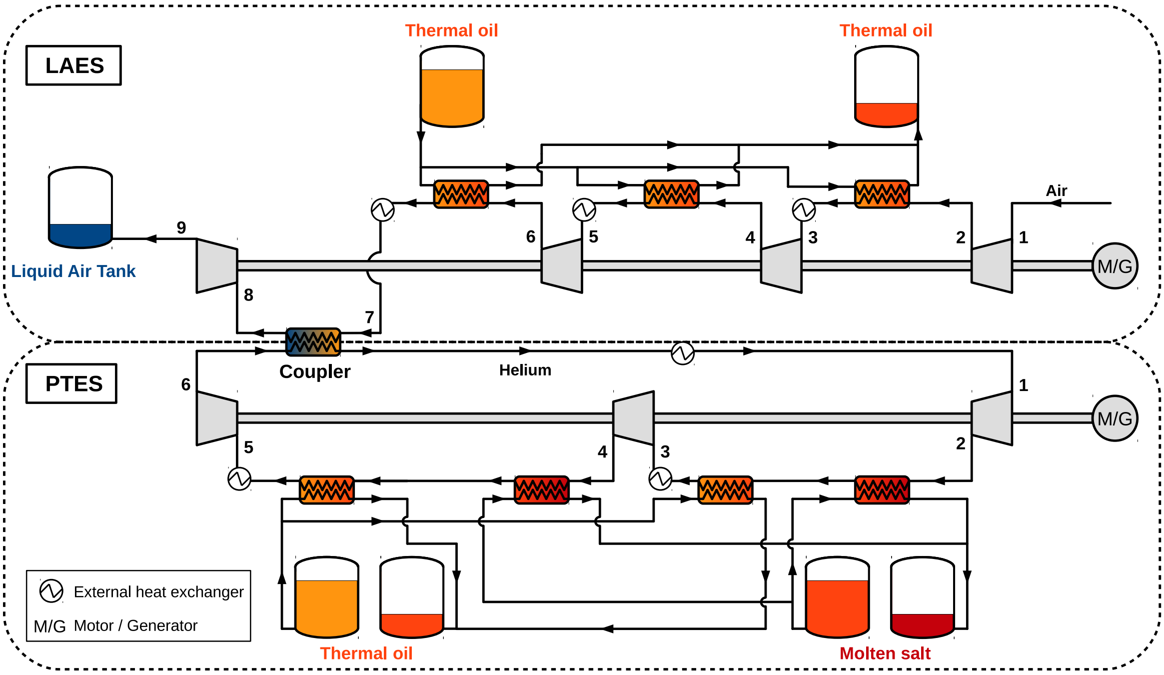

(a) Combined cycle plant layout.

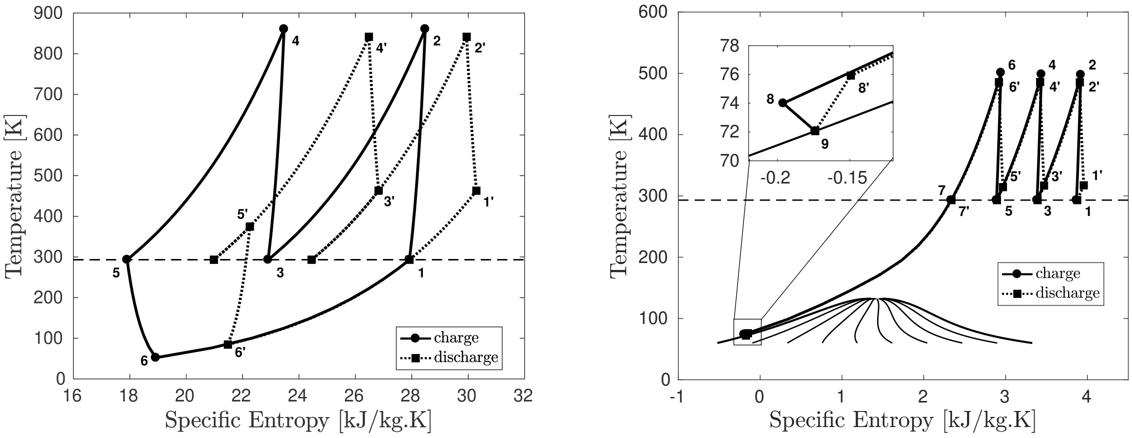

(b) *T*-*s* diagram of the PTES subsystem.

(c) *T*-*s* diagram of the LAES subsystem.

Figure 3.1: Proposed plant layout and *T*-*s* diagrams of the PTES and LAES sub-cycles. Arrow directions refer to charge. Primes ($'$) refer to conditions during discharge.

Table 3.2: State of the helium gas at different points along the PTES subsystem of the combined cycle.

T [K]	p [bar]	$\dot{m}$ [kg/s]	Point
293.1	1.0	10.0	1
872.4	11.6	10.0	2
293.1	11.5	10.0	3
872.2	133.9	10.0	4
293.1	132.6	10.0	5
51.0	1.0	10.0	6
83.5	1.0	10.0	6’
377.4	29.5	10.0	5’
854.8	29.2	10.0	4’
466.7	5.4	10.0	3’
854.8	5.4	10.0	2’
466.6	1.0	10.0	1’

Table 3.3: State of the air at different points along the LAES subsystem of the combined cycle.

T [K]	p [bar]	$\dot{m}$ [kg/s]	Point
293.1	1.0	29.3	1
497.7	5.4	29.3	2
293.1	5.3	29.3	3
498.5	28.5	29.3	4
293.1	28.2	29.3	5
501.2	151.5	29.3	6
293.1	150.0	29.3	7
75.1	148.5	29.3	8
73.1	1.0	29.3	9
73.1	1.0	29.3	9’
77.0	150.0	29.3	8’
293.1	148.5	29.3	7’
485.6	147.0	29.3	6’
314.4	27.8	29.3	5’
485.8	27.5	29.3	4’
316.9	5.2	29.3	3’
485.5	5.1	29.3	2’
317.3	1.0	29.3	1’

side. However, it is notable that thermal oil is relatively expensive, and significant savings could potentially be obtained by using a cheaper alternative such as sunflower oil (see Table 1.1). In this sense, the viability of using vegetable oils as sensible storage materials, considering in particular the topic of thermal stability, should be the subject of future work.

After the working fluids have released the thermal energy into the storage liquids (and because the counter-flow heat exchangers are not perfectly effective), additional ‘low-cost’ (e.g. imbalanced cross-flow) heat exchangers are used to bring the working fluids closer to ambient temperature. Compression and cooling are repeated (once for helium, twice for air), reaching the top pressures of 135 bar (helium) and 150 bar (air) for the case shown. The helium then undergoes a single expansion back to ambient pressure before entering the ‘coupler’, which is the main counter-flow heat exchanger linking the two cycles and which cools the supercritical air down to cryogenic temperatures (between around 60 K and 78 K, depending on the configuration). Finally, the air flows through a cryo-expander (rather than a throttle), resulting in a 100% yield of subcooled liquid air at point 9. The liquid air is then stored at ambient pressure, while the helium returns to the starting point of the closed cycle. During discharge, all processes are reversed.

The combined cycle has two important features that distinguish it from the separate cycles. First, the cold thermal reservoirs of the two systems have been replaced by a single heat exchanger, thus providing significant savings on storage media. Second, the supercritical air can be cooled to temperatures that are low enough for it to be fully liquefied upon expansion. This has several advantages, including: (a) a mechanical expansion device is more readily employed (because the damage associated with two-phase flow has been eliminated), thereby avoiding the significant irreversibility associated with throttling; (b) there is no need for a flash gas recirculation system and (c) the same quantity of air is processed during discharge and charge, thus providing better heat integration with the thermal stores.

It should be pointed out that the present study does not constitute the first proposal for a combined PTES-LAES system. Notably, several possibilities for integrating the two cycles are described in a patent by Isentropic Ltd [77]. These are, however, quite different concepts to that considered here – for example, most are based on sub-critical LAES with a variable-pressure liquid air tank containing “ballast air”; one cycle is supercritical but it does not provide full liquefaction and is devised to work in conjunction with a combustion gas turbine.

3.2.3 Coupling and operation

One difficulty encountered when coupling the LAES and PTES subsystems is that the c_p of helium (or neon) is essentially constant whilst that of supercritical air varies significantly

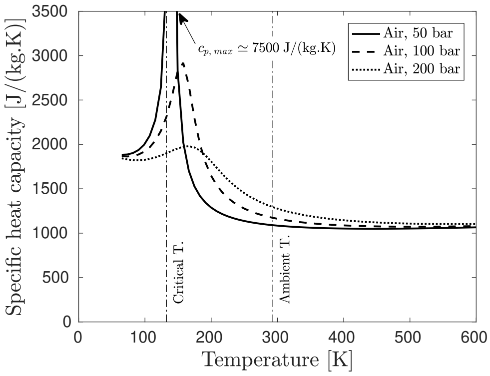

Figure 3.2: Specific heat capacity of supercritical air at three pressure levels.

as it approaches its critical temperature (132.5 K). As shown in Fig. 3.2, this effect is most pronounced at pressures just above the critical pressure (37.9 bar) but becomes less so as the pressure increases. The different c_p variations give rise to pinch points in the air-helium heat exchanger (as shown in Fig. 3.3) which limits cycle performance. There is an optimal mass flow ratio which lies close to that given by

$$\left.\frac{\dot{m}_{\mathrm{air}}}{\dot{m}_{\mathrm{He}}}\right|_{\mathrm{opt}} \simeq \frac{\overline{c_p}_{\mathrm{He}}}{\overline{c_p}_{\mathrm{air}}} \tag{3.1}$$

which leads to $\dot{m}_{\mathrm{air,opt}} \simeq 2.9\dot{m}_{\mathrm{He}}$ when the LAES subsystem is operated at 150 bar.

The pressure ratios of the two sub-cycles are also interlinked because the PTES pressure ratio determines the helium inlet temperature to the coupler whereas that of the LAES cycle affects the shape of the air c_p curve, which in turn influences the air temperature at exit from the coupler. Thus, for a specified liquid air temperature, the charge pressure ratio of the PTES cycle becomes a function of the pressure ratio of the LAES cycle, as will be seen later in section 3.2.5.

The optimal discharge pressure ratio of the LAES cycle is found to be very similar to that during charge and these are therefore taken as equal in the present study. For the PTES cycle, however, the optimal pressure ratio is significantly lower during discharge. This is mainly due to the above-mentioned pinch point issues which mean that prior to compression during discharge (point 6' on the PTES *T*-*s* diagram, Fig. 3.1b) the helium is considerably hotter than at the corresponding point in the charge cycle (point 6). The temperature at this point is important as it has a strong influence on the compression work. In the results that follow, the PTES discharge cycle is always operated at its optimal pressure ratio (based on round-trip efficiency), which is found by iteration.

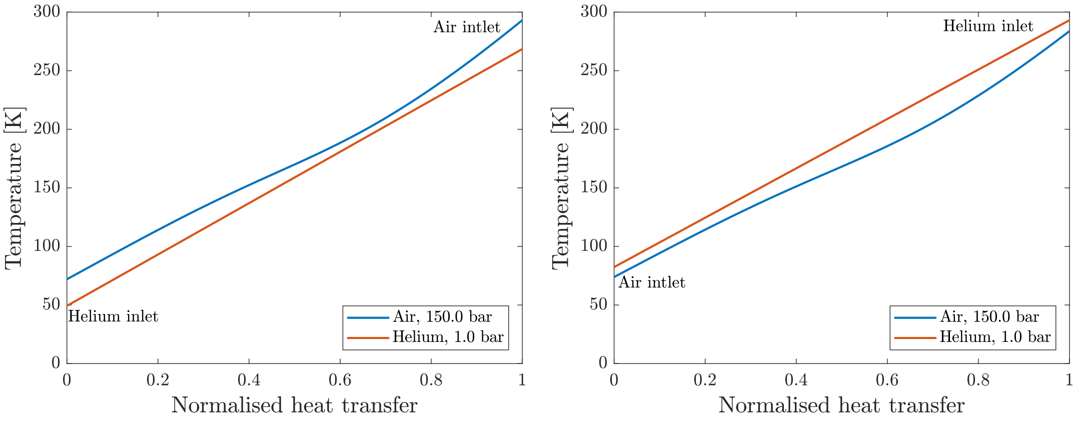

(a) Charge.

(b) Discharge.

Figure 3.3: Temperature distributions inside the coupler during charge and discharge.

3.2.4 Modelling

Similarly to the PTES models in the previous chapter, straightforward ‘design point’ cycle calculations have been undertaken using fixed values of component performance parameters such as compression and expansion efficiency, fractional pressure loss and heat exchanger effectiveness. The modelling of the different components and of the whole cycle is as described in section 2.5. Note that, although the combined cycle produces liquid air during charge, all the components remain in the single-phase region and so no additional modelling complexity is introduced.

The nominal performances of the different components is also the same as in the previous chapter: $\eta_\mathrm{c} = \eta_\mathrm{e} = 0.9$, $\varepsilon = 0.97$ and $f_p = 0.01$. Note that a 90% efficiency is realistic for state-of-the-art turbomachinery, but may be a slight overestimate for the cryo-expander (see [107], in which a value of 88% is reported for cryogenic liquid expanders in the context of LNG). However, the corresponding work term is very small (as is the pump work during discharge) and so small changes in the efficiency of this component have negligible impact on the overall performance.

3.2.5 Selection of operating conditions

In order to determine the best overall pressure ratios, a parametric study of the combined cycle was performed, the results of which are presented in Fig. 3.4. The LAES pressure ratio was varied from 100 bar to 300 bar, while that for PTES was automatically adapted to obtain specified liquid air temperatures, T_LA. In the plots shown, three curves are presented according to three different T_LA values: low (60 K – i.e., just above the triple point for air), medium (70 K) and high (78.5 K – i.e., just below the boiling point at ambient pressure).

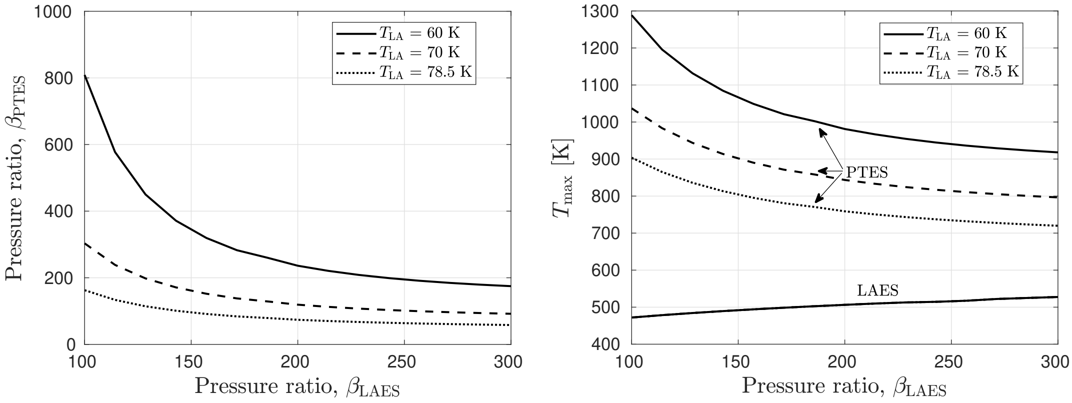

(a) PTES pressure ratio.

(b) Maximum temperatures.

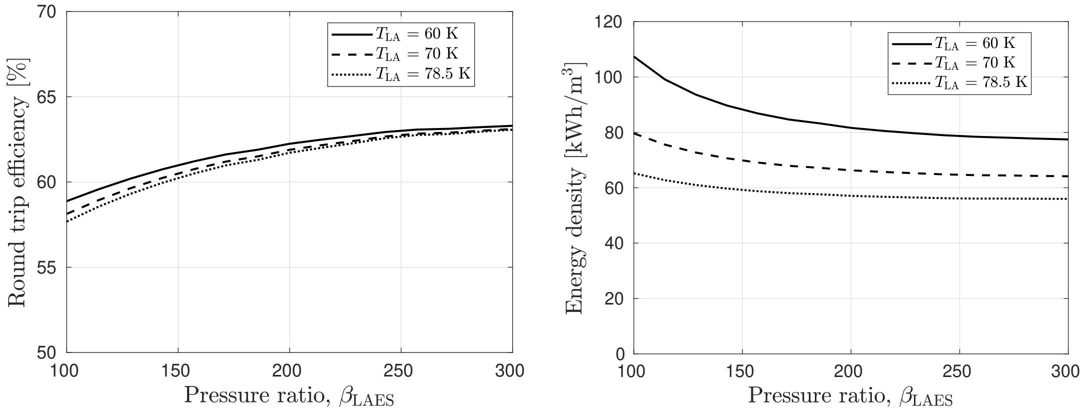

(c) Efficiency.

(d) Energy density.

Figure 3.4: Parametric study of the combined cycle. Variation of relevant parameters with the pressure ratio of the LAES subsystem, β_{LAES}, and the temperature of the liquefied air, T_{LA}.

As the overall pressure ratio of the LAES cycle, β_{LAES}, increases, that of the PTES cycle, β_{PTES}, decreases (see Fig. 3.4a). The dependence is particularly strong for low values of β_{LAES} but then falls off due to the less severe variations in c_p of supercritical air at higher pressures, as explained in section 3.2.3. Low liquid air temperatures require a higher β_{PTES} so that the helium is sufficiently cold after expansion. Maximum temperatures for the two sub-cycles are shown in Figure 3.4b, from which it is apparent that a combination of low β_{LAES} and low liquid air temperature leads to impractically high top temperatures in the helium circuit.

Figure 3.4c shows that the round-trip efficiency of the combined cycle increases with β_{LAES}. This again stems from the temperature dependence of c_p for supercritical air, which is smaller at higher pressure and thus allows better performance of the coupling heat exchanger. The efficiency is, however, almost independent of T_{LA}. This is due to two conflicting factors which tend to cancel one another: at low T_{LA} pinch point problems are more severe, but the correspondingly higher β_{PTES} improves the work ratio (and thus the performance) of the PTES system.

Finally in this section, Figure 3.4d shows variations of the overall energy density, ρ_{E}. The energy density exhibits the opposite trend to that of efficiency in that it decreases with β_{LAES} at fixed T_{LA} . This is because (as noted earlier) increasing β_{LAES} requires a reduction in the PTES pressure ratio, which in turn reduces the temperature and exergy density of the PTES storage media. Since the PTES plant provides the largest fraction of the stored exergy (typically $\sim 60\,\%$), the value of β_{PTES} has a dominant effect on the overall energy density. This also means that ρ_{E} increases with decreasing T_{LA}, as shown by the different curves in Fig. 3.4d.

On the basis of the previous discussion, a baseline design is proposed with a top LAES pressure of 150 bar and liquid air temperature of 73 K. The maximum PTES temperature is then about 870 K (while the maximum LAES temperature is about 500 K), thereby avoiding the excessive cost of higher-temperature materials. Even so, the overall pressure ratio of the PTES cycle is 135:1, requiring two compressors, each with around 12:1 pressure ratio. This would imply many rotor-stator stages (or very high blade speeds) if accomplished by turbomachinery due to the high value of c_p for helium, and it may be preferable to undertake some of the compression (and expansion) with positive displacement devices. Alternatively, neon could be used in place of helium as the working fluid, or the LAES pressure ratio could be raised. (In this respect, the authors of Ref. [62] specify a pressure limit of 250 bar based on published values for supercritical steam plant.) Ultimately, the best choices require a full thermo-economic optimisation, but this is beyond the scope of the present study.

3.2.6 Loss distribution

Having established the baseline operating conditions, a second law analysis is applied to the combined cycle to determine the distribution of exergetic losses. The method for computing the lost work in each component is the same as detailed in the previous chapter, in section 2.5.4. Additionally to the loss terms shown in Table 2.1, a loss term associated with the entropy of mixing must be computed, since, as shown in Fig. 3.1a, several liquid streams coming from different heat exchangers are stored in the same tanks. Mixing of gas flows does not occur in the baseline combined cycle but it occurs in some of the adaptations shown later in this chapter. For both liquids and gases, the entropy generation due to (isobaric) mixing is computed via:

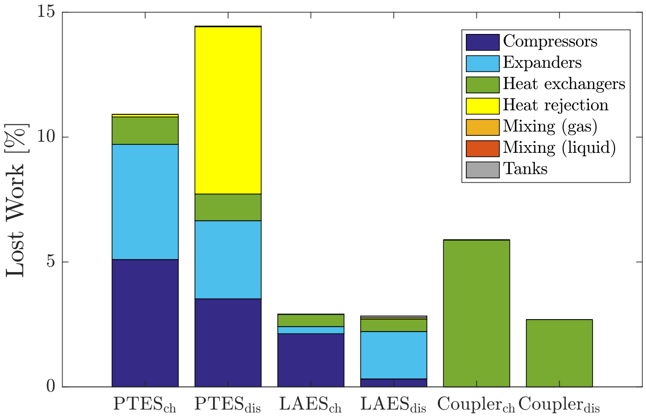

Figure 3.5: Distribution of exergetic losses for the baseline configuration of the combined cycle ($\text{PR}_{\text{LAES}} = 150$, $T_{\text{LA}} = 73$ K), shown as a fraction of the total net work input during charge. The different bars correspond to the PTES subsystem, the LAES subsystem and the main heat exchanger (the Coupler), during charge and discharge.

$$\dot{S}_{\text{irr}} = \dot{m}_{\text{out}} s_{\text{out}} - \sum_i (\dot{m}_{\text{in}} s_{\text{in}})_i$$

Fig. 3.5 shows the distribution of exergetic losses in the baseline combined cycle. The biggest losses occur in: (i) the compression and expansion machinery of the PTES subcycle; (ii) the main heat exchanger linking the cycles and (iii) heat rejection above ambient temperature (at around 200 °C) from the PTES system during discharge. This last loss could be reduced by an additional bottoming cycle (e.g., based on an ORC) at the expense of additional complexity and capital cost. Alternatively the rejected heat might be exploited for other purposes.

Mixing losses in the liquid streams are reduced almost to zero by using the same pressure ratio for each phase of compression/expansion. Likewise, losses that would occur due to the tanks not being fully discharged are avoided by using the same mass flow ratios (i.e., between air, helium and storage liquids) for charge and discharge. Finally, as already noted, the losses associated with the cryogenic expander and the corresponding liquid air pump are small due to the small work transfers for these devices.

3.2.7 Comparison with stand-alone cycles

In this section, the performance of the combined cycle is compared to those of independent PTES and LAES. The stand-alone systems used for comparison are those presented in Fig. 2.11b (‘high-regen.’ PTES) and Fig. 1.9 (LAES with cold recycling). The main differences between them and the subsystems within the combined cycle are as follows:

- In the case of PTES, the stand-alone cycle has one single compression phase and above-ambient regeneration, while the subsystem of the combined cycle has two compression phases and no regeneration, which leads to a much larger pressure ratio. The stand-alone cycle uses molten salts and methanol for the hot store and cold store, respectively, while the subsystem uses molten salts and thermal oil for the hot store but requires no cold storage. Finally, the independent cycle employs nitrogen as working fluid, while the subsystem requires helium (or neon) instead.
- In the case of LAES, the two systems are very similar in terms of operating conditions, but the stand-alone cycle requires a cold store and recirculation of a fraction of non-liquefied air. More specifically, the supercritical air is cooled by two heat exchangers connected in series to two double-tank liquid reservoirs containing methanol and propane, similar to the system described by Guizzi et al [65]. For the system to be stable over several cycles, each of the storage liquids must be returned to the same temperature after each complete charge-discharge cycle. However, not all the air is liquefied during charge and the flash gas is thus recirculated. Although this contributes to the cooling of the incoming air, the specific heat capacity of the flash gas is much lower than that of supercritical air and consequently the cooling required during charge is greater than that supplied during discharge. This difficulty is resolved by adjusting the ratio of mass flow rates between the air and cooling fluids during the discharge cycle. This enables the cold thermal storage to be fully re-charged, at the expense of slightly greater heat transfer irreversibility. Another challenge of the stand-alone cycle is that the cryo-expander operates at very complex conditions due to the two-phase flow with very low vapour quality. Because of this, a more conservative value is assumed for the polytropic efficiency of this component ($\eta = 0.70$, in line with the study in [65]) when modelling the cycle, while the performance of all other compressors/expanders is kept at the default value ($\eta = 0.9$).

The results of the comparative study are summarised in Table 3.4. The efficiency of the combined cycle is around 60%, similar to stand-alone LAES[2] but about 5 percent points below stand-alone PTES. The main benefit of the combined cycle, however, lies in the significant improvement in energy density, exceeding by 40% and 140% those of the individual PTES and LAES systems, respectively, due to the removal of the cold storage systems.

---

[2] It should be noted that, due to the difficulties associated with operating expanders in the two-phase region, practical (stand-alone) LAES might employ a throttle instead of a mechanical expander, and in this case the efficiency would fall dramatically, by more than 20 percent points, due to the reduced liquid air yield during charge. For comparison, were a throttle to be employed in the combined cycle it would incur a much smaller efficiency penalty of just 3 percent points. This is because conditions downstream of the throttle remain in the fully liquid state for the combined cycle case.

Table 3.4: Comparison between the stand-alone cycles and the combined cycle. The single PTES system refers to the 'high-regen' cycle in Fig. 2.11b. The single LAES system refers to the Linde-based adaptation in Fig. 1.9. The combined cycle refers to the baseline configuration in Fig. 3.1.

Parameter	Single PTES	Single LAES	Combined Cycle
Efficiency [%]	**65.2**	**61.0**	**60.4**
Energy density [kWh/m^3]	46.2	27.4	65.7
Work ratio (charge) [-]	3.8	36.1	4.3 (PTES) 43.1 (LAES)
Solar Salt [t/MWh]	15.7	-	6.2
Mineral Oil [t/MWh]	-	10.6	8.1
Methanol [t/MWh]	10.4	4.7	-
Propane [t/MWh]	-	8.2	-
Liquid air [t/MWh]	-	7.4	2.7
Cost materials [\$/kWh]	11.0	22.5	16.1
Cost tanks [\$/kWh]	4.6	4.3	2.7
Total cost [\$/kWh]	**15.5**	**26.8**	**18.7**

The table also shows the estimated cost of energy capacity of each cycle, computed in the same way as in section 2.6.[3] Despite its larger energy density, the combined cycle fails to obtain a lower cost of energy capacity than stand-alone PTES. This is due to the high price of mineral oil, which is employed for the combined cycle but not for the 'high-regen.' PTES configuration. However, if the mineral oil could be substituted by a cheaper alternative, such as sunflower oil, the cost of energy capacity of the combined cycle would drop from 19 \$/kWh to 8 \$/kWh, while stand-alone PTES would remain at around 16 \$/kWh. This possibility, therefore, provides an important argument in favour of the combined cycle and justifies further research in this direction.

---

[3] To summarise: the estimated cost of energy capacity includes the costs for the storage materials (as presented in Table 1.1) and the costs of the tanks. A cost of 50 \$/m^3 is used for all the tanks except for the solar salt tanks, for which a value of 150 \$/m^3 is used. A factor of 20 % to the cost of each tank is added to account for insulation. Two tanks are assumed to be required for each storage material, except for the liquid air, which only requires one tank.

3.2.8 Sensitivity to loss parameters

Results thus far have been obtained with fixed values of compression and expansion polytropic efficiencies (η) and heat exchanger effectivenesses (ε). The effect of varying these parameters is shown in Figure 3.6. It is apparent that the stand-alone LAES is the least sensitive to variations in η, this being due to its high work ratio, but is also the most sensitive to variations in ε, because it impacts directly on its liquefaction yield during charge. On the other hand, the most sensitive to variations in η is the stand-alone PTES, which has a comparatively low work ratio. The stand-alone PTES and the combined cycle present similar sensitivity to variations in ε. Conclusions regarding the relative merits of the different systems are, however, unaffected by the values of η and ε.

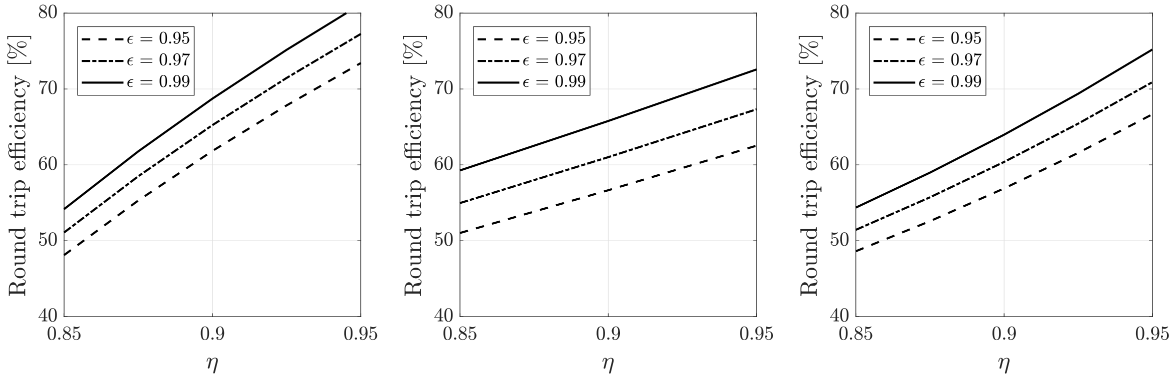

(a) Stand-alone PTES **(b)** Stand-alone LAES **(c)** Combined Cycle

Figure 3.6: Sensitivity study.

3.3 Developments aimed at high performance

The basic combined cycle as described above may be modified in many different ways with the aim of improving its performance. Three such modifications are considered here.

3.3.1 Asymmetrical LAES stages

When considering the design of a typical air liquefaction plant, one would normally aim at minimising the compression work required per kilogram of liquefied air. One strategy to achieve this (apart from making use of high performance components) is to make use of multiple, intercooled stages, in order to approach a quasi-isothermal compression process. Such a strategy might also be useful for a LAES plant which has access to a medium-

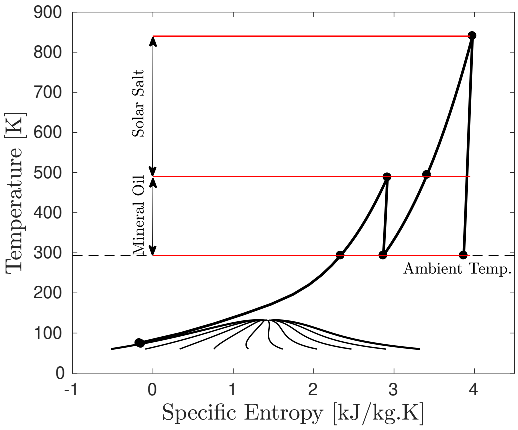

Figure 3.7: T-s diagram of the LAES subsystem employing two asymmetrical compression stages. The thermal energy released after the first stage is stored in Solar Salt and mineral oil tanks, while the second one only uses mineral oil.

grade heat source[4] and which therefore does not need to store the "heat of compression". However, in the case of a completely independent plant (as in the systems described above), the thermal energy delivered during charge must be stored and returned to the air before expansion during discharge. In this case, the approach that results in the highest energy and power densities is to *maximise* the compression work. For a given pressure ratio, the work input will be maximum if a single adiabatic compression phase is employed. However, for the pressure ratios that the LAES subsystem (or any LAES plant) requires, this would result in air temperatures too high to be practicable.

A reasonable compromise is to use two (rather than three) compression stages for the LAES subsystem, with an asymmetric pressure ratio split as shown in Fig. 3.7. The pressure ratios are selected such that the temperature after the first stage is 870 K —i.e., at the solar salt limit, like in the PTES subsystem— and after the second stage is about 500 K. With this modification, the energy density of the combined cycle is boosted to $74.2\,\mathrm{kWh/m^3}$ and the round-trip efficiency is improved to 62.5%. While the increase in energy density can be easily understood from the above-discussion, the increase in round-trip efficiency stems from the fact that, within the combined cycle, the LAES subsystem is more efficient than the PTES subsystem (see section 3.3.3 for a detailed discussion on this). The asymmetrical stages increase the power input and output coming from the LAES subsystem, while the PTES subsystem remains unchanged. Therefore, the LAES subsystem gains 'weight' within the combined cycle, which improves the overall efficiency.

---

[4] E.g. heat rejected by an industrial process or a power plant, or a renewable heat source such as geothermal or solar power.

3.3.2 Multi-stream heat exchanger

As previously shown in the loss distribution in Fig. 3.5, the main heat exchanger linking the PTES and LAES cycles is one of the biggest sources of irreversibility, typically causing around 20% of the total loss. This is essentially due to the pinch point issues discussed before. One way to reduce the associated loss is to employ a multi-stream heat exchanger that has two levels of helium mass flow so as to more closely match the values of $\dot{m}c_p$ for the hot and cold streams. The resulting plant structure is more complex than before, but the main features of the modified system are as follows (see Fig. 3.8 for the layouts and *T*-*s* diagrams).

During charge (Fig. 3.8a), secondary streams of helium are extracted from part way through the second compression (point 1s) and part way through the coupling heat exchanger (point 4s). Heat is recuperated between these streams from points 2s to 3s and points 4s to 5s, respectively. The coupling heat exchanger thus has two different helium mass flow sections which allows better integration with the air stream, as shown in Fig. 3.9. The net result is that, for a given helium inlet temperature (point 6), the air is now cooled to a lower exit temperature, implying that less exergy is destroyed and more transferred to the liquid air storage tank. This effect is sufficiently pronounced that with the same operating conditions as those of the original combined cycle the air temperature would drop below the triple point after expansion and thus freeze. The overall pressure ratio of the PTES cycle is therefore reduced so that T_{LA} remains above 60 K. Similar modifications are made for the discharge cycle (Fig. 3.8b), but due to the lower pressure ratio during discharge there is only one expansion stage for the secondary helium flow, contrasting with the two compression stages during charge.

The modified cycle has more degrees of freedom than the original one in that, in addition to the discharge pressure ratio of the PTES subsystem, the following parameters must also be specified: the fraction of mass flow in the secondary helium stream; the pressure ratios for the secondary stream during both charge and discharge and the ratio between the mass flow of air and the total mass flow of helium. These parameters were chosen by optimising for round-trip efficiency using a constrained, non-linear, multi-variable optimisation algorithm, which is based on the interior point method [108] and is readily available in Matlab. When the optimised values are employed, the hot and cold streams of the coupling heat exchanger match much better than in the original cycle (contrast Fig. 3.9 with Fig. 3.3) and, in conjunction with the asymmetric compression stages described above, a round-trip of efficiency of 65.1% is achieved at an energy density of 78.1 kWh/m^3 and an energy capacity cost of 15 \$/kWh.

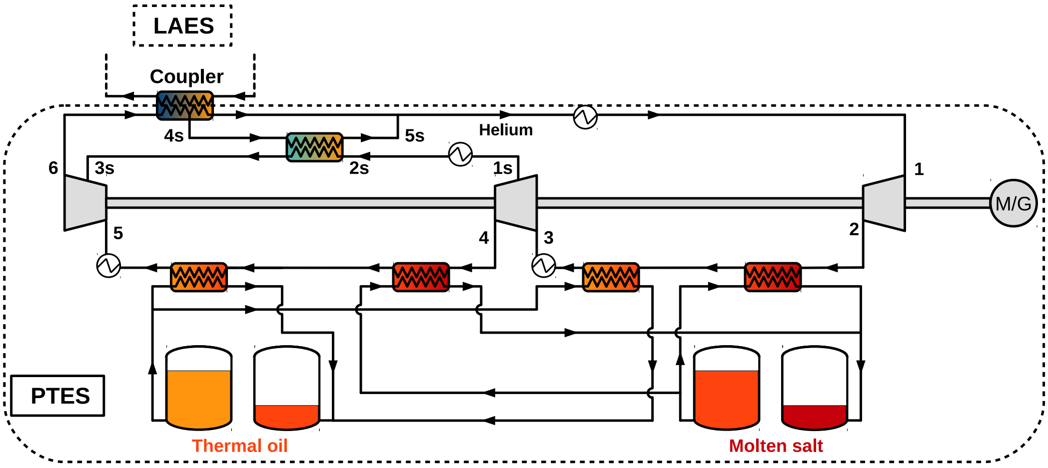

(a) Plant layout (charge).

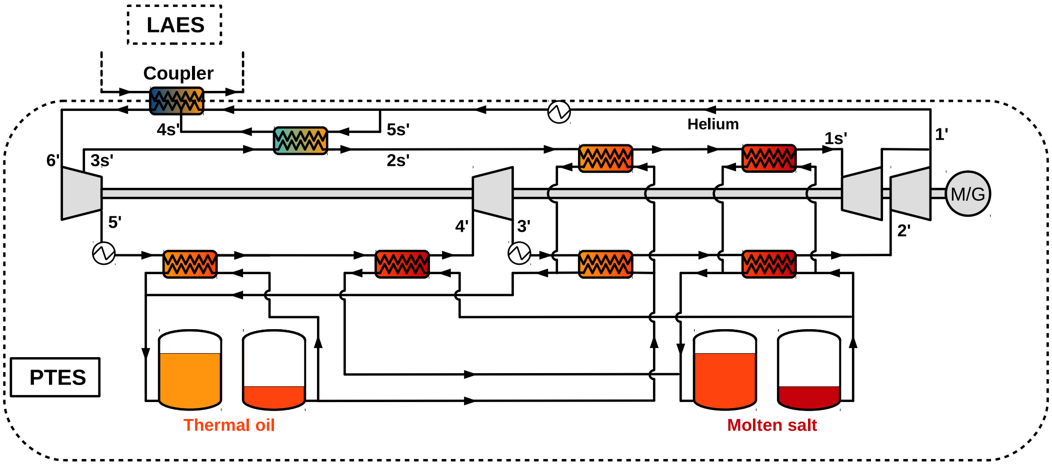

(b) Plant layout (discharge).

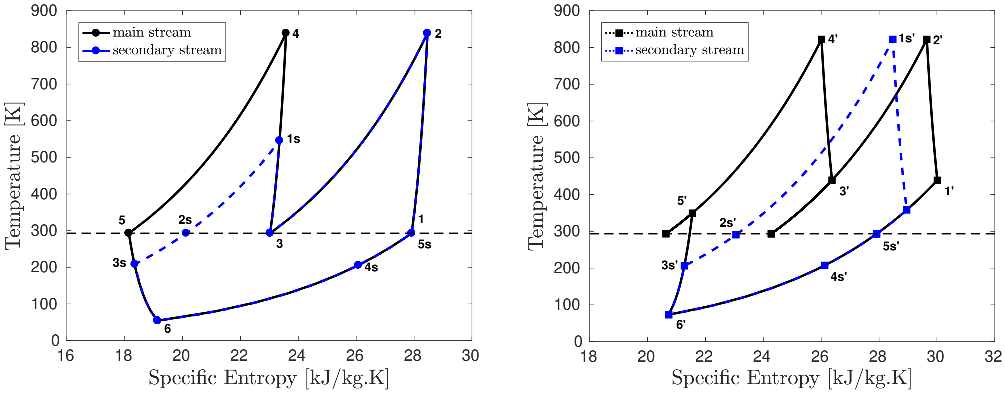

(c) T-s diagrams of the PTES subsystem. Left: charge. Right: discharge.

Figure 3.8: Adaptation of the combined cycle to allow different levels of helium mass flow rate at two different sections of the coupler. The layout of the LAES subsystem is like that of Figure 3.1 but employing the asymmetrical compression and cooling stages described in section 3.3.1. An “s” after a number denotes the secondary stream. Primes ($'$) refer to discharge.

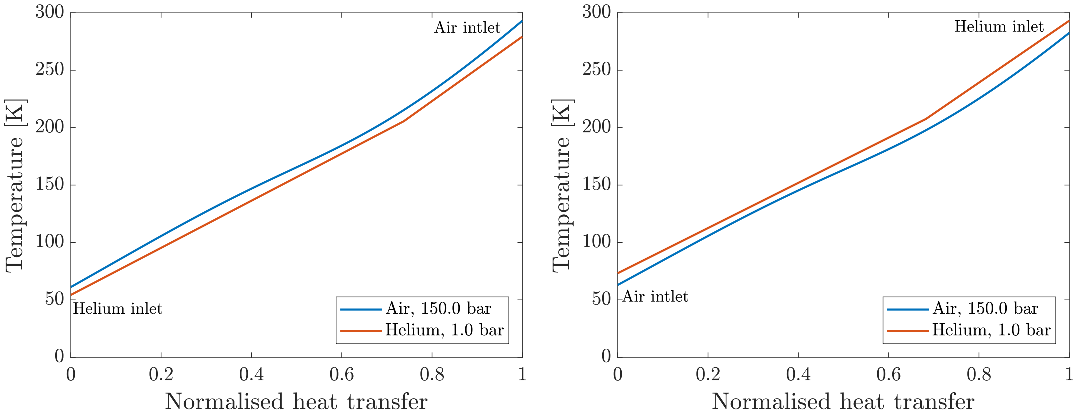

(a) Charge.

(b) Discharge.

Figure 3.9: Temperature distributions inside the multi-stream coupler.

3.3.3 Supercritical air pre-cooling

By looking again at the loss distribution shown in Fig. 3.5, one can see that the largest fraction of the losses comes from the PTES subsystem. The main reasons for this are: (i) the LAES subsystem has a much higher work ratio than the PTES subsystem, (ii) the irreversibility within the coupling heat exchanger requires additional heat to be rejected from the PTES subsystem—note that the air essentially retraces the same state path during charge and discharge, whereas the helium must be colder than the air during charge, but hotter than it during discharge, which leads to a lower PTES discharge pressure ratio and to high heat rejection losses—, and (iii) the PTES subsystem is the largest contributor to the total power input and output of the plant. This last aspect is shown in Table 3.5a, which presents the net work inputs and outputs for the unmodified combined cycle and its subsystems. The tabulated figures also show how the efficiency of the LAES subsystem is much higher than that of the PTES. However, the efficiency of the combined cycle is weighted more towards that of the PTES subsystem due to the larger work exchanges of the latter.

These observations suggest that the overall cycle efficiency can be improved by raising the efficiency of the PTES subsystem and reducing its share of the work input and output. This is achieved here by use of a regenerative helium cycle, with just one (rather than two) compression phases, as shown in Fig. 3.10a. Apart from increasing the work ratio and reducing the overall pressure ratio of the PTES subsystem, the regenerator means that the main helium-to-air heat exchanger operates over a narrower temperature range and so some pre-cooling of the air (i.e., by cold recycling) is required to compensate for this. The net result is that the efficiency increase is obtained at the expense of a slightly lower energy density.

Table 3.5: Net work inputs and outputs for each subsystem and for the overall combined cycle. The figures shown in the table are for an arbitrary helium mass flow rate of $10\,\mathrm{kg/s}$ and for a charge (and discharge) time of 10 h at constant power, but calculations are undertaken on a specific (per unit mass flow) basis.

(a) Baseline combined cycle.

Parameter	PTES subsystem	LAES subsystem	Combined Cycle
Net work input, charge (MWh)	475	180	655
Net work out, discharge (MWh)	250	146	396
Efficiency (%)	**52.6**	**80.9**	**60.4**

(b) Combined cycle with helium regeneration and supercritical air pre-cooling, also employing the asymmetrical compression and cooling stages described in section 3.3.1.

Parameter	PTES subsystem	LAES subsystem	Combined Cycle
Net work input, charge (MWh)	246	194	440
Net work out, discharge (MWh)	150	162	312
Efficiency (%)	**60.9**	**83.6**	**70.9**

A number of common alcohols and hydrocarbons are suitable as storage media for the pre-cooling phase. Methanol has been used to generate the results presented here because of its low cost, but ethanol, which is also relatively inexpensive, could be used instead. As with the main coupling heat exchange process, incompatible temperature dependence of c_p for air and methanol leads to pinch point issues, but these are readily rectified by incorporating an intermediate temperature methanol tank, thereby allowing two independent methanol mass flow rates (see Fig. 3.10c). Finally, an additional small improvement is obtained by introducing a secondary compressor that acts only during discharge and that allows an increase in the discharge pressure ratio and thus rejection of heat at lower temperatures, as can be seen between points 3a' and 3b' of the T-s diagram in Fig. 3.10b. Details about the temperature and pressure conditions along the cycle are shown in Tables 3.6 and 3.7.

The main work transfers of the modified cycle (which also includes the asymmetrical stages of the LAES subsystem) are shown in Table 3.5b. Noticeably, a significant increase in round-trip efficiency is achieved, reaching 70.9 % while displaying an energy density of $63.3\,\mathrm{kWh/m^3}$ (which is similar to the energy density of the baseline combined cycle despite the presence of the additional methanol tanks[5]).

---

[5] The decrease in energy density due to the additional pre-cooling tanks is compensated by the increases due to the asymmetrical stages of the LAES subsystem and the higher efficiency of the cycle.

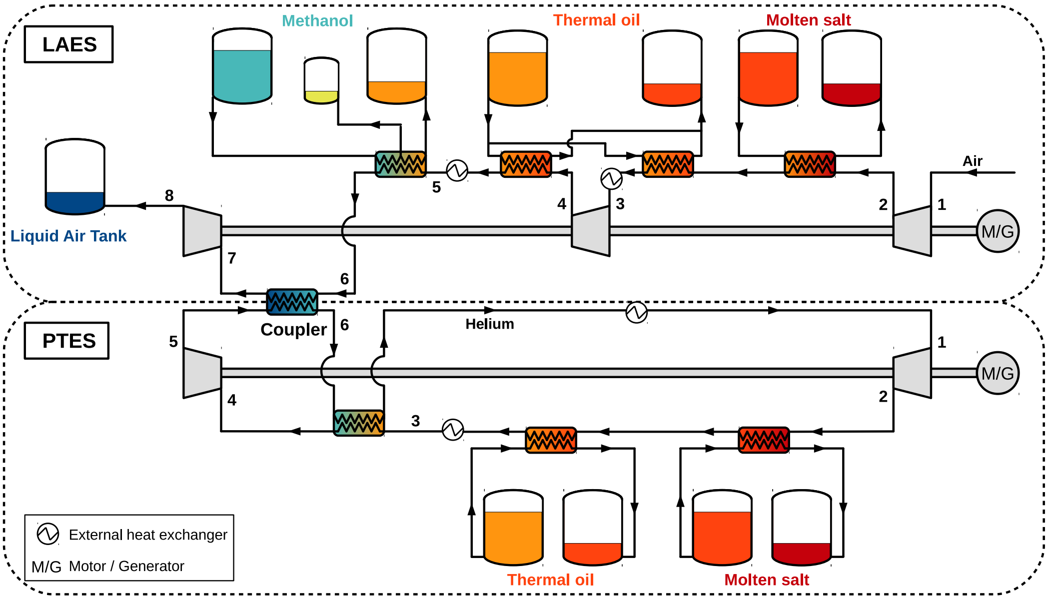

(a) Plant layout.

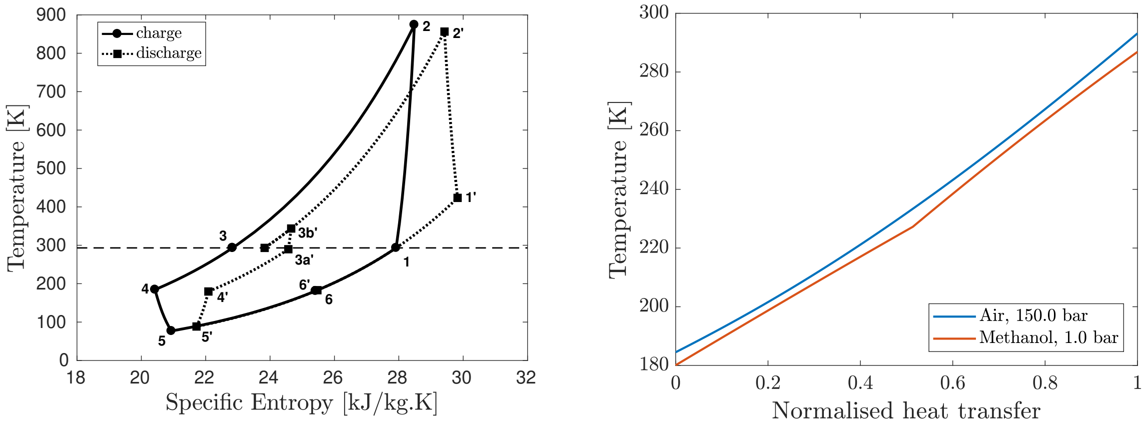

(b) T-s diagrams of the PTES subsystem.

(c) Temperature distribution inside the air-methanol heat exchanger.

Figure 3.10: Proposed adaptation of the combined cycle, employing a regenerated PTES cycle and pre-cooling of the supercritical air. (a) Plant layout shown during charge. All processes are reversed during discharge, with the exception of an additional secondary compressor which is introduced in the PTES subsystem during discharge (points 3a′ to 3b′). (b) T-s diagram of the PTES subsystem. Primes (′) refer to conditions during discharge. (c) Temperature distribution in the multi-stream heat exchanger which transfers heat between the supercritical air and the cold storage medium (methanol), during the pre-cooling phase.

Table 3.6: State points of the helium gas flowing in the PTES subsystem of the combined cycle (pre-cooling configuration).

T [K]	p [bar]	$\dot{m}$ [kg/s]	Point
293.1	1.0	10.0	1
873.9	11.7	10.0	2
293.1	11.6	10.0	3
184.4	11.6	10.0	4
76.8	1.0	10.0	5
181.0	1.0	10.0	6
183.2	1.0	10.0	6’
88.5	1.0	10.0	5’
179.8	4.9	10.0	4’
289.7	4.9	10.0	3a’
342.6	7.1	10.0	3b’
856.4	7.0	10.0	2’
424.0	1.0	10.0	1’

Table 3.7: State points of the air flowing in the LAES subsystem of the combined cycle (pre-cooling configuration).

T [K]	p [bar]	$\dot{m}$ [kg/s]	Point
293.1	1.0	25.6	1
840.4	30.7	25.6	2
293.1	30.4	25.6	3
488.2	150.0	25.6	4
293.1	150.0	25.6	5
184.3	148.5	25.6	6
80.5	147.0	25.6	7
78.1	1.0	25.6	8
78.1	1.0	25.6	8’
82.5	150.0	25.6	7’
177.0	148.5	25.6	6’
280.7	147.0	25.6	5’
477.5	147.0	25.6	4’
315.5	30.1	25.6	3’
816.7	29.8	25.6	2’
352.0	1.0	25.6	1’

This last adaptation of the combined cycle significantly exceeds the individual stand-alone cycles in both efficiency and energy density and is, therefore, particularly appealing. The estimated cost of storage capacity becomes 15 $/kWh, which is very similar to that of the stand-alone PTES system, or 8 $/kWh if the mineral oil can be substituted by sunflower oil. Furthermore, this adaptation is also less complex than the multi-stream coupler adaptation, and makes the PTES subsystem more comparable to its stand-alone counterparts. Particularly, the smaller pressure ratio of the PTES subsystem (which is of the order of 12:1, rather than 135:1) allows pressurisation of the low pressure line and an increase in the power density of this subsystem, similarly to the cycles studied in chapter 2.

3.4 Developments aimed at long-term energy storage

Perhaps the most notable characteristic of the baseline PTES-LAES combined cycle is that it removes the need for a cold store, such that all the exergy is stored in the hot store and in the liquid air tanks. Here the possibility of additionally removing the hot store is explored, such that all the exergy is stored in the liquid air tanks. This would be very advantageous from an economic point of view, since the liquid air tanks are much cheaper than the hot/cold stores for obvious reasons (the storage medium is free and only a single tank is needed to store all the liquid air, while two tanks are typically required for each hot/cold storage material[6]). Such a scheme would dramatically reduce the cost associated with energy capacity and potentially enable plants with significantly larger storage capacities (e.g. charging/discharging times of several days or weeks rather than several hours).

Removal of the hot store may be achieved by employing near-isothermal (rather than adiabatic) stages in the compression train during charge, and near-isothermal stages in the expansion train during discharge. This approach has already been proposed and tested for some CAES systems (known as I-CAES —isothermal CAES— systems) in which all the exergy is stored in the compressed air [18]. Isothermal compression/expansion can be realised by employing reciprocating or rotary machines, but has the disadvantage that the power rating is limited by the heat transfer rate [110]; in order words, a trade-off appears between power density and isothermal efficiency. Research is therefore being focused on increasing the heat transfer rate, which may be achieved in several ways, such as (i) spraying fine liquid droplets which exchange heat with the gas during the compression/expansion process

---

[6] The two-tank system is the traditional system employed in most commercial CSP power plants, although thermocline systems that employ a single tank and significantly reduce the amount of liquid storage media required (by embedding a low-cost solid filler material inside the tank) have also been proven at large scale [109]. However, thermocline systems imply further operational complexity and higher self-discharge losses due to their internal thermal fronts.

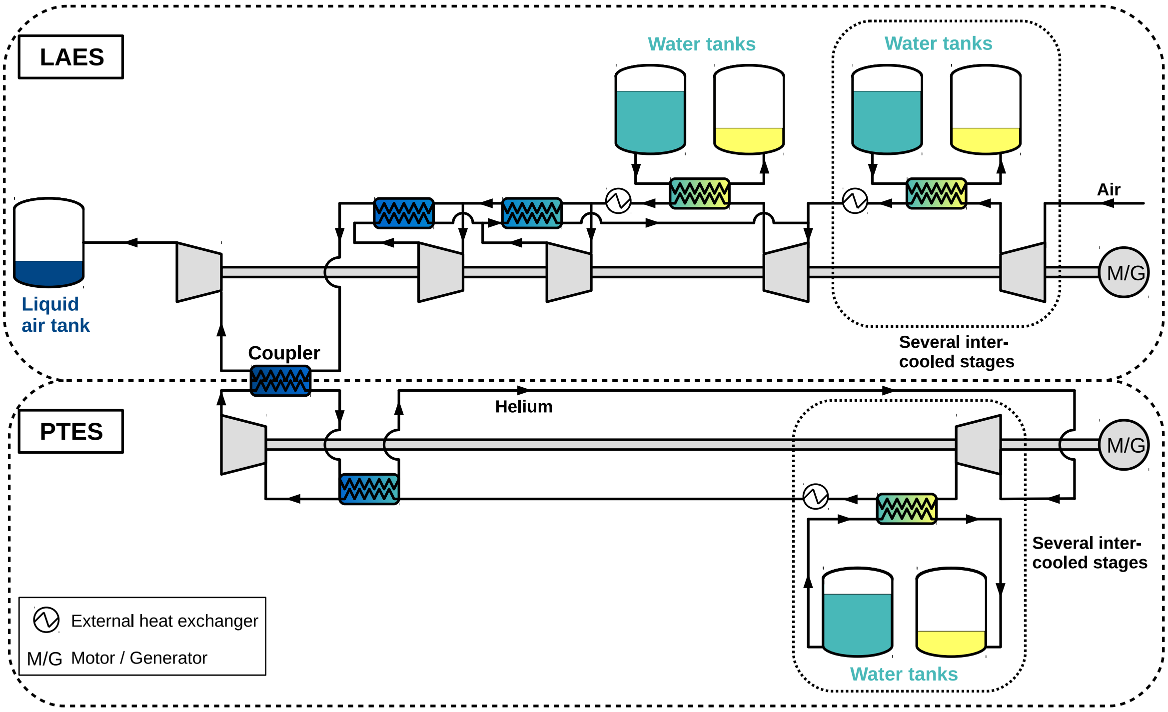

Figure 3.11: Layout of the ‘low-temperature’ adaptation of the combined cycle, operating with water and liquid air as storage media, shown during charge. All processes are reversed during discharge.

[21, 111] or (ii) using a liquid piston in combination with high-surface-density materials which are introduced inside the piston chamber [112]. Following the latter approach (using porous media inserts), experimental results by Yan et al. [113] show that isothermal compression efficiencies of 95 % (and isothermal expansion efficiencies of 90 %) are possible at a power density of $\sim 150\,\mathrm{kW/m^3}$.

Since, unfortunately, the isothermal compression technology is still at a development stage, a different scheme will be used here, in which several intercooled stages are employed for the (charge) compression and (discharge) expansion trains. This approach, which is similar to that of low-temperature CAES [114], does not succeed in removing the hot store but still enables a large reduction in its cost.

The proposed plant layout (referred to as ‘low-temperature’ adaptation) is presented in Figure 3.11. T-s diagrams of the two subsystems are presented in Figure 3.12. Employing several intercooled stages lowers the top temperature of the cycle, which allows water to be used as storage medium in unpressurised tanks. This is not quite the same as an isothermal scheme without hot store, but it may still be expected to cut the cost of storage capacity because the cost of water is negligible and because unpressurised tanks operating below 100 °C may be built with cheap (e.g. plastic-based) materials.

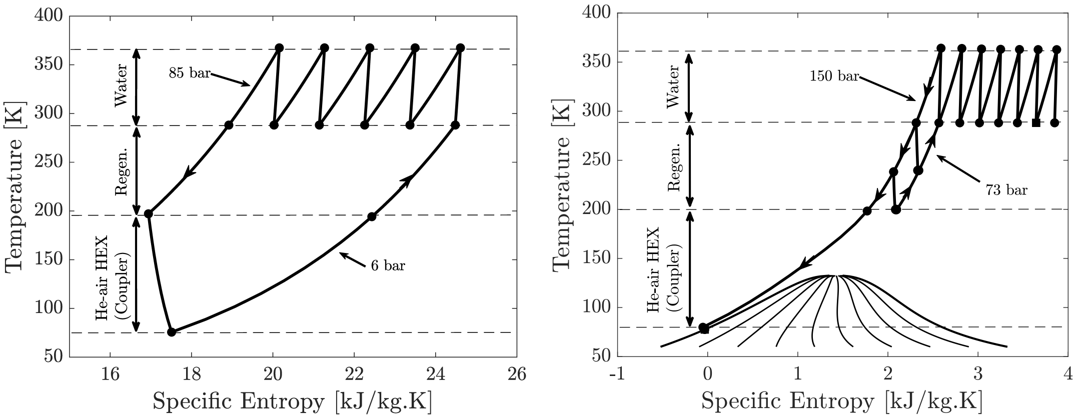

(a) PTES subsystem. **(b)** LAES subsystem.

Figure 3.12: T-s diagrams of the 'low-temperature' adaptation of the combined cycle, shown during charge.

Another possibility would be to substitute the water tanks by ground-level water reservoirs surrounded by a non-permeable insulating layer. This would somehow resemble pumped-hydro, where two water reservoirs are needed, but where energy is stored as thermal exergy rather than gravitational potential. However, the reservoirs could be natural terrain depressions or simply excavated on flat ground, since no height difference is required. Furthermore, the volume required per unit of energy stored is much lower. As noted in chapter 1, the energy density of a pumped hydro facility with a height difference of 500 m is about $1.4\,\mathrm{kWh/m^3}$, while the thermal availability of water at 100 °C is about $12\,\mathrm{kWh/m^3}$. However, the energy density of the combined cycle is even larger than this because of the contribution of the liquid air tanks, as will be shown below.

This adaptation of the combined cycle is similar to the 'pre-cooling' adaptation (section 3.3.3) in the sense that the PTES subsystem is regenerated and the HEX that couples the two cycles operates over a narrower temperature range, such that some pre-cooling of the supercritical air is required. This time, however, the pre-cooling is not provided by a cold store but by the expansion of secondary air streams of the LAES subsystem itself, in a way that resembles (to some extent) the first part of the Claude liquefaction cycle. In contrast to the Claude cycle, however, the returning streams are not at ambient pressure but at a higher intermediate pressure, such that the c_p variation of the main and the secondary streams is more similar and the impact of pinch-point issues is minimised.

The performance of the 'low-temperature' combined cycle depends on various factors, mainly:

- The fraction of air that is recirculated in the secondary streams, which is optimised to

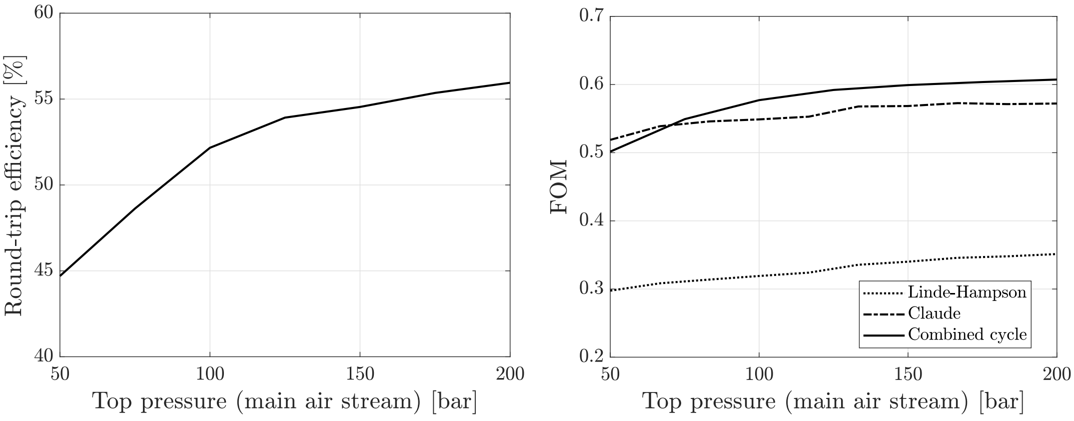

(a) Round-trip efficiency.

(b) Liquefaction efficiency.

Figure 3.13: Performance of the ‘low-temperature’ adaptation of the combined cycle.

ensure that $\dot{m}\overline{c_p}$ is the same at each side of the two air-air regenerators, similarly to the helium-air HEX.

- The pressure of the secondary streams, which is selected to be equal to the pressure of the incoming air prior to the last compression stage, where the returning streams rejoin the main stream. In this study the pressure ratio of the last compression stage is assumed to be the same as that of the other intercooled stages, but a future study should explore if there is scope for optimisation.

- The number of secondary air streams. Two secondary streams (with the corresponding air-air regenerators) are used here, cooling the main air stream down to $\sim 200\,\mathrm{K}$ before it enters the He-air coupler, but a third secondary stream could potentially be used. This would have the advantage of further cooling the main air stream and reducing the weight of the PTES subsystem, which is the least efficient.

- The top pressure of the main air stream, which also determines the number of inter-cooling stages. This is because the number of inter-cooling stages varies to ensure that the top temperature at each stage never exceeds the boiling point of water. The effect of the top pressure on the round-trip efficiency is shown in Fig. 3.13a. As expected, the efficiency increases with the top pressure, as it did in the previous adaptations of the combined cycle. Again, this is because the c_p variation of the supercritical air is less significant at high pressures, and because the LAES subsystem gains weight in front of the PTES subsystem.

A summary of important parameters of the ‘low-temperature’ adaptation, when operating at a top air pressure of $150\,\mathrm{bar}$, is shown in Table 3.8. Noticeably, the cycle is less efficient

Table 3.8: Main characteristics of the 'low-temperature' adaptation.

Parameter	Combined Cycle
Efficiency [%]	**54.5**
Energy density [kWh/m^3]	29.1
Work ratio (charge) [-]	3.2 (PTES)
	6.2 (LAES)
Water [t/MWh]	27.9
Liquid air [t/MWh]	5.7
Cost water [\$/kWh]	0.1
Cost water tanks [\$/kWh]	3.4
Cost air tanks [\$/kWh]	0.4
Total cost [\$/kWh]	**3.9**

than the previous adaptations, mainly because of the reduced work ratios of both subsystems, which is consequence of the larger number of intercooled stages and the expansion of the secondary streams in the LAES subsystem. On the other hand, the estimated cost of energy capacity is only $\sim 4\,\$/\mathrm{kWh}$, which is significantly lower than for all previous cycle adaptations. This cost is assuming carbon steel tanks (as for the stores in the previous cycle adaptations) for both the water and the liquid air tanks. However, the total cost is largely dominated by the cost of the water tanks, which, as discussed earlier, can potentially be cut down by employing low-cost non-metallic tanks or reservoirs.

While the cost of energy capacity is only $\sim 25\,\%$ of the cost of the previous cycle adaptations, the requirement of several inter-cooling stages is expected to increase the cost associated with power capacity, such that the system is likely to become competitive in those applications where long charge/discharge times are required or beneficial. This topic is briefly discussed in chapter 5.

Finally, another interesting feature of the charge-phase of the 'low-temperature' combined cycle is that it can be employed for liquid air production[7] (in which case the 'heat of compression' is not stored but simply rejected to the environment or used for other purposes). The plant may therefore be designed to supply the two different services, liquid air production and energy storage, thereby increasing its capacity factor and diversifying its

---

[7] Which can be used as an exergy carrier or, more often, to obtain nitrogen, oxygen, argon and other rare gases via partial distillation.

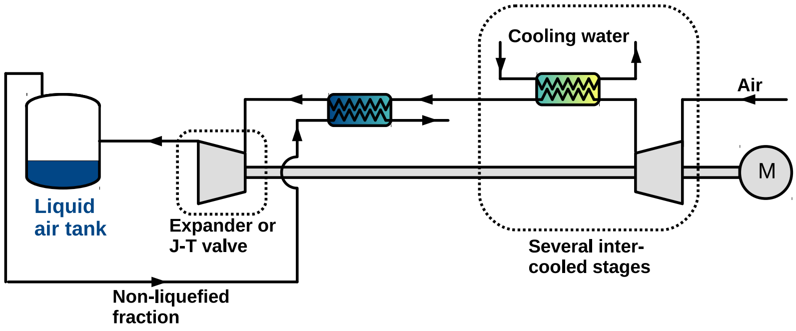

(a) Linde-Hampson cycle.

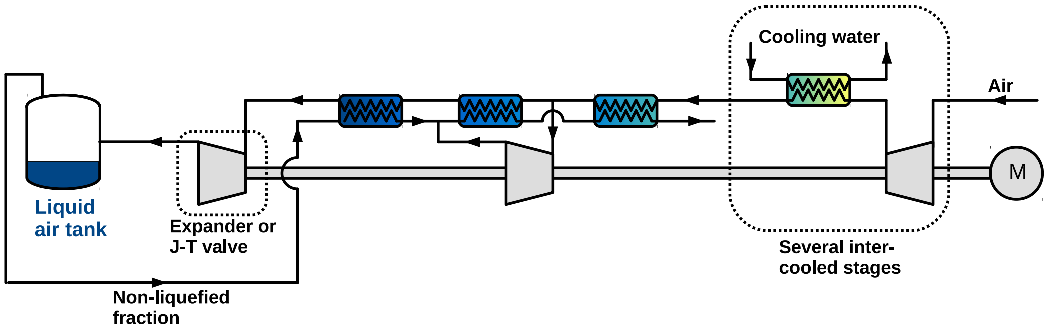

(b) Claude cycle.

Figure 3.14: Layouts of traditional liquefaction cycles.

streams of revenue.

The liquefaction efficiency is traditionally measured with the following figure of merit (FOM) [115],

$$\mathrm{FOM} \equiv \frac{w_{\mathrm{liq\,ideal}}}{w_{\mathrm{liq\,actual}}}$$

where $w_{\mathrm{liq\,ideal}}$ is equal to the specific exergy of liquid air (195 Wh/kg), and $w_{\mathrm{liq\,actual}}$ is the net work input of the cycle per unit mass of liquefied air. The FOM of the combined cycle is shown in Fig. 3.13b as a function of the top pressure of the main air stream. Note that the FOM is intrinsically lower than the charge exergetic efficiency because the exergy taken by the water streams is assumed to be rejected. For instance, at 150 bar, the charge exergetic efficiency of the combined cycle is 75 %, while the FOM is only 60 %. Interestingly, the FOM of the combined cycle exceeds that of the traditional Claude and Linde-Hampson liquefaction cycles for any top pressure above $\sim$ 75 bar. The layouts of these cycles are presented in Fig. 3.14, based on the descriptions by Windmeier and Barron [115]. While the original versions of the two cycles employ a Joule-Thomson (i.e. throttle) valve, the plots in Fig. 3.13b were computed using a two-phase mechanical expander. The FOM is significantly lower if a throttle is used, particularly in the case of the Linde-Hampson cycle.

Future work should include a comparison between the proposed combined cycle and the cycles used in modern air liquefaction plants, which are likely to be more advanced than the traditional Claude liquefaction system, which dates back to 1902 [115].

3.5 Concluding remarks

A novel thermo-mechanical energy storage system that integrates PTES and LAES into a single combined cycle has been presented in this chapter. The system employs liquid materials as thermal energy storage media and helium or neon as a working fluid for the PTES subsystem. Simple, design-level cycle calculations have been undertaken using realistically achievable values of compression and expansion efficiency and heat exchanger effectivenesses, from which the following may be concluded:

- The baseline combined cycle has a round-trip efficiency which is similar to stand-alone LAES but lower than stand-alone PTES ($\sim 60\,\%$ and $\sim 65\,\%$, respectively, for the nominal component performance parameters). This is only true, however, under the assumption that cryogenic expanders are practicable when operating with two-phase flow. If a throttle is employed instead, the efficiency of stand-alone LAES falls significantly below that of the other two cycles.

- A Second Law analysis reveals that the main losses in the baseline combined cycle are due to compression and expansion irreversibility and pinch-point-related losses in the main heat exchanger that links the two cycles. The pinch point arises from the strong variation of specific heat capacity of supercritical air at temperatures and pressures which are close to its critical point. This effect is reduced when operating the LAES subsystem at higher pressures, which has a positive impact on the efficiency of the overall cycle and also implies that lower pressure ratios are required from the PTES subsystem to produce liquid air at a given temperature.

- Although stand-alone PTES is found to be more efficient than stand-alone LAES, this trend is reversed when examining the constituent parts of the combined cycle: the PTES subsystem is significantly less efficient than the LAES subsystem. This is mainly because the operating conditions that the PTES cycle must adopt in order to be coupled with the LAES cycle are unfavourable and imply a low work ratio, and because the irreversibility generated in the heat exchanger that couples the two cycles is manifested only in the PTES subsystem. Ensuring full liquefaction of the air stream during charge, on the other hand, greatly improves the performance of the LAES subsystem.

- Three adaptations of the baseline combined cycle aimed at improving its performance have been proposed and studied. The first exploits asymmetric compression stages and is the easiest to implement. It is also compatible with the other adaptations. The second focuses on alleviating heat transfer irreversibility by employing a multi-stream heat exchanger with two levels of helium mass flow rate, thereby achieving a moderate increase in round-trip efficiency. The third adaptation, on the other hand, focuses on improving the performance of the PTES subsystem and reducing its weight within the combined cycle. This is done by employing a helium-helium regenerator on the PTES side and an additional thermal storage system to pre-cool the supercritical air before entering the helium-air heat exchanger. At the expense of a small reduction in overall energy density, this adaptation achieves a significant increase in thermodynamic efficiency, of about 10 percent points (from 60 % for the baseline combined cycle up to about 70 %), exceeding stand-alone PTES by 5 percent points.

- The energy density of all of the above-mentioned versions of the combined cycle ($60 \sim 80\,\mathrm{kWh/m^3}$) is significantly greater than either of the constituent subsystems (around $45\,\mathrm{kWh/m^3}$ for stand-alone PTES and $30\,\mathrm{kWh/m^3}$ for LAES). Despite the larger energy density, the estimated cost of energy capacity is not lower than for stand-alone PTES, since the combined cycle relies on mineral oil as a component of the hot store. If mineral oil could be substituted for a cheaper alternative, such as sunflower oil, the cost of storage capacity would be significantly lower.

- A further adaptation, referred to as 'low-temperature' adaptation, has been proposed with the aim to dramatically reduce the cost of energy capacity. This adaptation increases the number of inter-cooling compression stages and allows the hot stores to operate solely with water. The cycle has a lower round-trip efficiency of around 55 %, but could potentially enable much longer charge/discharge times than those of typical PTES/LAES systems. Since liquid air and water are the only storage materials and they have both a null or a negligible cost, the cost of the storage capacity becomes dominated by the cost of the storage tanks, and further savings could be achieved by substituting the water storage tanks by cheaper (low-temperature, non-metal-based) alternatives.

- Nominal operating conditions in all cycle adaptations assumed a pressure ratio of 150:1 for the LAES subsystem (which matches the expected pressures for commercial stand-alone LAES plants [64]), while the pressure ratio of the PTES subsystem was adapted in each case to ensure full air liquefaction. The latter is 135:1 for the baseline combined cycle and around 12:1 for the 'pre-cooling' and 'low-temperature' adaptations. Higher values of round-trip efficiency can be achieved by further increasing the pressure ratio of the LAES side and decreasing that of the PTES side.

- Repeating the calculations with neon instead of helium as a working fluid for the PTES subsystem leads to practically identical results as long as the same values of polytropic efficiency and heat exchanger effectiveness are assumed. Therefore, the choice between the two will fall down to economic considerations.

A summary of the predicted efficiencies, energy densities and estimated energy capacity costs of the different cycles studied in this chapter is presented in Figures 3.15a and 3.15b. The cost values are associated with the cost of the storage media and the tanks and are only approximate. Nevertheless, it is possible to state that the 'pre-cooling' adaptation stands as the most efficient cycle, while the 'low-temperature' adaptation achieves by far the lowest storage capacity cost. Different applications will favour one virtue over the other. It should be expected that the stand-alone PTES system, which has the least number of components (together with a mid-high efficiency and a moderate energy capacity cost), will have a relatively low cost of power capacity and might be preferred in some cases (see chapter 5 for a brief discussion on economic considerations).

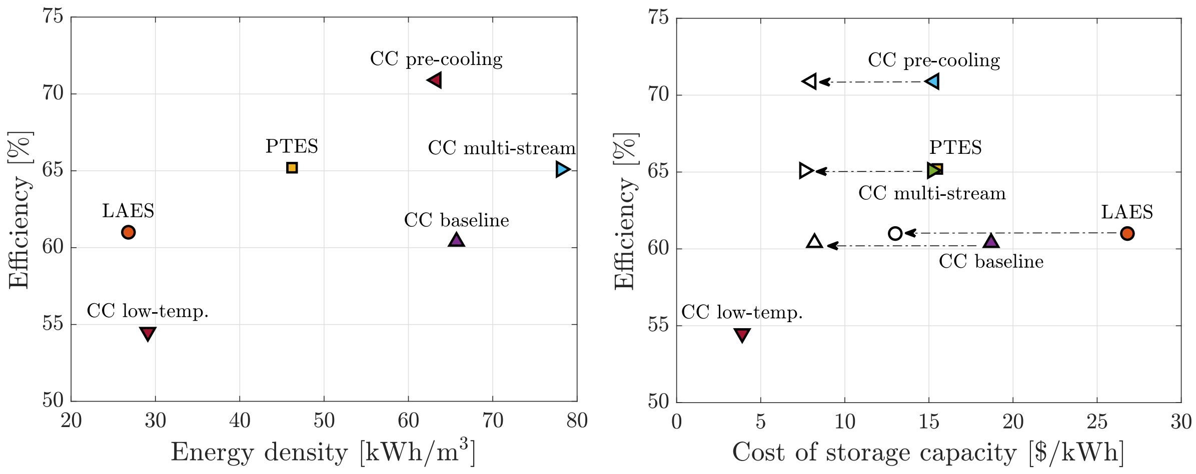

(a) Efficiency and energy density.

(b) Efficiency and cost of storage capacity.

Figure 3.15: Efficiency, energy density and cost of storage capacity of the studied cycles. In (b), filled markers indicate storage costs using the default storage media, while empty markers indicate cases where mineral oil has been substituted by a cheaper, vegetable oil alternative.

Chapter 4

Thermodynamic optimisation of heat exchangers

4.1 Introduction

Heat exchangers (HEXs) play a critical role in many thermodynamic cycles. In some applications, such as thermo-mechanical energy storage or cryogenic cycles [115], heat exchanger performance can significantly impact system performance and very high heat exchanger effectivenesses may be required. However, the required heat transfer area grows exponentially as the effectiveness increases, therefore increasing the amount of material needed and the size and cost of the device. Understanding how to design HEXs that are both highly efficient and compact is therefore an important consideration for such systems.

While a heat exchanger may be designed for specified effectiveness and pressure drop, a more exergetically meaningful approach employs entropy generation as a measure of performance. The idea of designing a heat exchanger for minimum irreversibility was first introduced by McClintock [116] in 1951, and later popularised by Bejan in 1977 [99], who has made significant contributions to the field of entropy generation minimisation (EGM) of flow and heat transfer processes through some of his various publications (e.g. [117–121]). Other early works of EGM applied to heat exchangers include those of Witte and Shamsundar [122], London and Shah [123] and Sekulić [124], in the early and mid 1980s.

Since then, several authors have continued to work on this field, as demonstrated by the high number of articles published so far (see e.g. the review in [125]). Some of the major topics explored so far include (i) the development of different performance indices to express entropy generation in a dimensionless form, (ii) the research of heat transfer surfaces that minimise entropy generation by increasing heat transfer and/or reducing flow friction, (iii) assessment of the entropy generation linked to the manufacturing process of the heat exchanger and (iv) thermo-economic analysis of heat exchangers. The reviews in [125] and [126] provide summaries of a significant part of the work done in the field.

Perhaps the biggest advantage of EGM is that entropy generation represents a single quantity that adds up the several sources of exergy loss in a consistent way. Thus, this avoids the need to separately specify, for example, a thermal performance and a hydraulic performance. In the case of heat exchangers, most authors have historically focused on flow thermal resistance and flow friction as the two main sources of irreversibility, while neglecting the contribution of axial (i.e. longitudinal) conduction. However, while this is generally a valid approach for long devices, compact heat exchangers tend to result in short channel lengths, in which case the effect of axial conduction on the thermal performance may overcome the effect of flow thermal resistance [93, 105].

Furthermore, as shown later in this chapter, when longitudinal conduction is neglected the EGM procedure delivers a physically unrealistic result, predicting a constant relationship between the volume of material and the hydraulic diameter, seemingly indicating that the HEX volume can be arbitrarily diminished by continuously decreasing the channel size (while maintaining a certain level of exergetic efficiency). There is, in fact, a general finding in the field of heat exchanger design that smaller channels lead to more compact devices (see [91, 96]). However, while the trend is certainly true when starting at high hydraulic diameters, the prediction neglects the fact that the channel's length dramatically decreases with decreasing diameter, which implies that axial conduction eventually becomes the dominant source of entropy generation.

A small subset of the literature on EGM of heat exchangers accounts for axial conduction. In 1983 Chowdhury and Sarangi found an analytical expression of the optimal metal conductivity for a concentric-tube exchanger of given diameter and length, minimising the overall exergy losses by balancing those due to axial conduction with those due to wall thermal resistance [127]. More recently, Will and de Waele provided expressions of entropy production for the different sources of irreversibility as a function of the geometrical parameters of an exchanger made with circular channels, and found a closed-form expression of the optimal diameter for pre-determined values of length and cross-sectional area when operating in the laminar regime [128]. Lerou et al. extended Will and de Waele's work by employing the same expressions and performing a numerical optimisation of the height, width and length of a two-channel HEX operating in a micro cooling cycle [129].

The analysis presented in this chapter focuses on minimising entropy generation in balanced gas-gas counter-flow heat exchangers for a given weight of construction material, which can be taken as a proxy for capital cost [44, 96, 130, 131]. After showing that small hydraulic diameters (and low Reynolds numbers) are a requirement for highly compact and efficient devices, laminar flow correlations are employed to obtain an analytical expression of the total entropy generation as a function of the basic geometrical parameters of the HEX, and closed-form solutions for the optimal channel length and hydraulic diameter are derived. For simplicity, the analysis is first presented for one single stream and then extended to the simultaneous optimisation of the two streams. Different gases and pressure levels are explored, indicating that both factors have a large impact on the cost-effectiveness of the device. Finally, a numerical optimisation method is employed to investigate situations with heat capacity variation. The model shows that heat capacity variation sets a minimum level of heat transfer irreversibility and affects the optimal geometrical configuration.

While all results presented in this chapter refer to the case of a gas-gas HEX, the analysis is readily adapted to the case of a gas-liquid HEX, as shown in Appendix B.

4.2 Basic design considerations

The field of heat exchanger design is vast and complex. Heat exchangers have been designed for a wide range of applications and a large number of geometries and manufacturing techniques have been developed. For an in-depth presentation of the major types of heat exchangers, one may refer to the book by Shah and Sekulić, *Fundamentals of Heat Exchanger Design* [91]. Herein the analysis is restricted to designs that consist of straight channels with constant cross-sectional area and no fins, but the methodology is readily adapted for other geometries. In this simplified case, the geometry of one side of the heat exchanger (i.e. the collection of channels corresponding to one fluid) has only three degrees of freedom [118]. For example: D, L and A_f (the hydraulic diameter, the length and the flow's cross-sectional area, respectively). Or, equivalently, D, L and $G \equiv \dot{m}/A_\mathrm{f}$, the mass flux. Once A_f and D are known, the total number of channels is fixed and one only needs to decide how to organise them (e.g. in the case of plate designs, how many channels per plate and how many plates), but this has little influence on the performance of the HEX core.

As mentioned before, it is generally found that employing smaller values of D allows a given thermal performance to be achieved with a more compact, less heavy (and typically cheaper) heat exchanger. The following shows that there are two main reasons for this: (i) smaller channels increase the amount of heat transfer area available per unit volume, and (ii) smaller channels permit higher heat transfer coefficients.

According to the definition of hydraulic diameter:

$$D \equiv \frac{4A_\mathrm{f}}{P} = \frac{4A_\mathrm{f}L}{A} = \frac{4V}{A} \tag{4.1}$$

Table 4.1: Formulas and coefficients for the fully developed internal flow model [97]. The equations for laminar flow are exact, analytical results. The equations for turbulent flow are experimental correlations valid for smooth surfaces. The values of the constants a_L and b_L refer to constant heat flux conditions. Transition from laminar to turbulent flow occurs between $2,000 \lesssim \mathrm{Re} \lesssim 3,000$.

	c_f	St
Laminar	$\dfrac{a_\mathrm{L}}{\mathrm{Re}}$	$\dfrac{b_\mathrm{L}}{\mathrm{RePr}}$
Turbulent	$\dfrac{1}{(1.58\ln\mathrm{Re}-3.28)^2}$	$\dfrac{(c_\mathrm{f}/2)(1-1000/\mathrm{Re})}{1+12.7(c_\mathrm{f}/2)^{1/2}\left(\mathrm{Pr}^{2/3}-1\right)}$

Constant	Circular pipe	Squared pipe
a_L	16	14.25
$b_\mathrm{L}(=\mathrm{Nu_L})$	4.36	3.61

where P is the channel perimeter, V the flow volume and A the surface (heat transfer area). The heat transfer area is related to the convective heat transfer coefficient h_t by

$$\dot{Q} = h_\mathrm{t} A \Delta T \tag{4.2}$$

where $\dot{Q}$ is the total heat transfer rate and ΔT is the temperature difference between the fluid and the channel's wall. Thus,

$$V = \frac{\dot{Q}D}{4h_\mathrm{t}\Delta T} \tag{4.3}$$

which emphasises the importance of increasing h_t to reduce the size of the HEX. In turn, h_t is related to the Stanton number:

$$\mathrm{St} \equiv \frac{\mathrm{Nu}}{\mathrm{RePr}} = \frac{h_\mathrm{t}}{Gc_p} \tag{4.4}$$

Well established correlations of St (or Nu) as function of the Reynolds and the Prandtl number, the channel geometry and the flow regime can be found in standard heat transfer textbooks (see [97]) and are shown in Table 4.1. One may, therefore, select a range of values of D and G, compute the corresponding Re and St numbers, and then compute the heat transfer coefficient h_t. The result is shown in Figure 4.1, which plots the value of h_t as a function of D for three different values of G for air in circular pipes. While some benefit can be obtained by jumping from laminar to turbulent regime at moderate values of D, it is clear

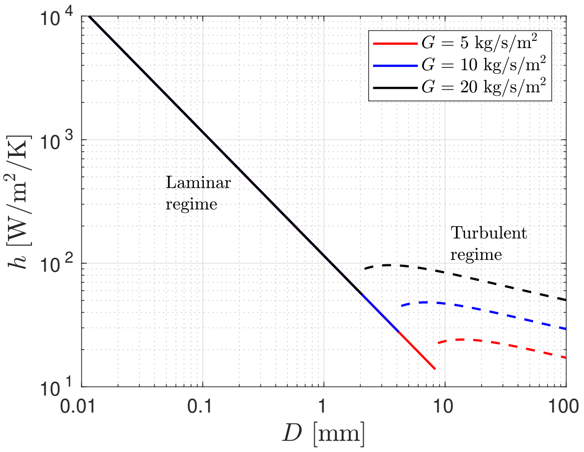

Figure 4.1: Convective heat transfer coefficient of air at ambient temperature for fully developed flow in a circular channel. Solid lines indicate laminar regime, dashed lines indicate turbulent regime.

that much higher heat transfer coefficients can be obtained by employing small channels (i.e. operating at low Reynolds numbers).

In the case of laminar flow, h_t simplifies to

$$h_t = \mathrm{St}Gc_p = \frac{b_\mathrm{L}Gc_p}{\mathrm{RePr}} = \frac{b_\mathrm{L}k}{D} \tag{4.5}$$

where k is the fluid thermal conductivity. Together with Eq. (4.3), this implies

$$V = \frac{\dot{Q}D^2}{4b_\mathrm{L}k\Delta T} \tag{4.6}$$

i.e. the flow volume becomes proportional to D^2 (and independent of G). It is shown later that the amount of material needed to fabricate a heat exchanger is proportional to the flow volume. Therefore Eq. (4.6) highlights the importance of employing small hydraulic diameters to reduce the HEX footprint and cost, specially for large-scale applications (high $\dot{Q}$) requiring high thermal performance (small ΔT). Interestingly, a very similar relationship between V and D has also been found in the context of more complex geometries operating in the turbulent regime [96].

In practice, the minimum possible value of D will be limited by the chosen manufacturing technique, and this explains the increasing interest in techniques for fabricating micro-channel heat exchangers, which can be built with several materials including silicon and a range of metals and alloys [95]. The building material also has an influence on the minimum diameter. For silicon, hydraulic diameters around 50 μm and wall thicknesses as thin as 15 μm [132] have been reported. For stainless steel and other base metal alloys, hydraulic diameters as small as $40\,\mu$m [93] have been reported, but wall thicknesses do not normally fall below $100\,\mu$m.

Diminishing the hydraulic diameter also has the effect of increasing flow friction, but this can be compensated by reducing L and increasing A_f (i.e. decreasing G) while maintaining the same overall heat transfer area. However, reducing L also has the effect of increasing axial conduction. As will be shown later, this makes an optimal D appear which balances the different losses and minimises the overall entropy generation.

4.3 Sources of entropy generation

Analytical expressions of entropy generation in heat exchangers due to flow thermal resistance, flow friction and axial conduction have been previously presented elsewhere (e.g. see the works by Will and De Waele [128] and Lerou et al. [129]). Nevertheless, the expressions are re-derived here for completeness and rewritten as a function of the volume of metal, which is useful for the subsequent analyses in the rest of the chapter.

4.3.1 Assumptions

The following assumptions are made when deriving the expressions of entropy generation:

- Counter-flow arrangement with balanced flows (i.e. $\dot{m}_1 c_{p1} = \dot{m}_2 c_{p2}$).
- Nearly ideal heat exchanger (i.e. $\Delta T \ll T$, $\Delta p \ll p$) with insulated (i.e. adiabatic) external walls.
- Straight, constant cross-sectional area channels with no fins.
- Ideal gas.
- Negligible kinetic or potential energy changes.

4.3.2 Flow thermal resistance and flow friction

Consider the simplified layout of a counter-flow HEX in Fig. 4.2a, and the diagram in Fig. 4.2c which shows the heat and mass flows on an infinitesimal section of one channel. The steady-flow energy equation reads simply,

$$\mathrm{d}\dot{Q} = \dot{m}\mathrm{d}h \tag{4.7}$$

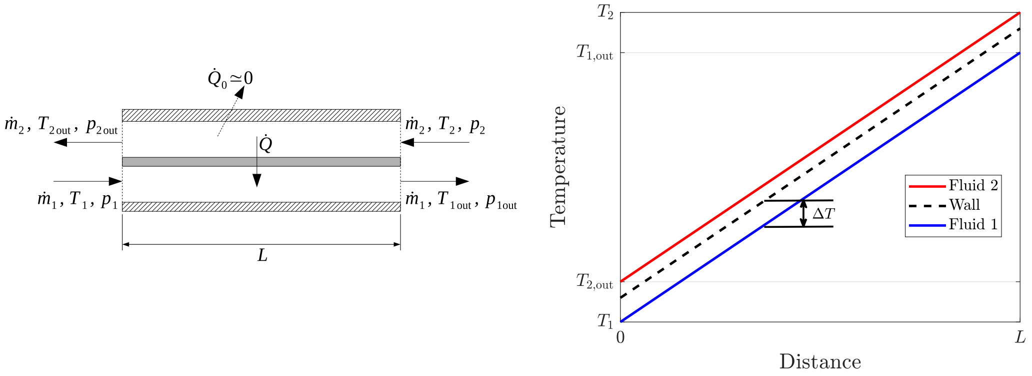

(a) One-dimensional diagram. **(b)** Temperature distribution.

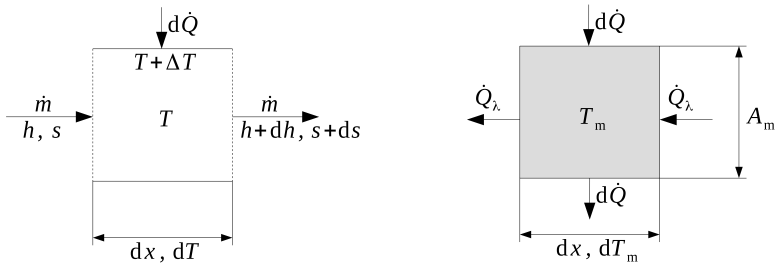

(c) Channel section. **(d)** Wall section.

Figure 4.2: Diagrams of a generic counter-flow heat exchanger.

while the steady-flow entropy equation reads,

$$\mathrm{d}\dot{S}_{\mathrm{irr}\,1} = \dot{m}\mathrm{d}s - \frac{\mathrm{d}\dot{Q}}{T+\Delta T} \tag{4.8}$$

where $\dot{S}_{\mathrm{irr}\,1}$ is the (irreversible) entropy generation per unit time in the stream 1 (and equivalent expressions follow for stream 2). The previous two equations, together with the thermodynamic relation

$$T\mathrm{d}s = \mathrm{d}h - v\,\mathrm{d}p \tag{4.9}$$

lead to

$$\mathrm{d}\dot{S}_{\mathrm{irr}\,1} = \mathrm{d}\dot{Q}\left(\frac{1}{T} - \frac{1}{T+\Delta T}\right) - \frac{\dot{m}v\,\mathrm{d}p}{T} \tag{4.10}$$

$$\simeq \frac{\mathrm{d}\dot{Q}\Delta T}{T^2} - \frac{\dot{m}v\,\mathrm{d}p}{T} \tag{4.11}$$

Employing the definition of St and Eq. (4.1), the specific heat transfer can be written

$$\mathrm{d}\dot{Q} = h_\mathrm{t}\Delta T\,\mathrm{d}A = \frac{4\mathrm{St}\dot{m}c_p\Delta T\,\mathrm{d}x}{D} \tag{4.12}$$

while the pressure change due to flow friction is [97],

$$\mathrm{dp} = -\frac{2c_\mathrm{f}vG^2\mathrm{d}x}{D} \tag{4.13}$$

leading to

$$\mathrm{d}\dot{S}_\mathrm{irr1} = \left(\frac{\Delta T}{T}\right)^2 \frac{4\mathrm{St}\dot{m}c_p\mathrm{d}x}{D} + \frac{2c_\mathrm{f}\dot{m}v^2G^2\mathrm{d}x}{TD} \tag{4.14}$$

From Fig. 4.2b one can see that ΔT is constant and that, on the limit $\Delta T \ll T$, temperature and length are related by

$$\mathrm{d}x = \frac{L\,\mathrm{d}T}{(T_2 - T_1)} \tag{4.15}$$

Additionally, from Eqs. (4.7) and (4.12),

$$\Delta T = \frac{D\,(T_2 - T_1)}{4L\mathrm{St}} \tag{4.16}$$

Including the previous expressions into Eq. (4.14), employing the ideal gas law and integrating from T_1 to T_2 (i.e. from 0 to L),

$$\dot{S}_\mathrm{irr1} = \frac{(T_2 - T_1)^2}{T_1T_2}\frac{\dot{m}c_pD}{4L\mathrm{St}} + \frac{2Rc_\mathrm{f}\dot{m}vG^2L}{pD} \tag{4.17}$$

where it is important to note that all variables which are temperature dependent (such as v, c_f or St) are taken as averaged values, evaluated at $p = p_\mathrm{in}$ and $T = 0.5(T_1 + T_2)$.

4.3.3 Wall axial conduction

The diagram in Fig. 4.2d shows the heat flows on an infinitesimal section of the wall separating the channels. The vertical arrows represent heat flows from one channel to the other, $\mathrm{d}\dot{Q}$, while the horizontal arrows represent axial conduction within the wall, $\dot{Q}_\lambda$. As shown in Appendix D, the thermal resistance of the wall is typically orders of magnitude smaller than the thermal resistance of the flow, and therefore its contribution to entropy generation can be neglected. Here the analysis is restricted to the contribution of axial conduction. The axial heat transfer is,

$$\dot{Q}_\lambda = A_\mathrm{m}k_\mathrm{m}\frac{\mathrm{d}T_\mathrm{m}}{\mathrm{d}x} \tag{4.18}$$

where A_m is the wall's cross-sectional area and k_m is the conductivity of the heat exchanger material. The associated entropy generation is:

$$\mathrm{d}\dot{S}_{\mathrm{irr,m}} = A_\mathrm{m} k_\mathrm{m} \frac{\mathrm{d}T_\mathrm{m}}{\mathrm{d}x} \left(\frac{1}{T_\mathrm{m} - \dfrac{\mathrm{d}T_\mathrm{m}}{2}} - \frac{1}{T_\mathrm{m} + \dfrac{\mathrm{d}T_\mathrm{m}}{2}} \right) \simeq A_\mathrm{m} k_\mathrm{m} \left(\frac{\mathrm{d}T}{\mathrm{d}x} \right)^2 \frac{\mathrm{d}x}{T^2} \tag{4.19}$$

Finally, substituting Eq. (4.15) into (4.19) and integrating leads to

$$\dot{S}_{\mathrm{irr,m}} = \frac{(T_2 - T_1)^2}{T_1 T_2} \left[\frac{A_\mathrm{m} k_\mathrm{m}}{L} \right] \tag{4.20}$$

4.3.4 Overall entropy generation

The entropy generation may be normalised by $\dot{m}c_p$ in order to obtain the dimensionless irreversibility function N_s, also known as the *number of entropy units*,

$$N_s \equiv \frac{\dot{S}_{\mathrm{irr}}}{\dot{m}c_p} \tag{4.21}$$

The N_s parameter is commonly used in the field of entropy generation minimisation, and it can be easily related to the exergetic loss as a fraction of the power of the cycle in which the heat exchanger operates [99]. For example, in the 'low-regen.' PTES cycle described in chapter 2, the charge cycle has $\left(\Delta T_{\mathrm{comp}} - \Delta T_{\mathrm{turbine}}\right) \approx 400\,\mathrm{K}$. Thus,

$$\frac{\dot{W}_{\mathrm{loss}}}{\dot{W}_{\mathrm{in}}} = \frac{T_0 \dot{S}_{\mathrm{irr}}}{\dot{m}c_p \left(\Delta T_{\mathrm{turbine}} - \Delta T_{\mathrm{comp}}\right)} \approx 0.75 N_s \tag{4.22}$$

i.e., for $N_s = 10^{-2}$ the exergetic loss is equivalent to about 0.75 % of $\dot{W}_{\mathrm{in}}$, the input power of the cycle.

Adding the contributions from the two streams (Eq. (4.17)) and from the wall (Eq. (4.20)), the irreversibility function of the HEX may be expressed as

$$N_s = N_{s1} + N_{s2} \tag{4.23}$$

where

$$N_{s1} = \underbrace{\frac{\tau^2}{4L}\left(\frac{D}{\mathrm{St}}\right)_1}_{\text{thermal resistance}} + \underbrace{2L\left(\frac{R}{c_p}\frac{c_\mathrm{f}\, v\, G^2}{pD}\right)_1}_{\text{flow friction}} + \underbrace{\frac{\tau^2 k_\mathrm{m}}{L}\left(\frac{A_*}{c_p G}\right)_1}_{\text{axial conduction}} \tag{4.24}$$

and an equivalent expression follows for N_{s2}. Note that the entropy generation in each stream contains the entropy generation due to the material associated with that stream (i.e., $A_{\mathrm{m}} = A_{\mathrm{m}1} + A_{\mathrm{m}2}$). The following definitions have been used:

$$\tau \equiv \frac{T_2 - T_1}{\sqrt{T_2 T_1}} \tag{4.25}$$

and

$$A_{*1} \equiv \frac{A_{\mathrm{m}1}}{A_{\mathrm{f}1}} = \frac{V_{\mathrm{m}1}}{V_{\mathrm{f}1}} \tag{4.26}$$

where A_* is a dimensionless parameter which depends on the kind of heat exchanger and is, in principle, independent of D, L and G (see Appendix C for more details). Since the aim is to minimise entropy generation for a given amount of construction material, it is useful to write N_s as a function of the volume of material. The volume of material in one stream is

$$V_{\mathrm{m}1} = A_{\mathrm{m}1} L = \left(\frac{A_* \dot{m}}{G} \right)_1 L \tag{4.27}$$

Substituting Eq. (4.27) and $D = \mathrm{Re}\mu / G$ into Eq. (4.24),

$$N_{s1} = \underbrace{\frac{\tau^2}{4} \left(\frac{\mu A_* \dot{m}}{V_{\mathrm{m}}} \frac{\mathrm{Re}}{\mathrm{St}} G^{-2} \right)_1}_{\text{thermal resistance}} + \underbrace{2 \left(\frac{R}{c_p} \frac{v V_{\mathrm{m}}}{p \mu A_* \dot{m}} \frac{c_{\mathrm{f}}}{\mathrm{Re}} G^4 \right)_1}_{\text{flow friction}} + \underbrace{\tau^2 k_{\mathrm{m}} \left(\frac{A_*^2 \dot{m}}{c_p V_{\mathrm{m}}} G^{-2} \right)_1}_{\text{axial conduction}} \tag{4.28}$$

4.4 Optimisation of one stream

Since the geometries of the two streams of a heat exchanger are linked (e.g. a counter-flow HEX will always have $L_1 = L_2 \equiv L$), one should in principle always attempt to perform a simultaneous optimisation of both streams. Nevertheless, the independent optimisation of one single stream is still a useful exercise, for two main reasons. First, it is a valid strategy when it is clear that the stream which is being optimised is the one having the biggest contribution into the exergy losses (e.g. in the case of a gas-liquid HEX, or a gas-gas HEX with one stream at a significantly lower pressure than the other). Second, the algebra is simplified considerably, which allows to present the physical principles in a more clear way. This section shows how to minimise N_{s1} for a given $V_{\mathrm{m}1}$, while section 4.5 extends the analysis to N_s (including both N_{s1} and N_{s2}).

The expression of N_{s1} in Eq. (4.28) is similar to that found by Bejan [118] but with two differences: (i) it is expressed as a function of the volume of material instead of the flow volume, and, most importantly (ii) it includes the term corresponding to axial conduction. Bejan proceeds by finding the optimal G_1 (which minimises N_{s1}) for a given Reynolds number and a given volume. If axial conduction is neglected,

$$\frac{\partial N_{s1}}{\partial G} = 0 \Rightarrow G_{1,\mathrm{opt}} = \left[\frac{\tau^2}{16} \frac{c_p}{R} \frac{\mathrm{Re}^2}{c_\mathrm{f}\mathrm{St}} \frac{p\mu^2 A_*^2}{v} \left(\frac{\dot{m}}{V_\mathrm{m}} \right)^2 \right]_1^{1/6} \tag{4.29}$$

and

$$N_{s1,\min} = \left[\frac{27\tau^4}{32} \frac{R}{c_p} \frac{c_\mathrm{f}\mathrm{Re}}{\mathrm{St}^2} \frac{v\mu A_*}{p} \frac{\dot{m}}{V_\mathrm{m}} \right]_1^{1/3} \tag{4.30}$$

from which one can learn that, for a given level of reversibility, less material is required at low Reynolds numbers. Consequently, the present analysis proceeds with a study of the laminar regime case, expanding Bejan's analysis by including the axial conduction term and including the dependence of St and c_f on Re from Table 4.1 into Equation (4.28). The number of entropy units becomes

$$N_{s1} = \underbrace{K_{\Delta T1} \frac{D_1^2}{V_{\mathrm{m}1}}}_{\text{thermal resistance}} + \underbrace{K_{\Delta p1} \frac{L^2}{V_{\mathrm{m}1} D_1^2}}_{\text{flow friction}} + \underbrace{K_{\lambda 1} \frac{V_{\mathrm{m}1}}{L^2}}_{\text{axial conduction}} \tag{4.31}$$

where the following parameters have been defined:

$$\begin{aligned} K_{\Delta T1} &\equiv \left(\frac{\tau^2 A_* \dot{m} c_p}{4 b_L k} \right)_1 \\ K_{\Delta p1} &\equiv \left(\frac{R}{c_p} \frac{2 a_\mathrm{L} A_* \mu \dot{m} v}{p} \right)_1 \\ K_{\lambda 1} &\equiv \left(\frac{\tau^2 k_\mathrm{m}}{\dot{m} c_p} \right)_1 \end{aligned} \tag{4.32}$$

Equation (4.31) is important because it brings further insight into the major trends that dominate the design of compact, highly efficient heat exchangers. For example, considering only the term due to thermal resistance gives $V_{\mathrm{m}1} \propto D_1^2$ for a given performance, which is the same conclusion reached with the simple analysis that led to Equation (4.6). On the other hand, considering thermal resistance and flow friction implies $N_{s1} \to 0$ when both $L \to 0$ and $D_1 \to 0$. In other words, it would appear that, *in the absence of axial conduction, a heat exchanger may be designed to be arbitrarily reversible and arbitrarily compact by making it infinitesimally flat and employing infinitesimally small channels*. This is, as mentioned before, a physically unrealistic result. However, when longitudinal heat transfer is introduced, N_{s1} cannot be made arbitrarily small any more and optimal values of both L and D_1 emerge.

For a given $V_{\mathrm{m}1}$ and a given L, the optimal D_1 is

$$\frac{\partial N_{s1}}{\partial D_1} = 0 \;\Rightarrow\; D_{1,\mathrm{opt}} = \left(\frac{K_{\Delta p} L^2}{K_{\Delta T}}\right)_1^{1/4} \tag{4.33}$$

while, for a given $V_{\mathrm{m}1}$ and a given D_1, the optimal L is

$$\frac{\partial N_{s1}}{\partial L} = 0 \;\Rightarrow\; L_{\mathrm{opt}} = \left(\frac{K_{\lambda} V_{\mathrm{m}}^2 D^2}{K_{\Delta p}}\right)_1^{1/4} \tag{4.34}$$

Solving the two above equations results in:

$$D_{1,\mathrm{opt}} = \left(\frac{K_{\lambda} K_{\Delta p} V_{\mathrm{m}}^2}{K_{\Delta T}^2}\right)_1^{1/6} \tag{4.35}$$

$$L_{\mathrm{opt}} = \left(\frac{K_{\lambda}^2 V_{\mathrm{m}}^4}{K_{\Delta T} K_{\Delta p}}\right)_1^{1/6} \tag{4.36}$$

and a minimum possible value of N_{s1}:

$$N_{s1,\mathrm{min}} = 3\left(\frac{K_{\Delta T} K_{\lambda} K_{\Delta p}}{V_{\mathrm{m}}}\right)_1^{1/3} = 3\left(\frac{a_{\mathrm{L}} \tau^4 A_*^2}{2} \frac{k_{\mathrm{m}}}{b_L k} \frac{R}{c_p} \frac{\mu v}{p} \frac{\dot{m}}{V_{\mathrm{m}}}\right)_1^{1/3} \tag{4.37}$$

where, noticeably, the exergetic losses corresponding to the three separate terms contribute equally to the overall loss (thus the factor 3 in front of the brackets).

At this point, the procedure to design an optimal stream becomes straightforward. First, Equation (4.37) is used to establish the required value of $V_{\mathrm{m}1}$ for the desired level of exergetic performance, unless $V_{\mathrm{m}1}$ is known *a priori* from economic considerations. Then, Equations (4.36) and (4.35) are used to determine D_1 and L, and finally Eq. (4.27) is employed to obtain the value of G_1. Once these parameters have been found, the geometry is determined and the remaining unknown parameters simply follow.

The optimisation procedure has been applied to six different gases that could be potentially employed in a regenerated Joule-Brayton cycle (hydrogen, helium, nitrogen, oxygen, neon and argon), for different pressure levels and for a range of V_{m} values, under the conditions shown in Table 4.2. Results are presented in Figures 4.3 and 4.4. The properties of the gases were determined using the thermophysical property library CoolProp [80]. For the results to be independent of the scale of the application, V_{m} is divided by $\dot{W}$, the *electrical* power of the corresponding power cycle (see Eq. 4.22), thus providing an indication of cost per unit power. The values of maximum allowable stress (important to determine A_*, as

Table 4.2: Ranges of values employed to compute the exergetically optimised design of one HEX stream.

Parameter	Unit	Value
$V_{\mathrm{m}1}/\dot{W}$	m^3/MW	0.001~1
p	bar	1~200
T_1	K	200
T_2	K	290
σ_{max}	bar	1000
k_{m}	W/m/K	15
L_{min}	mm	200
$(t/D)_{\mathrm{min}}$	-	0.05

shown in Appendix C) and thermal conductivity of the material correspond roughly to those of stainless steel (but variations are observed between different alloys).

As shown in Table 4.2, a minimum length has been specified, which is important for two different practical considerations. First, it is done to limit the thermal stress in the axial direction, as thermal gradients are inversely proportional to the length. Second, it is done because counter-flow designs require a non-pure-counter-flow region near the inlets and outlets of the exchanger, where the ports that distribute the flow are located [98]. In order to keep this region small relative to the counter-flow core, the number of ports (and the headers' cost and complexity) increase with decreasing length. Thus, if a minimum length were not specified, a counter-flow design could become impractical. As a detailed examination of these issues is outside the scope of this work, a value of L_{min} has been selected according to some of the shortest counter-flow HEXs encountered in the literature (e.g. [133, 134]), although lower values might be possible. In order to account for this limit, L_{opt} is computed first from Eq. (4.36). If L_{opt} is found to be smaller than L_{min} for a given V_{m}, L_{min} is used instead. Then $D_{1,\mathrm{opt}}$ is computed from Eq. (4.33) and N_{s1} from Eq. (4.31).

Table 4.2 also specifies a minimum thickness-to-diameter ratio (refer to Appendix C and Figure C.1 to see why this is done and how t/D affects A_*). A minimum diameter was not specified because predicted values fall within those reported as feasible. If a certain application required bigger values of D_1 than those predicted by Eq. (4.33), this can be easily accounted by specifying $D_{1,\mathrm{min}}$ and computing L from Eq. (4.34) instead of Eq. (4.36).

The graphs in Fig. 4.3 show the variation of N_{s1} and of the main geometrical parameters

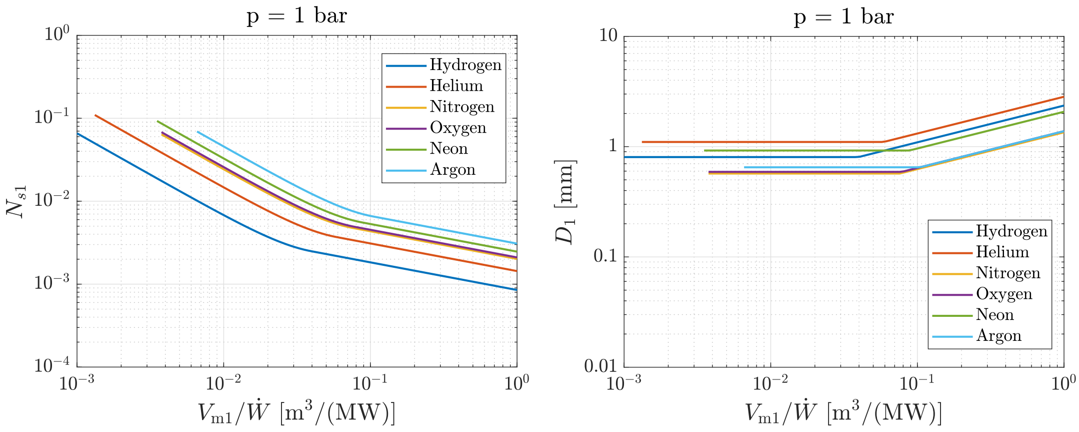

(a) Entropy generation function.

(b) Hydraulic diameter.

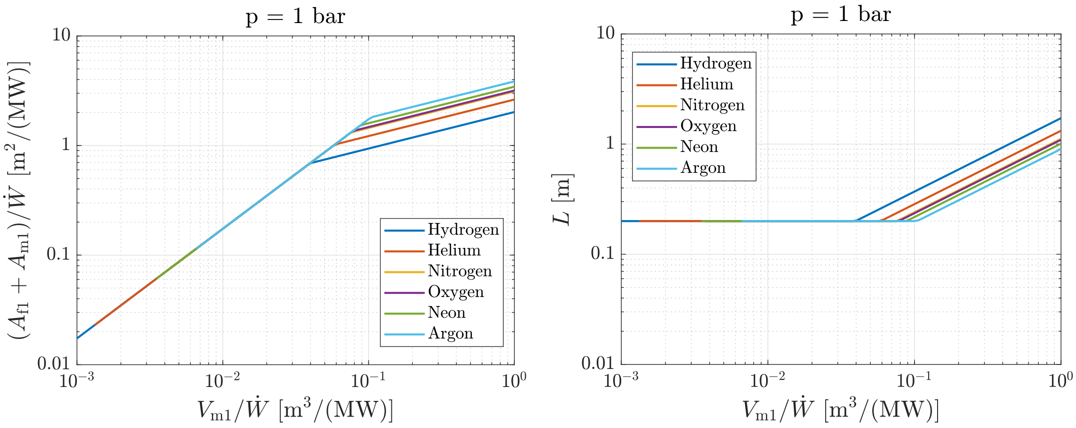

(c) Cross-sectional area.

(d) Length.

Figure 4.3: N_{s1} and main geometrical parameters as a function of $V_{m1}/\dot{W}$, for different gases at 1 bar and the conditions set in Table 4.2.

with $V_m/\dot{W}$, for a number of gases at 1 bar for the exergetically optimum design. In all cases one can identify two clearly separate regions, one where $L = L_{opt}$ and one where $L = L_{min}$. All the plotted points correspond to laminar flow. As shown in Fig. 4.3a, lower irreversibility is obtained from larger HEXs (i.e. that require more material). Furthermore, the graph indicates significant differences between different gases. To better understand this, Eq. (4.37) may be written as a function of $V_m/\dot{W}$, showing only those parameters that depend on gas properties:

$$N_{s1,\mathrm{min}} \propto \left(\frac{R}{c_p}\frac{\mathrm{Pr}\,\nu}{c_p^2}\frac{\dot{W}}{V_\mathrm{m}}\right)^{1/3} \propto \left(\left(\frac{R}{c_p}\right)^2\frac{\mathrm{Pr}}{c_p}\frac{\dot{W}}{V_\mathrm{m}}\right)^{1/3} \tag{4.38}$$

where the right hand side expression is obtained after employing the ideal gas law. One can conclude that a gas tends to be more advantageous if it has a higher c_p, or if it is a diatomic gas ($R/c_p \approx 0.29$) instead of a monatomic gas ($R/c_p \approx 0.4$). Table 4.3 provides the value of the factor $R\mathrm{Pr}\,v/c_p^3$, for the gases in Figure 4.3a, normalised with respect to the value for hydrogen. The parameter indicates how many times more material is required for a given level of reversibility, and evidences a significant advantage of hydrogen and helium over the other gases.

Table 4.3: Parameter $R\mathrm{Pr}v/c_p^3$ for different gases, normalised with respect to the value for hydrogen, at $p = 1\,\mathrm{bar}$ and $T = 300\,\mathrm{K}$.

Hydrogen	Helium	Nitrogen	Oxygen	Neon	Argon
1.0	5.1	14.1	15.6	26.0	51.0

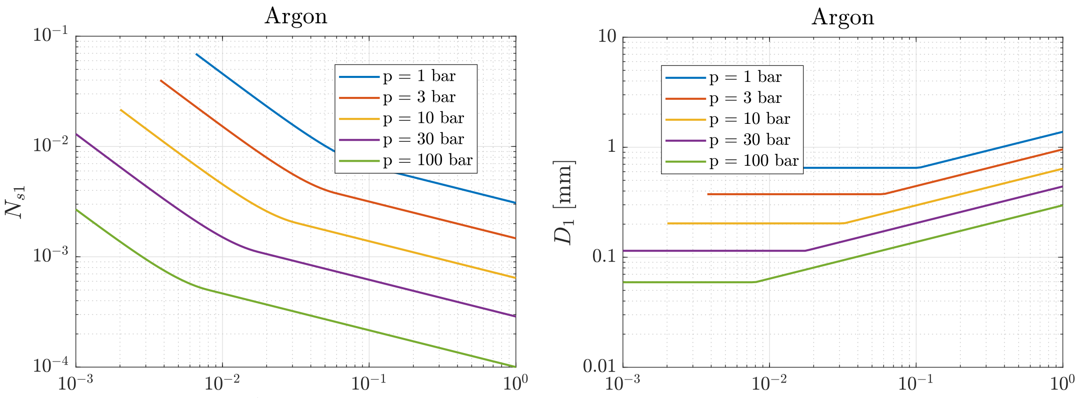

(a) Entropy generation function. **(b)** Hydraulic diameter.

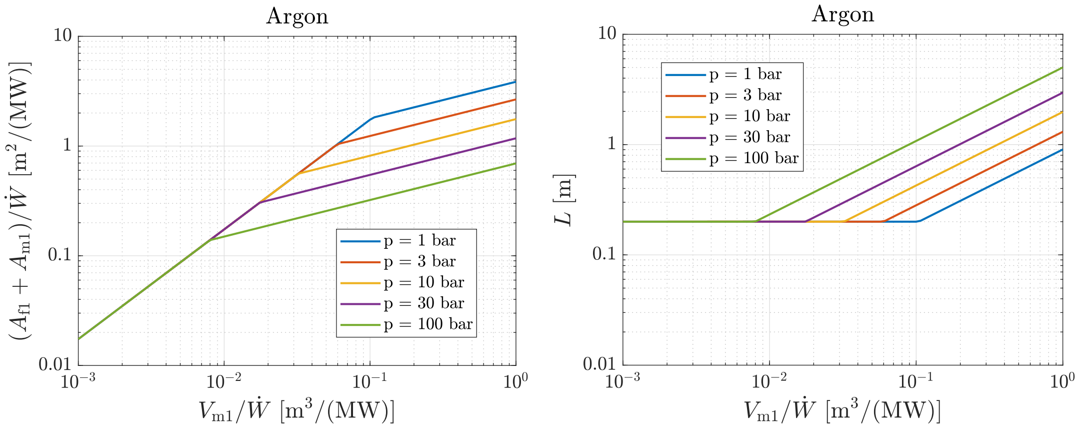

(c) Cross-sectional area. **(d)** Length.

Figure 4.4: N_{s1} and main geometrical parameters as a function of V_{m1}, employing Argon as working fluid at different pressures and the conditions set in Table 4.2.

Figure 4.4a shows N_{s1} as a function of $V_\mathrm{m}/\dot{W}$ for Argon at different pressures. For a given value of $V_\mathrm{m}/\dot{W}$ a significant reduction in N_{s1} is obtained at higher pressures. This improvement can be explained from Eq. (4.37), where the pressure-dependent parameters are proportional to $p^{-2/3}$ for an ideal gas. Other effects of pressurisation, as shown in Figures 4.4b, 4.4c and 4.4d are a decrease in the hydraulic diameter, a decrease in the cross-sectional area and an increase of the channel length. The last two effects are also regarded as beneficial for the construction and placement of the heat exchanger within a power plant, as they improve the aspect ratio of the device.

4.5 Simultaneous optimisation of the two streams

The simultaneous optimisation of the two streams is slightly more complex than the optimisation of a single stream, but follows the same principles and leads to very similar results. In order to find a globally optimum design, the entropy generation function must include the contributions from both streams:

$$\begin{aligned} N_s &= K_{\Delta T1}\frac{D_1^2}{V_{\mathrm{m}1}} + K_{\lambda 1}\frac{V_{\mathrm{m}1}}{L^2} + K_{\Delta p1}\frac{L^2}{V_{\mathrm{m}1}D_1^2} \\ &+ K_{\Delta T2}\frac{D_2^2}{V_{\mathrm{m}2}} + K_{\lambda 2}\frac{V_{\mathrm{m}2}}{L^2} + K_{\Delta p2}\frac{L^2}{V_{\mathrm{m}2}D_2^2} \end{aligned} \tag{4.39}$$

where one can identify five degrees of freedom: $V_{\mathrm{m}1}$, $V_{\mathrm{m}2}$, D_1, D_2, and L (one degree was already eliminated by noting that $L_1 = L_2 \equiv L$). Another degree of freedom can be eliminated by noting that the cross-sectional geometries are also linked. For instance, for a parallel-plate HEX, the two streams must have the same number of plates and the same plate width. Therefore, if the channels are straight, the combined width of all the channels of each stream (including the thickness of the walls between channels) must be the same. Referring to Fig. C.1 in Appendix C,

$$(D+2t)_1 N_1 = (D+2t)_2 N_2 \tag{4.40}$$

where the number of channels in one stream is

$$N_1 = \frac{4A_{\mathrm{f}1}}{\pi D_1^2} \tag{4.41}$$

Together with Eq. (4.27), the previous two expressions imply

$$D_2 = \frac{(1+2t/D)_2}{(1+2t/D)_1} \frac{A_{*1}}{A_{*2}} \frac{V_{\mathrm{m2}}}{V_{\mathrm{m1}}} D_1 \equiv K_* \frac{V_{\mathrm{m2}}}{V_{\mathrm{m1}}} D_1 \tag{4.42}$$

where the ratio t/D is assumed to be independent of D. Finally, defining the ratio $V_{\mathrm{R}} \equiv V_{\mathrm{m2}}/V_{\mathrm{m1}}$ and noting that $V_{\mathrm{m}} = V_{\mathrm{m1}} + V_{\mathrm{m2}}$,

$$V_{\mathrm{m1}} = \frac{V_{\mathrm{m}}}{1+V_{\mathrm{R}}} \tag{4.43}$$

and

$$V_{\mathrm{m2}} = \frac{V_{\mathrm{m}}}{1+1/V_{\mathrm{R}}} \tag{4.44}$$

Employing expressions (4.42), (4.43) and (4.44), the entropy generation function becomes

$$\begin{aligned} N_s &= K_{\Delta T1} \frac{(1+V_{\mathrm{R}}) D_1^2}{V_{\mathrm{m}}} + K_{\lambda 1} \frac{V_{\mathrm{m}}}{(1+V_{\mathrm{R}}) L^2} + K_{\Delta p1} \frac{(1+V_{\mathrm{R}}) L^2}{V_{\mathrm{m}} D_1^2} \\ &+ K_{\Delta T2} K_*^2 \frac{\left(V_{\mathrm{R}}^2 + V_{\mathrm{R}}\right) D_1^2}{V_{\mathrm{m}}} + K_{\lambda 2} \frac{V_{\mathrm{m}}}{(1+1/V_{\mathrm{R}}) L^2} + \frac{K_{\Delta p2}}{K_*^2} \frac{(1+1/V_{\mathrm{R}}) L^2}{V_{\mathrm{m}} V_{\mathrm{R}}^2 D_1^2} \end{aligned} \tag{4.45}$$

which now has four degrees of freedom: V_{m}, V_{R}, D_1 and L. Since the aim is to minimise N_s for a given V_{m}, the optimal values of D_1, L and V_{R} are searched for. As in the analysis for one single stream, the optimal values of D_1 and L can be found by setting $\partial N_s / \partial D_1 = 0$ and $\partial N_s / \partial L = 0$. The results are:

$$D_{1\mathrm{opt}} = \left[\frac{\left(K_*^2 V_{\mathrm{R}}^3 K_{\Delta p1} + K_{\Delta p2}\right) L^2}{K_*^2 V_{\mathrm{R}}^3 \left(K_{\Delta T1} + K_{\Delta T2} K_*^2 V_{\mathrm{R}}\right)} \right]^{1/4} \tag{4.46}$$

$$L_{\mathrm{opt}} = \left[\frac{K_*^2 V_{\mathrm{R}}^3 \left(K_{\lambda 1} + K_{\lambda 2} V_{\mathrm{R}}\right) V_{\mathrm{m}}^2 D_1^2}{(1+V_{\mathrm{R}})^2 \left(K_*^2 V_{\mathrm{R}}^3 K_{\Delta p1} + K_{\Delta p2}\right)} \right]^{1/4} \tag{4.47}$$

and, after solving the two above equations:

$$D_{1\mathrm{opt}} = \left[\frac{\left(K_{\lambda 1} + K_{\lambda 2} V_{\mathrm{R}}\right) \left(K_{\Delta p1} K_*^2 V_{\mathrm{R}}^3 + K_{\Delta p2}\right) V_{\mathrm{m}}^2}{(1+V_{\mathrm{R}})^2 K_*^2 V_{\mathrm{R}}^3 \left(K_{\Delta T1} + K_{\Delta T2} K_*^2 V_{\mathrm{R}}\right)^2} \right]^{1/6} \tag{4.48}$$

$$L_{\mathrm{opt}} = \left[\frac{K_*^2 V_{\mathrm{R}}^3 \left(K_{\lambda 1} + K_{\lambda 2} V_{\mathrm{R}}\right)^2 V_{\mathrm{m}}^4}{(1+V_{\mathrm{R}})^4 \left(K_*^2 V_{\mathrm{R}}^3 K_{\Delta p1} + K_{\Delta p2}\right) \left(K_{\Delta T1} + K_{\Delta T2} K_*^2 V_{\mathrm{R}}\right)} \right]^{1/6} \tag{4.49}$$

Although these expressions look fairly complicated, they strongly resemble the simpler Eqs. (4.35) and (4.36) and represent a sort of “weighted average” that results from optimising the combined two-stream system, allowing to obtain N_s as a function of V_m and V_R only. While it is not possible to obtain a closed-form analytical solution of $V_\mathrm{R,opt}$ (the optimal value of V_R for a given V_m), it can be found through straightforward single-variable numerical optimisation (e.g. through a golden-search method) in a small number of steps. Then, the design of the two streams becomes fully determined.

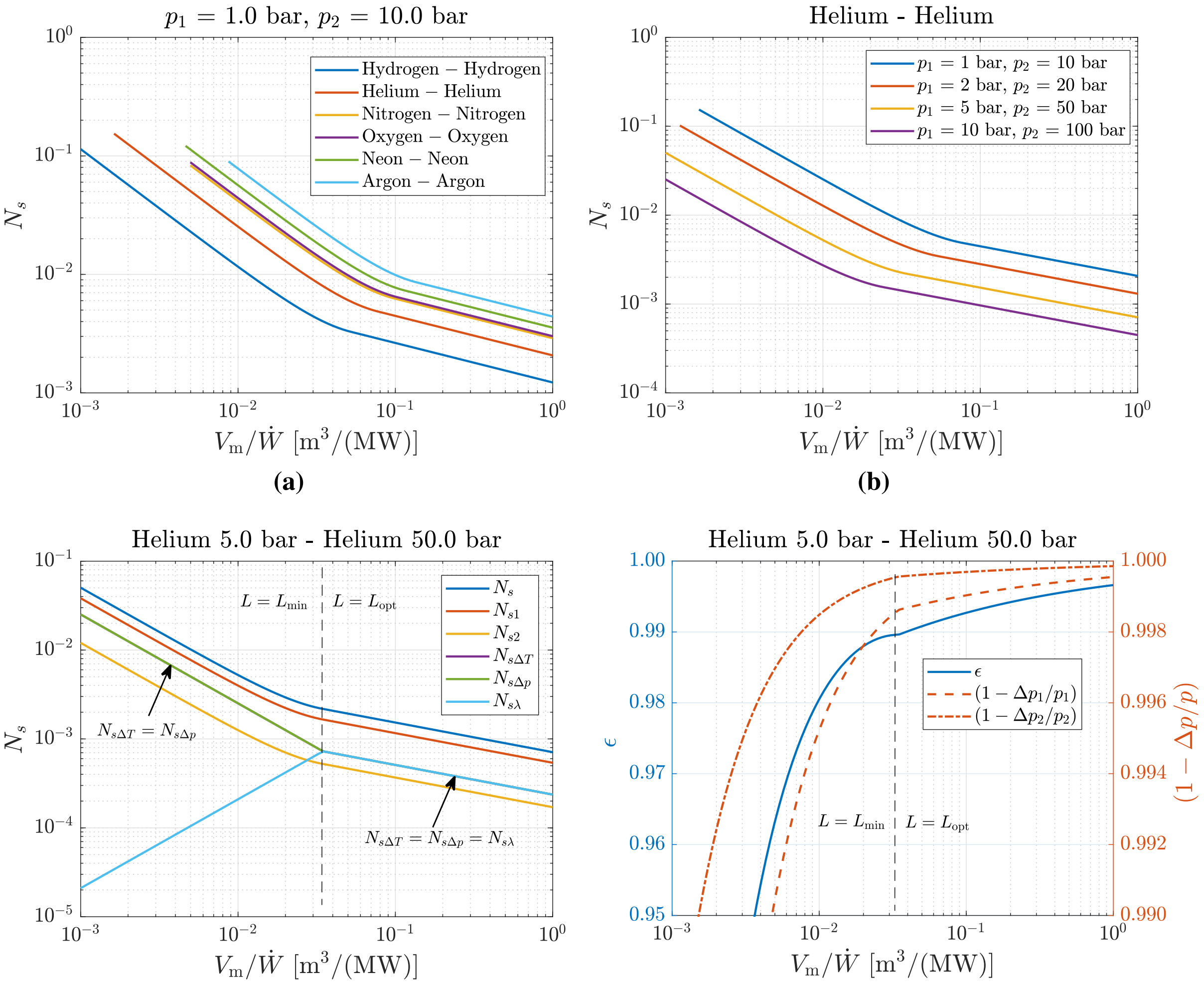

(a) (b)

(c) (d)

Figure 4.5: Selected results of the simultaneous optimisation procedure for two HEX streams. Above: N_s as a function of $V_\mathrm{m}/\dot{W}$ for (a) several gases (b) Helium at several baseline pressures. Below: (c) N_s distribution and (d) effectiveness and pressure drops for a helium regenerator with 5 bar and 50 bar streams.

This procedure has been applied to several gases and several pressure levels, and results are presented in the graphs in Fig. 4.5. Fig. 4.5a shows the dependence of N_s with $V_\mathrm{m}/\dot{W}$ for different gases, and Fig. 4.5b does it for helium at different baseline pressures. The pressure ratio between the two streams is 10:1 in all cases. No significant differences are observed between the trends shown in these plots and those obtained when optimising one single stream, although the absolute values do obviously vary. Figure 4.5c shows the distribution of N_s in its different components, in the case of a helium regenerator with 5 bar and 50 bar streams. Noticeably, N_{s1} (the low pressure stream) is much larger than N_{s2} (the high pressure stream). Furthermore, when $L = L_{\mathrm{opt}}$ the three components of entropy generation (adding the two streams) are exactly equal, while when $L = L_{\min}$ the loss due to axial conduction becomes much smaller than the other two.

It is also possible to show how the heat exchanger effectiveness and the pressure drop vary with $V_{\mathrm{m}}/\dot{W}$ for the optimised configuration. This has been done in Fig. 4.5d. The pressure drop was readily computed from Eq. (4.13), while the effectiveness was computed as follows. According to the traditional $\varepsilon\,(\mathrm{NTU})$ model for a balanced counter-flow heat exchanger without axial conduction (see Kays and London [103]),

$$\varepsilon = \frac{\mathrm{NTU}}{1+\mathrm{NTU}} \tag{4.50}$$

where

$$\frac{1}{\mathrm{NTU}} = \frac{1}{\mathrm{Ntu}_1} + \frac{1}{\mathrm{Ntu}_2} \tag{4.51}$$

where Ntu represents the ‘number of transfer units’ for each stream. For the first stream,

$$\mathrm{Ntu}_1 \equiv \frac{(h_{\mathrm{t}}A)_1}{(\dot{m}c_p)_{\min}} = \frac{4L\mathrm{St}_1}{D_1} \tag{4.52}$$

and similarly for the second stream. It can be shown that the contribution of axial conduction amounts to a reduction in effectiveness given by (again, from [103]):

$$\frac{\delta\varepsilon}{\varepsilon} \simeq \lambda_1 + \lambda_2 \tag{4.53}$$

where, for the first stream,

$$\lambda_1 \equiv \frac{k_{\mathrm{m}}A_{\mathrm{m}1}}{(\dot{m}c_p)_{\min}L} \tag{4.54}$$

and similarly for the second stream. It is straightforward to prove that, under the assumption of a high-performance HEX (see section 4.3.1), the previous expressions can be combined to read:

$$\varepsilon = 1 - \left(\frac{1}{\mathrm{Ntu}_1} + \lambda_1\right) - \left(\frac{1}{\mathrm{Ntu}_2} + \lambda_2\right) \tag{4.55}$$

which is the form that was used to produce the plots in Fig. 4.5d. The effectiveness can also be related to entropy generation via the following equation presented by Bejan [118]:

$$N_s = (1-\varepsilon)\,\tau^2 + \left(\frac{R}{c_p}\frac{\Delta p}{p}\right)_1 + \left(\frac{R}{c_p}\frac{\Delta p}{p}\right)_2 \tag{4.56}$$

Importantly, substitution of Eq. (4.55) into Eq. (4.56) leads to the same results as Eq. (4.24), which is the starting point of the optimisation study.

Finally, Table E.1 and Table E.2 (in Appendix E) present a summary of the inputs and outputs of the optimisation procedure for two regenerators, one employing helium and one employing argon, at a value of $V_\mathrm{m}/\dot{W}$ which corresponds to $\varepsilon = 99\,\%$ ($N_s = 2.09 \cdot 10^{-3}$) in both cases. Such high performances require metal volumes of $0.039 \cdot 10^{-2}\mathrm{m}^3/\mathrm{MW_{el}}$ (helium) and $0.328 \cdot 10^{-2}\mathrm{m}^3/\mathrm{MW_{el}}$ (argon), which, taking a density of $8000\,\mathrm{kg/m}^3$ as a reference for stainless steel, correspond to $312\,\mathrm{kg/MW_{el}}$ and $2624\,\mathrm{kg/MW_{el}}$, respectively. Obviously, significantly less material would be required at lower effectivenesses.

These optimised configurations, however, present a practical limitation in terms of the minimum wall thicknesses that seem to be currently manufacturable with stainless steel. For instance, the proposed argon regenerator has $D_1 = 0.5\,\mathrm{mm}$ and $D_2 = 0.15\,\mathrm{mm}$. While these hydraulic diameters are perfectly viable, the corresponding wall thicknesses[1] fall below the limits of current technology, which is $\sim 0.1\,\mathrm{mm}$ for micro-machining and $\sim 20-50\,\mu\mathrm{m}$ for additive manufacturing with metals [135]. Although additive manufacturing technology is advancing very rapidly (for instance, Vyatskikh et al. describe a novel lithography-based process to produce complex metal nano-structures with a resolution of $\sim 100\,\mathrm{nm}$ [135]), one must consider the mentioned limitation when designing configurations aimed at current commercial manufacturing technology. This issue is addressed in chapter 5, which explains how to adapt the optimisation procedure subject to a constraint of $t_\mathrm{min} = 0.1\,\mathrm{mm}$.

4.6 Fluids with varying heat capacity

The final section of this chapter is concerned with fluids that have non-negligible variation in c_p. It will be shown that this variation sets a minimum threshold to the entropy generation and affects the optimal design of the heat exchanger. In order to study such situations, a simple numerical method that computes the temperature profiles and the corresponding exergy loss for a given geometry was implemented.

The method starts by selecting an initial geometry (i.e. a set of values for V_m, V_R, L and

---

[1] Derived either from stress considerations or from the ratio $(t/D)_\mathrm{min}$, depending on the pressure level, as explained in Appendix C.

D_1, from which all the other parameters follow) and making an initial guess of the outlet temperature of the hot fluid, $T_{2\,\mathrm{out}}$, for the given inlet conditions. Then, the heat exchanger is divided in n 'temperature sections' (see Fig. 4.6 for reference) such that the hot fluid presents the same temperature variation in each section,

$$\mathrm{d}T_{2i} = \frac{T_2 - T_{2\,\mathrm{out}}}{n} \tag{4.57}$$

Next, the heat transfer and the temperature difference in each section of the cold stream are computed from

$$\mathrm{d}\dot{Q}_i = \dot{m}_2 c_{p2i} \mathrm{d}T_{2i} = \dot{m}_1 c_{p1i} \mathrm{d}T_{1i} \tag{4.58}$$

This approach allows a very quick determination of the $T\left(\dot{Q}\right)$ diagram of the heat exchanger (after integration of Eq. (4.58)) provided that $T_{2\,\mathrm{out}}$ is known, and has been used elsewhere to model the temperature distributions in heat exchangers with varying c_p and in multi-stream heat exchangers such as those encountered in liquid air energy storage systems (see e.g. [69]). In here, however, further steps are required in order to also determine $T\left(x\right)$ and compute the different sources of entropy generation. Since the initial geometry of the device is given, the Reynolds numbers are easily found and the heat transfer coefficients along each stream are computed from the expressions in Table 4.1. Then, the heat transfer area required at each section is found from

$$\mathrm{d}A_{1i} = \frac{\mathrm{d}\dot{Q}_i}{U_i \left(T_{2i} - T_{1i}\right)} \tag{4.59}$$

where the local stream-to-stream heat transfer coefficient (ignoring wall thermal resistance) is

$$\frac{1}{U_i} = \frac{1}{h_{\mathrm{t}1i}} + \frac{A_1}{h_{\mathrm{t}2i} A_2} \tag{4.60}$$

Once the array of $\mathrm{d}A_{1i}$ values has been calculated, they are added to compute the total heat transfer area, and this value is compared to the value of A_1 initially provided by the

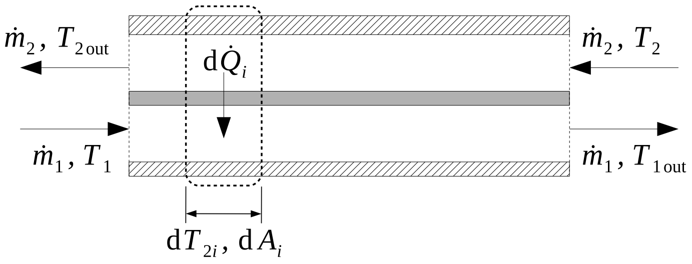

Figure 4.6: One-dimensional diagram of a heat exchanger, showing the i-th section.

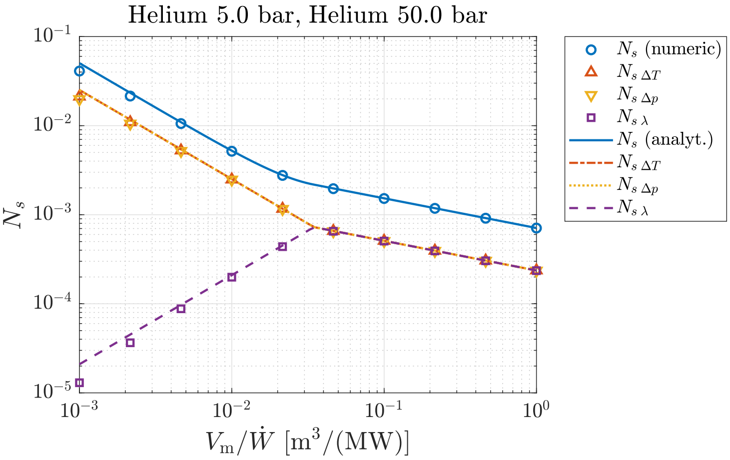

Figure 4.7: Comparison between the analytical procedure (solid lines) and the numerical optimisation method (symbols) for a helium regenerator.

given geometry. If the two values agree, it means that the initial guess of $T_{2\,\mathrm{out}}$ was correct. If the two values differ, the value of $T_{2\,\mathrm{out}}$ is changed and the procedure is repeated until convergence. Since $T_1 < T_{2\,\mathrm{out}} < T_2$, the converged solution is quickly reached through a simple golden search method.

Once the converged value of $T_{2\,\mathrm{out}}$ and the corresponding $T\left(\dot{Q}\right)$ and $T\left(x\right)$ diagrams are known (the $\mathrm{d}x_i$ array is found via $\mathrm{d}x_i = \mathrm{d}A_{1i}L/A_1$), the different sources of entropy generation can also be computed. The entropy generation due to irreversible heat transfer and flow friction are calculated by numerically integrating Eq. (4.14), while the component due to axial conduction is computed by numerically integrating Eq. (4.19). By doing so, the method assumes (as it was done during the previous sections of this work) that the effect of axial conduction is small enough to not significantly alter the shape of the $T\left(x\right)$ diagram.

The numerical procedure, therefore, may be coded as a function that computes N_s for given values of V_m, V_R, L and D_1 and given initial conditions. An optimisation algorithm can then be implemented to find the optimal values of V_R, L and D_1 that minimise N_s for a given V_m. This was done employing a constrained, non-linear, multi-variable optimisation algorithm, which is based on the interior point method [108] and is readily available in Matlab.

Figure 4.7 shows a comparison between the N_s value predicted by the analytical procedure and the one predicted by the numerical optimisation method for the helium regenerator of the previous section. The graph shows a strong agreement between the two methods, indicating that the c_p variation of helium is negligible and that this makes the analytical procedure a valid approach (agreement is found not only for N_s but for all the parameters of the optimised geometry). Nonetheless, a small deviation can be seen towards the low V_m

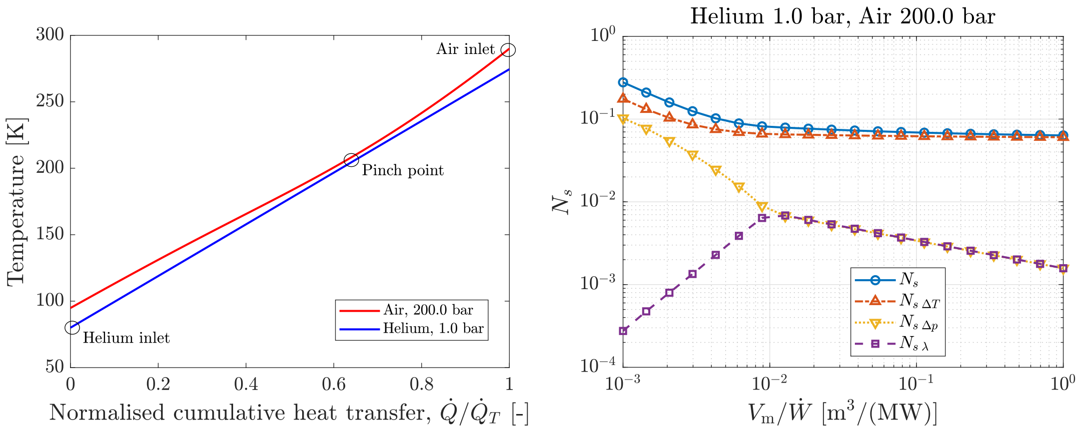

(a) Temperature distribution.

(b) Variation of exergetic losses.

Figure 4.8: Results obtained with the numerical method for a HEX operating with helium and supercritical air.

(high N_s) end of the graph. The deviation is an over-prediction of the losses by the analytical solution in that limit and is a consequence of the constant-gradient assumption made in Equation (4.15). In reality, as irreversibility increases and the effectiveness of the device decreases, the temperature gradient becomes less steep and this makes entropy generation more moderate, as captured by the numerical method.

The entropy function behaves differently in situations where c_p variation is non-negligible. Consider a HEX operating with helium and supercritical air (as the one included in the baseline PTES-LAES combined cycle from chapter 3). As shown in Fig. 4.8a, the HEX presents a pinch point where the temperature difference is minimum. In the limit of an infinitely large HEX, the pinch point temperature difference would be zero, but irreversible heat transfer would continue to occur elsewhere. As a consequence, $N_{s\Delta T}$ cannot be decreased below a certain minimum value. As shown in Fig. 4.8b, $N_{s\Delta T}$ and $N_{s\Delta p}$ have similar values in the low V_m (low effectiveness) region. However, at higher values of V_m the pinch point makes $N_{s\Delta T}$ reach a plateau, while $N_{s\Delta p}$ and $N_{s\lambda}$ continue to decrease as usual. Since N_s is the sum of the three separate contributions, it has the same minimum value as $N_{s\Delta T}$ and after some point there is no significant gain in further increasing V_m.

It is interesting to note that the highest variation in the c_p of supercritical air is encountered at conditions close to its critical temperature (132.5 K) and critical pressure (37.9 bar). As shown in Fig. 4.9a, the variation becomes less pronounced as the pressure is increased, and the pinch-point-derived losses becomes therefore less severe. As shown in Fig. 4.9b, this is translated in a lower minimum value for the overall entropy production. The optimal length and hydraulic diameter are shown in Figs. 4.9c and 4.9d. For purely illus-

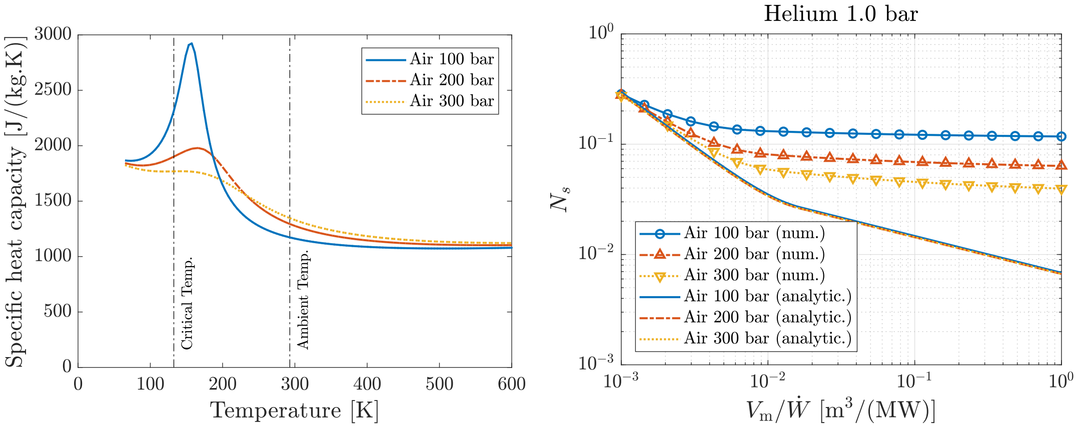

(a) c_p variation of supercritical air.

(b) Total entropy generation for the optimised designs.

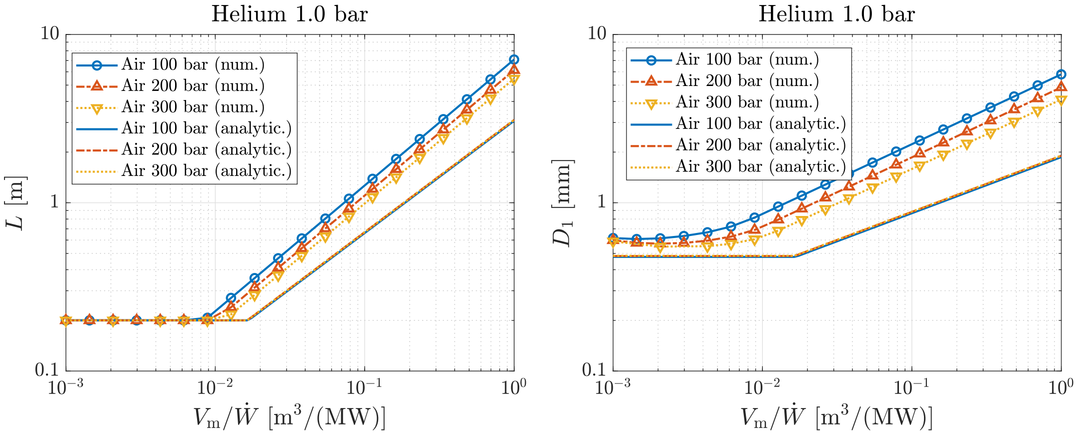

(c) Optimal lengths.

(d) Optimal hydraulic diameters.

Figure 4.9: Results of the numerical method for different pressures of the supercritical air and comparison with analytical results.

trative reasons, the results of the analytical method are included together with the numerical results. The analytical results correspond to a HEX operating with a fictitious fluid which has the same properties of supercritical air but constant c_p. In this case, higher air pressures do not have a noticeable impact because there is no pinch point and most of the entropy generation comes from the helium stream, which is at 1 bar in all cases. However, the numerical results show that the influence of pressure on c_p variation affects not only entropy generation but also the optimal geometry. Higher c_p variation is translated into both higher heat exchanger length and hydraulic diameters. Noticeably, this is consistent with what one may expect from Eq. (4.31) (or Eq. (4.39)) in a scenario with the same flow friction and axial conduction terms but a thermal resistance term with a weaker geometrical dependence, as is the case here.

4.7 Concluding remarks

In this chapter, an exergetic analysis of counter-flow heat exchangers has been presented, and analytical and numerical solutions of optimised geometries have been shown. Despite the limitations of any one-dimensional model, the study provides useful insight on the trends dominating exergy losses and optimal geometrical designs. The following points are worth being highlighted:

- The presented optimisation method treats the amount of heat exchanger material as the only fixed geometrical variable and entropy generation as the objective function to be minimised. Since the amount of heat exchanger material can be taken as a proxy for cost[2], the method identifies the geometric parameters that result in maximum efficiency at a given cost.

- Small hydraulic diameters are useful to obtain compact designs because: (i) smaller channels increase the amount of heat transfer area available per unit volume, and (ii) smaller channels permit higher heat transfer coefficients. In the case of laminar flow (as normally encountered at small values of D), the flow volume required for a given heat transfer rate and temperature difference is proportional to D^2 and independent of G (the mass flux).

- Introduction of axial conduction as a source of entropy generation eliminates the 'infinitesimal heat exchanger paradox': the notion that the size of a heat exchanger may be arbitrarily decreased by continuously decreasing the value of D without sacrificing performance. When axial conduction is accounted for (together with irreversible heat transfer and flow friction), optimal values of D and L can be found. The optimised geometries display a balanced distribution between the three sources of entropy generation.

- Depending on the inlet conditions and on the amount of heat exchanger material, the optimal length may be below the limit of practical heat exchanger designs. This can be accounted for by setting a minimum value of L, in which case an optimal value of D can still be found. In this case, the losses due to irreversible heat transfer and flow friction are still equal, but the loss due to axial conduction becomes smaller than the other two.

- The thermophysical properties of some fluids are beneficial in order to obtain more cost-effective designs. For example, a regenerator operating with helium requires

---

[2] See chapter 5 for more details on this topic.

about 10 times less heat exchanger material than an equivalent regenerator operating with argon. Operating at higher pressures also has a positive impact on the amount of material required.

- The analytical solutions are only valid in cases where the variation in specific heat capacity of the fluids is negligible. In cases where c_p varies significantly, a numerical method is required. Variation in c_p gives rise to pinch points that force irreversible heat transfer and set a minimum value for the overall entropy generation. This phenomenon also breaks the balance between the three sources of entropy generation, making irreversible heat transfer significantly larger than the other two in the optimised configuration.

- The analytical and numerical optimisation methods presented here rely on the assumption that the ratio between channel thickness and hydraulic diameter, t/D, is constant. This assumption, which is derived from stress considerations, produces optimised designs which have channel thicknesses below the limits of current manufacturing technologies employing stainless steel. Although this may very soon stop being true thanks to rapidly advancing additive manufacturing technologies, configurations aimed at current commercial processes should consider a minimum channel thickness as an additional constraint. This issue is addressed in the following chapter.

Chapter 5

Economic considerations

5.1 Introduction

As explained in chapter 1, the main focus of this project is the analysis and optimisation, from a thermodynamic perspective, of several PTES/LAES cycles and of the heat exchangers required by them. Little has been said so far about the economic performance of the different cycles, apart from estimating the cost associated with storage capacity in each case. However, since economics plays such a significant role in the success of storage technologies, it is important to also estimate the cost associated with power capacity. While a comprehensive and detailed economic analysis is beyond the scope of this work, the cost per unit power ($/kW) is computed here based on the cost of the turbomachines and the heat exchangers. This is then added to the cost of storage capacity ($/kWh) to obtain an indication of how the total capital cost varies with the nominal charge/discharge time.

The economic analysis is applied here to the three cycles that were found to be most promising from the studies in chapters 2 and 3, namely the 'high-regeneration' PTES cycle[1], the 'pre-cooling' combined cycle[2] and the 'low-temperature' combined cycle[3].

---

[1] Recall that this stand-alone PTES cycle uses an above-ambient regenerator, employs nitrogen as working fluid and stores the thermal energy in solar salt (hot side) and methanol (cold side). It achieves an efficiency of 65 % and has an estimated cost of storage capacity of 15 $/kWh. For more details, see Figures 2.10b and 2.11b and sections 2.4 and 2.6.

[2] Recall that this combined cycle uses a methanol cold store to pre-cool the supercritical air before entering the heat exchanger that links the LAES side with the PTES side. This allows the PTES side (driven by either helium or neon) to use a sub-ambient regenerator and have a lower overall pressure ratio. At the hot side of both subsystems, thermal energy is stored in solar salt and mineral oil. The combined cycle achieves an efficiency of 71 % and has an estimated cost of storage capacity of 15 $/kWh (or 8 $/kWh if mineral oil can be substituted by sunflower oil). For more details, see Fig. 3.10 and section 3.3.3.

[3] Recall that this cycle is similar to the 'pre-cooling' combined cycle but has more intercooled compression stages such that the hot stores can employ water as storage medium. It also substitutes the methanol cold store by expansion of secondary air streams that pre-cool the main supercritical air stream. The cycle achieves an

5.2 Cost of power capacity estimation

There is a number of different methods (varying in degrees of complexity and accuracy) to estimate the cost of the components of a process plant or power plant. For a quick and rough estimate, the engineer may use the so-called ‘rule of six tenths’, which relates the equipment cost (C) with its capacity or size (S) with a simple exponential function [136, 137]:

$$C_B = C_A \left(\frac{S_B}{S_A} \right)^n$$

where C_A and S_A are the known cost and size of a given piece of equipment, S_B is the size of the new equipment and C_B its cost estimate. The rule receives the name of ‘six tenths’ because, on average among several kinds of components in the process industry, $n \simeq 0.6$. The exact value of n, however, varies from one kind of component to another, as does the accuracy of the prediction. For instance, the rule may apply quite well to some pieces equipment such as pipes and tanks, but not so much to more complex components such as compressors and turbines, particularly when the operating conditions vary considerably from item A to item B. For this reason, more specific methods are used in sections 5.2.1 and 5.2.2 to estimate the capital cost of the turbomachines and the heat exchangers, respectively.

It is important to note that the cost estimates presented along this chapter correspond to those expected for a ‘mature plant’, i.e. once a large number of similar plants has been built and the development costs associated with the components of the plant have become negligible thanks to the benefits of mass production.

5.2.1 Turbomachinery

Accurately computing the cost of compressors and expanders is a challenging task, mainly a consequence of the complex nature of the design process of the turbomachines itself. It may be possible to obtain reliable data for the cost of a given compressor/expander (e.g. from a commercial gas turbine plant), but extrapolating this cost to a machine of a different power rating or a machine operating under different conditions (e.g. different inlet temperature and pressure, pressure ratio or working fluid) is not a straightforward process. Here, a very simple approach is used and the results should be regarded as approximate.

The cost model employed is based on a simplified version of the cost equations presented by Valero et al. [138] with recently updated fitting parameters in the context of gas turbines

---

efficiency of 55 % and has an estimated cost of storage capacity of 4 \$/kWh. For more details, see Figures 3.11 and 3.12 and section 3.4.

and CAES systems [20]:

$$Z_{\mathrm{c/e}} = \frac{C_{\mathrm{c/e}}\,\dot{m}\ln\beta}{\eta_{\mathrm{max}} - \eta} \tag{5.1}$$

where Z is the cost of the machine in USD and the c/e subscript indicates whether it is a compressor or an expander. η_{max} is set at 0.92 and the values of C_{c} and C_{e} are shown in Table 5.1. This cost equation is reasonable from a physical point of view: the cost increases linearly with $\dot{m}$ because the latter is proportional to the size and the power rating; the logarithmic increase with β accounts for the exponential relationship between pressure ratio and number of stages, and the asymptotic dependence with η accounts for the fact that there is a limit on the maximum possible efficiency of a turbomachine. According to the results presented in [20], this simple cost equation yields cost estimates which generally fall within ±30 % of reported values from actual gas turbines over a wide range of power ratings.

An obvious limitation of Eq. (5.1), however, is that it does not include any consideration on inlet temperature/pressure conditions or on the nature of the working fluid, because it is based on open-cycle gas turbines that operate with ambient air at the compressor inlet. A modification of the cost equation is therefore required to be able to apply it to the more diverse conditions of the cycles studied in chapters 2 and 3, which include pressurised configurations. Here, the modification is done based on an important fact noted by Laughlin [44], which is that (to a first approximation) the angle of the blades and the rotational speed of a turbomachine set the volumetric flow rate, and therefore increasing the inlet pressure essentially increases the power of the machine (because of the increased density and mass flow rate) without significantly affecting the cost. In other words, higher density means that a given power can be delivered with a more compact device. Consequently, Laughlin assumes an inversely proportional relation between cost per unit power and inlet pressure[4] and shows that, in a pressurised closed-cycle PTES system, the turbomachines become inexpensive enough for the cost to be dominated by the heat exchangers.

Following the previous reasoning, Eq. (5.1) is modified to provide a dependence on the volumetric flow rate rather than the mass flow rate:

$$Z^*_{\mathrm{c/e}} = Z_{\mathrm{c/e}}\frac{\rho_{\mathrm{ref}}}{\rho} = \frac{C^*_{\mathrm{c/e}}\dot{V}\ln\beta}{\eta_{\mathrm{max}} - \eta} \tag{5.2}$$

---

[4] It is obvious that this inversely proportional relation cannot be taken to the extreme without reaching absurd results (a compressor with an inlet pressure of 1000 bar will not be 1000 times cheaper than a compressor with an inlet pressure of 1 bar), but it seems reasonable to assume that the trend will be approximately correct at low-mid pressure levels. In practice it should be expected that at least two conflicting trends will be affecting the cost, since a higher pressure will mean a more compact device but also a thicker containment vessel.

Component	Eq. (5.1)	Eq. (5.2)	
Compressor	$C_\mathrm{c} = 670\,\$/(\mathrm{kg/s})$	$\rho_\mathrm{ref} = 1.2\,\mathrm{kg/m^3}$	$C^*_\mathrm{c} = 800\,\$/\left(\mathrm{m^3/s}\right)$
Expander	$C_\mathrm{e} = 1100\,\$/(\mathrm{kg/s})$	$\rho_\mathrm{ref} = 0.50\,\mathrm{kg/m^3}$	$C^*_\mathrm{e} = 560\,\$/\left(\mathrm{m^3/s}\right)$

Table 5.1: Parameters used in the turbomachinery cost equations.

where $Z^*_{\mathrm{c/e}}$ is the modified cost function and $C^*_{\mathrm{c/e}} \equiv C_{\mathrm{c/e}}\rho_\mathrm{ref}$ (values shown in Table 5.1). Note that the density and the reference density, ρ and ρ_ref, are computed at the inlet in the case of a compressor and at the outlet in the case of an expander. Reference values correspond to conditions in a typical gas turbine: 1 bar and 15 °C for the compressor, and 1 bar and $\sim 450\,°\mathrm{C}$ for the turbine. The volumetric flow rate is obtained from $\dot{V} = \dot{m}/\rho$. Note that Eq. (5.2) yields the same results as Eq. (5.1) when $\rho = \rho_\mathrm{ref}$, but it allows the costs to be estimated over a wider range of operating conditions.

Assuming ideal gas behaviour, it is possible to rewrite Eq. (5.2) in the form

$$Z^*_{\mathrm{c/e}} = \frac{C^*_{\mathrm{c/e}} \ln \beta^{(\gamma-1)/\gamma}}{\eta_\mathrm{max} - \eta} \frac{\dot{W}}{\Delta T} \frac{T}{p} \tag{5.3}$$

where $\dot{W}$ is the shaft power and ΔT the temperature difference between inlet and outlet, while T and p refer to inlet conditions for a compressor, and outlet conditions for an expander. Furthermore, because $\beta^{(\gamma-1)/\gamma} \approx \tau$ (the isentropic temperature ratio, see Eq. (2.2)), this equation suggests that the cost per unit power should be independent of the gas employed as long as the machine yields a certain *temperature* ratio (as opposed to a certain pressure ratio). However, one should be wary of extrapolating this conclusion to gases that are very dissimilar. For instance, it is known that compressing light gases such as hydrogen or helium with turbomachines is difficult and expensive because many stages are required [115]. The number of stages can be written as [139, 140]:

$$N_\mathrm{stages} = \frac{\Delta h_\mathrm{total}}{\Delta h_\mathrm{stage}} = \frac{c_p \Delta T_\mathrm{total}}{\psi U^2}$$

where ψ is the stage loading coefficient and U is the rotor blade speed. For given values of ψ and U, the number of stages becomes proportional to c_p, which suggests that a helium compressor (or expander) would require 5 times as many stages as an air compressor to achieve a certain temperature ratio (since $c_{p,\mathrm{He}} \simeq 5200\,\mathrm{J/kg/K}$, while $c_{p,\mathrm{air}} \simeq 1000\,\mathrm{J/kg/K}$). In air turbomachines, U values are limited both by stress considerations and by the speed of sound of the gas, since the losses increase significantly when the Mach number approaches unity [140]. On the other hand, helium has a speed of sound about three times higher than air[5], meaning that losses associated with Mach number effects basically disappear [141]. This generally allows blade speeds higher than in air turbomachines. However, because of the limits on bending stress, the increase in U is not large enough to fully compensate for the c_p effect on the number of stages and practical helium gas turbines are still characterised by a large number of stages for a given temperature ratio [141].

Considering the above discussion, Eq. (5.2) is only applied here to turbomachines operating with air and neon, which have very similar heat capacities ($c_{p,\mathrm{Ne}} \simeq 1050\,\mathrm{J/kg/K}$). The cost of the combined cycle configurations is therefore computed assuming that the PTES subsystem operates with neon rather than helium. Note that this does not change any of the conclusions presented in chapter 3, since, as already mentioned, performance calculations repeated for neon lead to essentially identical results. However, since neon does not have as good heat transfer properties as helium, larger heat exchangers are required.

5.2.2 Heat exchangers

The cost of the heat exchangers can be estimated with the analytical optimisation procedure presented in chapter 4. Note that the analytical model is used here (rather than the more computationally-expensive numerical model of section 4.6) because, for the three selected cycles, the effect of c_p variation is relatively small[6] thanks to the division of some cooling/heating processes in two or three different HEXs —but this would not be applicable to the baseline combined cycle, which employs a single HEX to cool down the supercritical air.

As previously discussed, one limitation of the optimisation procedure is that sometimes it leads to designs with channel walls which are too thin for current manufacturing techniques and thus to an underestimate of the cost. This issue is resolved here by introducing a minimum absolute thickness, t_{min}, as an additional constraint. The selected value is $t_{\mathrm{min}} = 0.1\,\mathrm{mm}$ for all streams except for the solar salt streams, in which case $t_{\mathrm{min}} = 0.5\,\mathrm{mm}$ is used to account for the effect of corrosion ($\sim 15\,\mu\mathrm{m/year}$ on stainless steel [85]).

The introduction of t_{min} does not change most of the trends discussed in chapter 4, but increases the metal volume (V_{m}) required to achieve a given performance. Furthermore, introducing t_{min} implies that an analytical closed-form solution for the optimal hydraulic diameter cannot be found, and the overall N_s function has to be minimised numerically in order to find the optimal values of D_1, L and V_{R} for a given V_{m}. Furthermore, since A_{*1}

---

[5] Speed of sound for an ideal gas $= \sqrt{(\gamma - 1)\, c_p T}$.

[6] It can be shown that neglecting the effect of c_p variation when estimating the cost of a HEX *for a given effectiveness* leads to an *overestimate* of the cost, because the expected average temperature difference is smaller and thus the expected heat transfer area is larger.

and A_{*2} become functions of D_1 and D_2, respectively, iteration is required to find the value of D_2 that corresponds to each pair of D_1 and V_{R} values (see Eq. (4.42)). On the other hand, finding a numerical solution means that the procedure is readily adapted to solve also for designs that may fall in the turbulent regime – in practice, this means using the entropy generation equation as presented in Eq. (4.24), which is general, rather than Eq. (4.39), which includes the assumption of laminar flow.

The adapted procedure is run for a range of V_{m} values to generate minimal entropy generation and effectiveness curves as a function of V_{m} – i.e. $N_s(V_{\mathrm{m}})$ and $\varepsilon(V_{\mathrm{m}})$ curves – for each heat exchanger. Since a certain level of effectiveness was specified[7] for the heat exchangers in chapters 2 and 3, the $\varepsilon(V_{\mathrm{m}})$ curves are used to find corresponding values of V_{m} for each heat exchanger. Once V_{m} is known, the cost of the heat exchanger is computed by:

$$Z_{\mathrm{HEX}} = C_{\mathrm{HEX}} \rho_{\mathrm{m}} V_{\mathrm{m}}$$

where $\rho_{\mathrm{m}} \simeq 8000\,\mathrm{kg/m^3}$ is the density of stainless steel, and C_{HEX} is the cost per unit mass of the heat exchanger. According to Kim et al. [130], who cite the company Heatric as source, the cost of printed-circuit heat exchangers correlates well with the mass of the device and is around $30\,\$/\mathrm{kg}$ for HEXs made of stainless steel. For comparison, Laughlin [44] estimates the cost of large shell-and-tube HEXs to be only $2\,\$/\mathrm{kg}$, which is twice the bulk cost of stainless steel. However, shell-and-tube exchangers require much larger hydraulic diameters than those achievable by printed-circuit exchangers, leading to V_{m} values more than one order of magnitude higher for a given performance. Gasketed flat-plate exchangers also have a lower cost per unit mass (a value of around $7.5\,\$/\mathrm{kg}$ can be derived from [142]) but cannot be used at high pressures. Finally, additive manufacturing technology, which allows more intricate designs but has (currently) a similar resolution than printed-circuit designs, has a material cost of about $80\,\$/\mathrm{kg}$ for stainless steel [143], which justifies the selection of printed-circuit exchangers.

5.2.3 Working fluid

The cost associated with purchasing the working fluid, which is associated with power capacity, was found to be negligible despite the PTES subsystems of the combined cycle relying on neon, which is a rare gas[8] with a high specific cost of around $80\,\$/\mathrm{kg}$. An indication of the amount of neon needed was obtained by computing the volume required to fill the

---

[7] $\varepsilon = 0.97$ under nominal conditions.

[8] Neon has a concentration of 18 ppm by volume in the atmosphere, and is obtained by fractional distillation of liquid air. A cost of $80\,\$/\mathrm{kg}$ was obtained from a quote by a Chinese manufacturer and is consistent with estimate prices that can be found online.

heat exchangers. Since the density of neon is low ($0.9\,\mathrm{kg/m^3}$ at ambient conditions), it only represents between $\sim 0.1-1\,\%$ of the density of stainless steel when pressurised to $10-100\,\mathrm{bar}$. When considering the specific dimensions of each heat exchanger, the cost associated with filling the neon stream was found to be less than 1 % of the total, and therefore it was deemed to be negligible.

5.2.4 Cost of power capacity for the 'high-regeneration' PTES cycle

In this section, the costs of the different turbomachines and heat exchangers of the 'high-regen.' PTES cycle are presented. The costs for the two other selected cycles (which have a larger number of components) will be presented in a more succinct way in the following section.

The costs and main parameters of the turbomachines are presented in Table 5.2, while the costs and main parameters of the heat exchangers are shown in Table 5.3. Interestingly, the total cost of the turbomachines happens to be very similar to the total cost of the heat exchangers for this cycle, at around $60\,\$/\mathrm{kW}$ (capital cost per net electric power output during discharge) for each block, leading to a total cost of power capacity of around $120\,\$/\mathrm{kW}$. This value is around 50 % of the value found by Laughlin [44] for a very similar PTES cycle, but in that case the cost is largely dominated by the heat exchangers, which are assumed to be of the shell-and-tube type and have a higher effectiveness.

Note that, despite the seemingly high fractional pressure losses predicted for the liquid streams in the gas-liquid heat exchangers (shown in Table 5.3), these losses correspond to a pumping load of around 2 kW for the solar salt and around 1 kW for the methanol, which are negligible compared to the $> 1\,\mathrm{MW}$ net power of the cycle. Furthermore, the pressure losses for the nitrogen streams at this level of effectiveness remain at around 0.5 %, meaning that the 1 % pressure loss per heat exchanger that was assumed for the cycle calculations in chapters 2 and 3 was an acceptable (if perhaps slightly conservative) estimate.

Table 5.2: Main parameters and cost estimates for the turbomachines of the PTES cycle. ρ refers to inlet conditions for the compressor, and outlet conditions for the expander.

	Turbomachines			
Component	Charge		Discharge	
	Compressor	Expander	Compressor	Expander
Fluid	Nitrogen			
T_{in} [K]	552	293	205	840
T_{out} [K]	860	197	357	556
p_{in} [bar]	24.4	105	24.2	132
p_{out} [bar]	106	24.7	134	24.4
ρ [kg/m^3]	14.8	44.6	41.6	14.6
$\dot{m}$ [kg/s]	10.0			
η [%]	90			
$\dot{W}$ [MW]	3.46	0.91	1.53	3.20
$Z^*_{\mathrm{c/e}}$ [10^3\$]	39.9	9.1	16.4	32.3
$Z^*_{\mathrm{c/e}}/\dot{W}$ [\$/kW]	11.5	10.0	10.7	10.1

Total $Z^*_{\mathrm{c/e}}$ [10^3\$]	97
$\dot{W}_{\mathrm{net,dis}}$ [MW]	1.67
Total $Z^*_{\mathrm{c/e}}/\dot{W}_{\mathrm{net,dis}}$ [\$/kW]	58

Table 5.3: Main parameters and cost estimates for the heat exchangers of the PTES cycle.

	Heat exchangers		
Component	Hot gas-liquid	Regenerator	Cold gas-liquid
Fluid 1	Solar salt	Nitrogen	Nitrogen
T_{in} [K]	550	293	197
p_{in} [bar]	1.0	24	24
$\dot{m}$ [kg/s]	7.2	10.0	10.0
Fluid 2	Nitrogen	Nitrogen	Methanol
T_{in} [K]	860	560	293
p_{in} [bar]	105	105	1.0
$\dot{m}$ [kg/s]	10.0	10.0	4.8
ε [%]		97	
$(\Delta p/p)_1$ [%]	560	0.66	0.45
$(\Delta p/p)_2$ [%]	0.45	0.38	125
V_{m} [m^3]	0.125	0.136	0.147
L [mm]	486	200	376
D_1 [mm]	0.16	0.17	0.22
D_2 [mm]	0.24	0.09	0.17
Re_1 [mm]	78	415	1140
Re_2 [mm]	1400	590	3.1
$(A_{\mathrm{f}} + A_{\mathrm{m}})$ [m^2]	0.31	0.92	0.60
$\dot{Q}$ [$\mathrm{MW_{th}}$]	3.46	2.84	1.06
Z_{HEX} [10^3\$]	29.9	32.6	35.3
$Z_{\mathrm{HEX}}/\dot{Q}$ [\$/$\mathrm{kW_{th}}$]	8.6	11.5	33.3

Total Z_{HEX} [10^3\$]		98	
Total $Z_{\mathrm{HEX}}/\dot{W}_{\mathrm{net,dis}}$ [\$/kW]		59	

5.3 Total cost and effect of storage capacity

A summary of costs for the three selected cycles is presented in Table 5.4. In terms of power capacity, the 'high-regeneration' PTES cycle was found to be the cheapest option, followed by the 'pre-cooling' and the 'low-temperature' adaptations of the PTES-LAES combined cycle. The turbomachines of the 'pre-cooling' and 'low-temp.' cycles were found to be significantly more expensive, mainly due to the fact that the LAES subsystem, which is an 'open-air' cycle, cannot be pressurised. On the other hand, the cost of the heat exchangers was found to be largely influenced by the heat-to-work ratio of each cycle, and under this metric the 'pre-cooling' system performs better than the stand-alone PTES cycle.

Table 5.4: Summary of costs for the three selected cycles, only including capital costs of the turbomachines, heat exchangers, storage media and tanks.

		PTES	CC 'pre-cooling'	CC
		'high-regen.'	mineral oil (veg. oil)	'low-temp.'
Turbomachines	$/kW	58	230	190
Heat exchangers	$/kW	59	24	150
Power capacity, total	**$/kW**	**120**	**250**	**340**
Storage media	$/kWh	11.0	12.7 (5.4)	0.1
Tanks	$/kWh	4.6	2.6	3.8
Energy capacity, total	**$/kWh**	**15**	**15 (8.0)**	**4.0**
Total (6 hours storage)	$/kW	200	340 (300)	370
Total (15 days storage)	$/kW	5700	5800 (3100)	1700

The table also shows the estimated costs of energy capacity as computed in the previous chapters, and shows examples of estimated total cost for two different applications, one with 6 hours of storage and another one with 15 days of storage. The variation of total cost with storage capacity is shown in more detail in Figure 5.1. This shows that the 'high-regen.' PTES cycle is likely to be preferred for applications where storage capacities of less than one day are considered sufficient, while the 'low-temp.' combined cycle is most likely to be preferred for applications with larger storage capacities. Note that a larger storage capacity means that the cycle is able to compensate for fluctuations in electricity production and demand over long time scales as well as deliver daily 'peak-shaving' services, thereby increasing the capacity factor of the plant. On the other hand, the competitiveness of the 'pre-cooling' cycle seems to hinge on whether sunflower oil (or another cheap vegetable

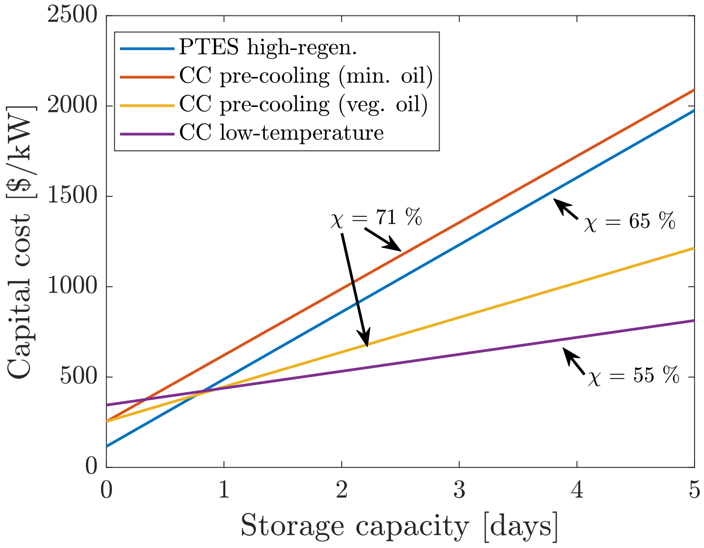

Figure 5.1: Variation of capital cost with storage capacity for three selected cycles. In the case of the 'pre-cooling' adaptation of the combined cycle, two different curves are shown, depending on whether mineral oil or sunflower oil are employed as storage media. The arrows indicate the round-trip efficiency of each system.

alternative) can be employed to substitute the expensive mineral oil in the hot stores. If this turns out to be possible, the cycle is likely to be preferred for applications with moderate storage capacities, specially in cases where a high efficiency is rewarded.

The costs shown in Table 5.4 and Fig. 5.1 are useful to compare the three selected cycles, but a comparison with other technologies should account for other costs not included so far, such as the electrical generator, controlling equipment and building infrastructure. The specific cost for a large electrical generator ($\sim$ 100 MW power plant) can be derived from the cost equations presented by Traverso et al. [144] for gas turbine power plants, indicating a cost of $\sim 40\,\$/\mathrm{kW}$. For all the other costs, such as site costs, ducting and electrical controlling equipment, Smallbone et al. [37] estimate a total value ranging between $200\,\$/\mathrm{kW}$ and $520\,\$/\mathrm{kW}$ ('technical potential' and 'conservative estimate', respectively) in the context of Joule-Brayton PTES cycles employing packed-bed reservoirs. The previous is consistent with the $350\,\$/\mathrm{kW}$ estimate indicated by Laughlin [44] to account for all costs other than the heat exchangers and the turbomachines, and this last value is used here.

Finally, Table 5.5 shows the updated costs of power capacity for the three studied cycles and compares them with those of pumped hydro and compressed air energy storage[9], which

---

[9] Batteries and other power-management technologies are not included in Table 5.5 because, as mentioned in chapter 1, despite their relatively low costs per unit power, their costs per unit energy capacity are much higher (normally above $100-200\,\$/\mathrm{kWh}$) and thus inadequate for large-scale energy management applications with several hours of storage.

are obtained from the review by Chen et al [1]. Although caution must be taken when using the costs shown due to the numerous approximations incurred when computing them, Table 5.5 indicates that the three studied cycles have costs per unit power and costs per unit energy that are comparable (and competitive) with those of PHS and CAES, while presenting the significant advantage of having no geographical constraints.

Table 5.5: Summary of main characteristics for the three selected cycles, compared with reference values for pumped hydro and compressed air energy storage (PHS and CAES data is from Ref. [1]). Costs of power capacity include a factor of 350 \$/kW that was added to the values from Table 5.4 to account for the electrical generator and all other infrastructure.[†]Value in brackets indicates case where mineral oil is substituted by vegetable oil as storage medium.

		PTES 'high-regen.'	CC 'pre-cooling'	CC 'low-temp.'	PHS	CAES
Efficiency	%	65	71	55	70-85	70-80
Energy Density	$\mathrm{kWh/m^3}$	46	63	29	0.5-1.5	3-6
Estimated cost (power capacity)	\$/kW	470	600	690	600-2000	400-800
Estimated cost (storage capacity)	\$/kWh	15	15 (8)[†]	4	5-100	2-50
Geographical independence		Yes	Yes	Yes	No	No

Chapter 6

Conclusions and future work

Growing amounts of renewable energy generation are being deployed worldwide in an effort to reduce greenhouse emissions and improve long-term energy security. While the fluctuating nature of wind and solar energy poses a challenge to the power network, it is now well established that large-scale storage can help to mitigate the effects of such fluctuations.

Pumped thermal energy storage (PTES) and liquid air energy storage (LAES) are two relatively new technologies that use mechanically-driven thermodynamic cycles to store electricity in the form of available thermal energy (i.e. exergy). The thermal energy is stored in large insulated tanks employing abundant materials. Both technologies are free from geographic constraints, which provides a significant advantage over competing methods such as pumped hydro energy storage or compressed air energy storage.

This thesis analyses, through analytical and numerical models, a Joule-Brayton version of PTES that employs liquid storage materials and heat exchangers. It also analyses several configurations of a combined PTES-LAES cycle and presents an optimisation procedure for the heat exchangers. Finally, economic estimates for the costs of power capacity and energy capacity of the most promising cycle configurations are computed.

6.1 Regenerative pumped thermal energy storage

Pumped thermal energy storage stores electricity in the form of available thermal energy. During charge, an electrically-driven heat pump is employed to transfer thermal energy from a cold reservoir to a hot reservoir. During discharge, a heat engine is operated between the same reservoirs in order to recover the energy stored. The ideal round-trip efficiency of PTES is 100 %, but in practice this is diminished by several loss mechanisms. Ongoing research is therefore focused on reducing such losses through optimisation of components, optimisation of the cycle operating conditions and development of new cycle configurations.

During the last decade, several PTES systems have been proposed. They can be broadly divided in three groups, depending on the thermodynamic cycle that they are based on: (i) Joule-Brayton cycles, (ii) Rankine cycles and (iii) transcritical cycles. The Rankine and transcritical cycles generally present a high work ratio, which reduces the impact of compression/expansion losses. On the other hand, the Rankine cycles require storage of latent heat, which prevents an independent sizing of the power and energy capacity of the storage units. The working fluid of the transcritical cycles tends to present strong variations in specific heat capacity, which also complicates the heat transfer process. The Joule-Brayton cycle has a worse work ratio but offers the advantage of storing all the energy as sensible heat and presenting very little variation in heat capacity.

The first Joule-Brayton PTES systems that were proposed use packed-bed reservoirs with direct heat exchanger between the working fluid and the solid particles. In chapter 2, a Joule-Brayton PTES system which employs liquid storage media is presented and studied. Using liquid storage media allows the system to simultaneously have unpressurised tanks and a pressurised working fluid, which reduces the cost of the storage tanks and the cost of the turbomachines. Furthermore, thermal fronts are removed from the storage units, which decreases self-discharge losses and simplifies operation.

An analytical study is presented that reveals how the performance of the cycle varies along a range of operating conditions. Generally, the same strategies that minimise compression/expansion losses also maximise heat exchanger losses, which results in optimal points at certain operating conditions. A numerical model based on design-level cycle analysis[1] is developed to find these optima while accounting for real fluid properties. On the other hand, constraints on the operating conditions arise from the limited temperature ranges of the candidate storage materials. The cycle can be adapted to these temperature ranges by either employing two liquids in series or by employing a regenerator, or both. Based on this, four possible cycle configurations are proposed. From these four configurations, a system that employs molten salt for the hot store, methanol for the cold store, nitrogen as a working fluid and a regenerator acting between ambient temperature and the hot store – referred to as the 'high-regeneration' configuration – is found to be the most promising. The regenerative process improves the work ratio of the cycle, which reaches a round-trip-efficiency of 65 % under nominal conditions.

---

[1] The model computes compression/expansion processes using a polytropic efficiency (η), and heat exchanger processes with a heat exchanger effectiveness (ε) and a fractional pressure loss ($\Delta p/p$). Nominal conditions assume $\eta = 0.9$, $\varepsilon = 0.97$ and $\Delta p/p = 0.01$; these values are ambitious but realistic for state-of-the-art devices. The model is written in Matlab and uses the library of thermophysical properties CoolProp.

6.2 Combined pumped thermal and liquid air cycles

Liquid air energy storage is a technology highly related to pumped thermal energy storage – it stores energy in the form of thermal exergy and is geographically unconstrained. The main difference between the two is that, while in PTES the working fluid flows in a closed circuit, LAES is an open cycle in which air is used both as working fluid and storage medium.

One of the appeals of LAES is its ostensibly high available energy density: the maximum work that can in principle be extracted from liquid air in returning it to ambient conditions is roughly $170\,\mathrm{kWh/m^3}$. However, a significant fraction of this exergy is consumed during discharge for the cold recycling process that powers the liquefaction cycle during charge. Additionally, the need for a cold reservoir further reduces the energy density.

In chapter 3, a combined cycle that integrates PTES and LAES is presented. The fundamental advantage of the hybrid cycle is that the PTES subsystem is used to provide the cooling duty required by the air liquefaction cycle, such that the cold thermal reservoirs that would be required by the separate cycles are replaced by a single heat exchanger that acts between them – thereby saving significant amounts of storage media per unit of energy stored. In order to reach cryogenic temperatures, the PTES cycle employs helium or neon as the working fluid, while the LAES cycle uses supercritical air (at around 150 bar) which is cooled sufficiently to be fully liquefied upon expansion, thus avoiding recirculation of leftover vapour. Both subsystems employ liquids (such as molten salt and thermal oil) as storage media for the hot stores, but alternative schemes using unpressurised packed-beds via a secondary heat transfer loop might also prove cost-effective.

The baseline configuration of the combined cycle is found to have a round-trip efficiency which is similar to stand-alone LAES but lower than stand-alone PTES ($\sim 61\,\%$ and $\sim 65\,\%$, respectively, under nominal conditions). On the other hand, it achieves a significantly higher energy density ($65\,\mathrm{kWh/m^3}$ compared to around $45\,\mathrm{kWh/m^3}$ for stand-alone PTES and $30\,\mathrm{kWh/m^3}$ for stand-alone LAES). A Second Law analysis reveals that the main losses in the baseline combined cycle are due to compression and expansion irreversibility and pinch-point-related losses in the main heat exchanger that links the two cycles. The pinch point arises from the strong variation in specific heat capacity of the supercritical air. This effect is reduced when operating the LAES subsystem at higher pressures, which has a positive impact on the overall efficiency.

Although stand-alone PTES is found to be more efficient than stand-alone LAES, this trend is reversed when examining the constituent parts of the combined cycle: the PTES subsystem is significantly less efficient than the LAES subsystem. This is mainly because the operating conditions that the PTES cycle must adopt in order to be coupled with the LAES cycle are unfavourable and imply a low work ratio, and because the irreversibility generated in the heat exchanger that couples the two cycles is manifested only in the PTES subsystem. Ensuring full liquefaction of the air stream during charge, on the other hand, greatly improves the performance of the LAES subsystem.

Based on the above considerations, different adaptations of the baseline combined cycle are proposed and optimised using a non-linear multi-variable optimisation algorithm. One adaptation focuses on alleviating heat transfer irreversibility by employing a multi-stream heat exchanger with two levels of helium (or neon) mass flow rate, thereby counter-acting the variation in heat capacity of the supercritical air and achieving a moderate increase in round-trip efficiency. Another adaptation focuses on improving the performance of the PTES subsystem and reducing its weight within the combined cycle. This is done by employing a regenerator on the PTES side and an additional thermal storage system to pre-cool the supercritical air before entering the heat exchanger that couples the two cycles. At the expense of a small reduction in overall energy density, this adaptation – referred to as the 'pre-cooling' adaptation – achieves a significant increase in efficiency, from 60 % for the baseline combined cycle up to 71 %.

A further adaptation, referred to as the 'low-temperature' adaptation, is proposed with the aim to dramatically reduce the cost of energy capacity. This adaptation increases the number of inter-cooling compression stages and allows the hot stores to operate solely with water. The cycle has a lower round-trip efficiency of around 55 %, but could potentially enable much longer charge/discharge times than those of typical PTES/LAES systems.

All the above results are found to be independent of whether helium or neon are used as working fluid for the PTES subsystem. However, the choice has implications regarding the cost of the heat exchangers and the compressors/expanders.

A summary of the predicted round-trip efficiencies, energy densities and costs of energy capacity[2] of the different cycles is shown in Figures 6.1a and 6.1b. The 'pre-cooling' adaptation stands as the most efficient cycle, while the 'low-temperature' adaptation achieves by far the lowest storage capacity cost. The stand-alone PTES system is also promising because of its simplicity and high power density (since it is a pressurised closed cycle), which leads to a lower cost of power capacity, as seen in chapter 5. It should be expected that different applications will favour some virtues over the others, meaning that the preferred cycle might change from case to case.

---

[2] Derived by adding the cost of the storage materials and the cost of the storage tanks.

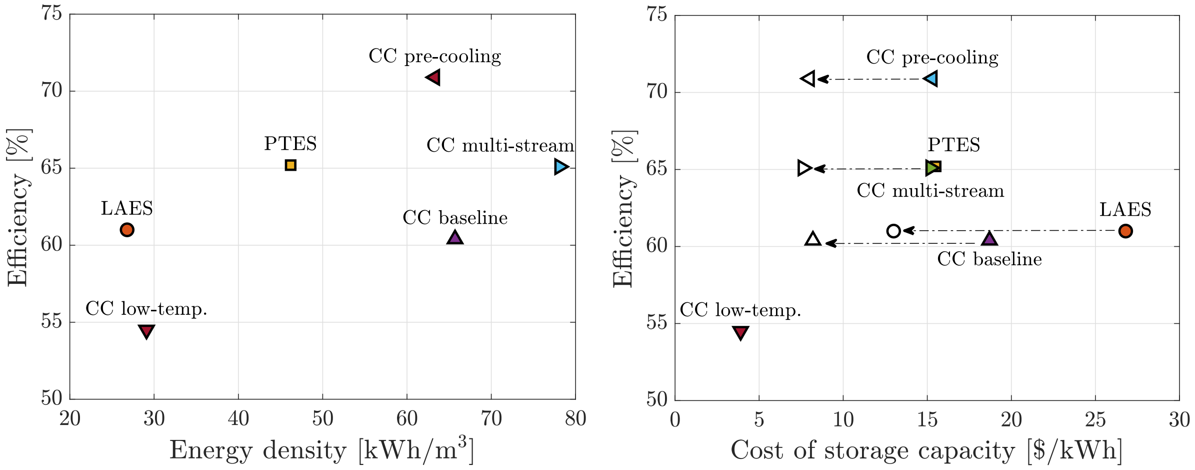

(a) Efficiency and energy density.

(b) Efficiency and cost of storage capacity.

Figure 6.1: Efficiency, energy density and cost of storage capacity of the studied cycles. In (b), filled markers indicate storage costs using the default storage media, while empty markers indicate cases where mineral oil has been substituted by a cheaper, vegetable oil alternative.

6.3 Optimisation of heat exchangers

The performance of the heat exchangers is found to have a significant impact on the overall performance of the studied cycles. Although heat exchangers can in principle be designed to arbitrarily high levels of effectiveness, high-performance heat exchangers tend to be large and expensive, as the heat transfer area grows exponentially with the effectiveness of the device. Understanding how to design heat exchangers that are both highly efficient and compact is therefore a very important consideration.

While a heat exchanger may be designed for specified effectiveness and pressure drop, a more exergetically meaningful approach employs entropy generation as a measure of performance. The process of optimising a certain thermodynamic process for minimum entropy generation is known as entropy generation minimisation (EGM). Perhaps the biggest advantage of EGM over other methods is that entropy generation represents a single quantity that adds up the several sources of exergy loss in a consistent way.

Most authors applying EGM methods on heat exchangers have historically focused on flow thermal resistance and flow friction as the two main sources of irreversibility, while neglecting the contribution of axial (i.e. longitudinal) conduction through the metal wall. However, while this is generally a valid approach for long devices, compact heat exchangers tend to result in short channel lengths, in which case the effect of axial conduction on the thermal performance can become significant enough as to overcome the effect of flow thermal resistance. A small subset of the literature on EGM of heat exchangers accounts for axial conduction, but in those works the authors tend to pre-specify a number of geometrical parameters (such as diameter and length, or length and cross-sectional area) which do not have a clear correlation with the cost of the device. In chapter 4, an optimisation procedure is presented with the aim to find optimised geometries that minimise entropy generation for a given amount of heat exchanger material – which is taken as a proxy for cost – as the only fixed geometrical variable.

The chapter starts by noticing that there are two reasons why small hydraulic diameters are useful to obtain a compact design: (i) smaller channels increase the amount of heat transfer area available per unit volume, and (ii) smaller channels permit higher heat transfer coefficients. In the case of laminar flow, this leads to the flow volume (as required for a given performance) being proportional to D^2 (the hydraulic diameter squared).

The chapter proceeds with an exergetic analysis of counter-flow heat exchangers, providing useful insight on the trends dominating exergy losses and optimal geometrical designs. For instance, the study finds that introducing axial conduction as a source of entropy generation eliminates the notion that the size of a heat exchanger may be arbitrarily decreased by continuously decreasing the value of D without sacrificing performance. When axial conduction is accounted for, optimal values of D and channel length (L) for a given amount of material (V_{m}) can be found. As expected, increasing the value of V_{m} decreases the overall entropy generation. Furthermore, the optimised geometries display a balanced distribution between the three sources of entropy generation – flow friction, parallel heat transfer resistance and axial conduction.

If the heat exchanger operates in the laminar regime, analytical solutions can be found for the optimal values of D and L. On the other hand, numerical solutions are required for heat exchangers operating in the turbulent regime and in situations where variation in specific heat capacity is significant. Variation in specific heat capacity boosts irreversible heat transfer and sets a minimum value for the overall entropy generation. This phenomenon also breaks the balance between the three sources of entropy generation, making irreversible heat transfer significantly larger than the other two.

One problem encountered by the optimisation procedure is that, depending on the inlet conditions and on the amount of heat exchanger material, the predicted optimal length may be below the limit of practical heat exchanger designs. This can be accounted for by setting a minimum value of L, which still allows to optimise the value of D in those cases. Another important consideration is the minimum thickness of the channel walls, t. The results presented in chapter 4 rely on the assumption that the ratio between channel thickness and hydraulic diameter, t/D, is constant, as can be derived from stress considerations. However, this assumption produces optimised designs which have channel thicknesses below the limits of current manufacturing technologies employing stainless steel. Although this may very soon stop being true thanks to rapidly advancing additive manufacturing technologies, configurations aimed at current commercial processes must consider a minimum channel thickness as an additional constraint. The method to adapt the optimisation procedure to account for this constraint is detailed in chapter 5.

Finally, the study in chapter 4 highlights that using different fluids can lead to very large differences in the cost of the device. For example, a regenerator operating with helium requires about 10 times less heat exchanger material than an equivalent regenerator operating with argon. Operating at higher pressures also has a very positive impact on the amount of material required.

6.4 Capital cost of the considered cycles

This thesis finishes with a rudimentary analysis on the capital cost of the most promising cycle configurations – the 'high-regeneration' PTES cycle[3], the 'pre-cooling' combined cycle[4] and the 'low-temperature' combined cycle[5]. Along chapters 2 and 3, the cost associated with the energy capacity of these different cycles (in \$/kWh) was derived by adding the cost of the storage materials and the cost of the storage tanks. In chapter 5, the cost associated with power capacity (\$/kW) is also estimated by adding the cost of the heat exchangers and the turbomachines.

A modified version of the optimisation procedure presented in chapter 4 (which accounts for a minimum thickness of the channel walls) is employed to compute the costs of the heat exchangers. The cost of the turbomachines is obtained from a simple cost equation developed in the context of open-cycle gas turbines, which is adapted here to account for the different operating conditions of the considered cycles. One of the features of the adapted equation is that the cost is proportional to the volumetric flow rate of the working fluid rather than to the mass flow rate (as was considered in the original equation). Because of this, the cost per unit power is predicted to decrease as the pressure increases. This is a reasonable prediction because a compressor/expander operating at high pressures (as in a pressurised closed cycle) has a higher power density and is more compact. On the other hand, the exact

---

[3] This stand-alone PTES cycle uses an above-ambient regenerator and stores the thermal energy in solar salt (hot side) and methanol (cold side). For more details, see sections 2.4 and 2.6.

[4] This version of the combined cycle uses a methanol cold store to pre-cool the supercritical air before entering the heat exchanger that links the LAES side with the PTES side. At the hot side of both subsystems, thermal energy is stored in solar salt and mineral (or vegetable) oil. For more details, see section 3.3.3.

[5] This version of the combined cycle has several intercooled compression stages such that the hot stores can employ water as storage medium. It also features secondary air streams that are expanded in order to pre-cool the main supercritical air stream (instead of a cold store). For more details, see section 3.4.

relationship between cost and pressure is uncertain and requires verification. The modified cost equation also predicts that turbomachines operating with different ideal gases should have a similar cost per unit power as long as they are designed for a given temperature ratio (as opposed to a given pressure ratio). This prediction is regarded as likely true for gases that have similar specific heat capacities, like air and neon, but is not applicable to very light gases like helium or hydrogen. This is because light gases have specific heat capacities much larger than that of air, which means that more stages of compression/expansion are required for a given temperature increase.

From the three cycle configurations considered in chapter 5, the 'high-regeneration' PTES cycle presents lower costs per unit power than the two combined cycle adaptations. The difference, however, becomes less significant once other 'fixed costs' – such as the cost for the electrical generator, control equipment and remaining infrastructure – are added to those of the heat exchangers and the turbomachines.

Because of their higher efficiency and the lower cost of power capacity, the 'high-regeneration' and 'pre-cooling' cycles are likely to be preferred in applications with storage capacities lower than one day. On the other hand, the very low cost of storage capacity of the 'low-temperature' adaptation potentially opens the door to schemes with much larger discharge times – up to several days or even weeks – than those typically considered for other PTES and LAES schemes.

Table 6.1: Summary of main characteristics for the three selected cycles, compared with reference values for pumped hydro and compressed air energy storage (PHS and CAES data is from Ref. [1]). †Value in brackets indicates case where mineral oil is substituted by vegetable oil as storage medium.

		PTES 'high-regen.'	CC 'pre-cooling'	CC 'low-temp.'	PHS	CAES
Efficiency	%	65	71	55	70-85	70-80
Energy Density	$\mathrm{kWh/m^3}$	46	63	29	0.5-1.5	3-6
Estimated cost (power capacity)	$/kW	470	600	690	600-2000	400-800
Estimated cost (storage capacity)	$/kWh	15	15 (8)†	4	5-100	2-50
Geographical independence		Yes	Yes	Yes	No	No

The main characteristics of the three selected cycles are shown in Table 6.1 and compared to reference values for pumped hydro and compressed air energy storage. While the round-trip efficiencies of the selected PTES and combined cycle configurations fall slightly behind those of PHS and CAES, results indicate that the selected cycles would be competitive with reported costs for PHS and CAES, while featuring geographical independence and much larger energy densities.

6.5 Recommendations for future work

As a result of what has been learned during this project, the following lines of research seem particularly promising:

- Experimental validation of sunflower oil (and other cheap vegetable oils) as an alternative to mineral oil for thermal energy storage at temperatures up to $200-250\,^{\circ}\mathrm{C}$. Special attention should be placed on the stability of the material under thermal cycling and under storage at high temperatures over prolonged periods of time, while surrounded either by air or by an inert atmosphere.

- Investigation of the viability of using isothermal compression/expansion stages for the 'low-temperature' PTES-LAES combined cycle, with the aim of improving the efficiency and the energy density and further reducing the cost per unit of energy capacity. Further theoretical and experimental development of the different methods for realising isothermal compression and expansion, with particular emphasis on practical considerations such as obtaining a high power density.

- Development of reciprocating compressors and expanders for operation in pressurised cycles at high absolute pressures, with the aim of improving efficiency and power density and lowering the costs per unit power.

- Exhaustive analysis of potential working fluids and ranges of operating conditions for transcritical PTES cycles, supported by detailed cycle analysis, with the aim of identifying those configurations that combine a high work ratio and a low variation in specific heat capacity. Detailed modelling of cycles that present a moderate variation in specific heat capacity but can employ a multi-stream heat exchanger and a small number of storage tanks at intermediate temperature levels as a counter-measure.

- Development of alternative thermal energy storage mechanisms, such as packed-beds employing a secondary (unpressurised) heat transfer fluid and latent heat storage processes with independent power and energy capacities.

- Detailed and comprehensive thermo-economic optimisation of the cycles described in this work, among other potentially promising configurations, with particular attention on employing cost equations that have been verified for all the required operating conditions. Determining the relative importance of different key metrics such as energy efficiency, capital cost and energy capacity, which are normally related by trade-offs.

6.6 Final remarks

Large-scale energy storage is an exciting and promising field of research which has imminent applications in the context of climate change mitigation and low-carbon power grids. Storing electricity in the form of high-grade thermal energy enables the use of cheap and abundant materials that can be kept inside large insulated tanks, leading to a high flexibility of location and a relatively high energy density. As an illustrative example, one cubic meter of water at a height of 500 m contains 1.4 kWh of exergy (i.e. energy that may be transformed into electrical work), while one cubic meter of hot water on flat ground contains 12 kWh of exergy. The challenge, however, rests on identifying the best configuration of thermodynamic cycle, operating conditions and storage materials that leads to a storage system with high efficiency and low overall cost, as well as on finding ways to improve the performance of critical cycle components such as heat exchangers, compressors and expanders. This thesis has proposed and studied several cycle configurations and found some of them to be particularly promising in terms of efficiency, energy density and cost. It has also explored the design and optimisation of heat exchangers according to the same goals.

There is still room for further development and optimisation of novel cycle configurations. However, the urgency with which large-scale energy storage solutions are needed indicates that efforts should also be placed in bringing existing designs to the demonstration and commercial phases as soon as possible. If significant advancements are made along the next decade or two, pumped thermal energy storage and liquid energy storage could become a very significant tool to help solve the great puzzle for energy sustainability.

References

[1] H. Chen, T. Cong, W. Yang, C. Tan, Y. Li, and Y. Ding, “Progress in electrical energy storage system: A critical review,” *Progress in Natural Science*, vol. 19, no. 3, pp. 291–312, 2009.

[2] A. Gallo, J. Simões-Moreira, H. Costa, M. Santos, and E. Moutinho dos Santos, “Energy storage in the energy transition context: A technology review,” *Renewable and Sustainable Energy Reviews*, vol. 65, pp. 800–822, 2016.

[3] D. MacKay, *Sustainable Energy - without the hot air*. UIT Cambridge, 2008. Available free online from www.withouthotair.com.

[4] J. Tester, E. Drake, M. Driscoll, M. Golay, and W. Peters, *Sustainable Energy: Choosing Among Options*. Massachusetts Institute of Technology, second ed., 2012.

[5] G. Boyle, B. Everett, and J. Ramage, *Energy Systems and Sustainability. Power for a sustainable future*. Oxford University Press, 2003.

[6] F. Díaz-González, A. Sumper, O. Gomis-Bellmunt, and R. Villafáfila-Robles, “A review of energy storage technologies for wind power applications,” *Renewable and Sustainable Energy Reviews*, vol. 16, no. 4, pp. 2154–2171, 2012.

[7] D. O. Akinyele and R. K. Rayudu, “Review of energy storage technologies for sustainable power networks,” *Sustainable Energy Technologies and Assessments*, vol. 8, pp. 74–91, 2014.

[8] A. F. Ghoniem, “Needs, resources and climate change: Clean and efficient conversion technologies,” *Progress in Energy and Combustion Science*, vol. 37, no. 1, pp. 15–51, 2011.

[9] IPCC, *Climate Change 2014: Synthesis Report. Contribution of Working Groups I, II and III to the Fifth Assessment Report of the Intergovernmental Panel on Climate Change*. 2014.

[10] UNFCCC, “Paris Agreement,” tech. rep., 2015.

[11] European Parliament, “Directive 2009/28/EC of the European Parliament and of the Council of 23 April 2009,” *Official Journal of the European Union*, vol. 140, no. 16, pp. 16–62, 2009.

[12] International Energy Agency, “World Energy Outlook 2017,” tech. rep., 2017.

[13] X. Luo, J. Wang, M. Dooner, and J. Clarke, “Overview of current development in electrical energy storage technologies and the application potential in power system operation,” *Applied Energy*, vol. 137, pp. 511–536, 2015.

[14] G. Strbac, M. Aunedi, D. Pudjianto, P. Djapic, F. Teng, A. Sturt, D. Jackravut, R. Sansom, V. Yufit, and N. Brandon, “Strategic Assessment of the Role and Value of Energy Storage Systems in the UK Low Carbon Energy Future,” *Energy Futures Lab, Imperial College London*, 2012.

[15] US Department Of Energy, “Global Energy Storage Database,” *energystorageexchange.org*, 2018.

[16] Electric Power Research Institute, “Electric Energy Storage Technology Options: A White Paper Primer on Applications, Costs and Benefits,” tech. rep., Palo Alto, California, 2010.

[17] M. Aneke and M. Wang, “Energy storage technologies and real life applications. A state of the art review,” *Applied Energy*, vol. 179, pp. 350–377, 2016.

[18] M. Budt, D. Wolf, R. Span, and J. Yan, “A review on compressed air energy storage: Basic principles, past milestones and recent developments,” *Applied Energy*, vol. 170, pp. 250–268, 2016.

[19] C. Bullough, C. Gatzen, C. Jakiel, M. Koller, A. Nowi, and S. Zunft, “Advanced Adiabatic Compressed Air Energy Storage for the Integration of Wind Energy,” *Proceedings of the European Wind Energy Conference*, no. November, pp. 22–25, 2004.

[20] H. Xue and A. White, “A comparative study of liquid, solid and hybrid adiabatic compressed air energy storage systems,” *Journal of Energy Storage*, vol. 18, no. May, pp. 349–359, 2018.

[21] C. Qin and E. Loth, “Liquid piston compression efficiency with droplet heat transfer,” *Applied Energy*, vol. 114, pp. 539–550, 2014.

[22] A. J. Pimm, S. D. Garvey, and M. de Jong, “Design and testing of Energy Bags for underwater compressed air energy storage,” *Energy*, vol. 66, pp. 496–508, 2014.

[23] B. C. Cheung, R. Carriveau, and D. S. K. Ting, “Multi-objective optimization of an underwater compressed air energy storage system using genetic algorithm,” *Energy*, vol. 74, no. C, pp. 396–404, 2014.

[24] W. D. Steinmann, “Thermo-mechanical concepts for bulk energy storage,” *Renewable and Sustainable Energy Reviews*, vol. 75, no. October 2016, pp. 205–219, 2017.

[25] A. White, G. Parks, and C. Markides, “Thermodynamic analysis of pumped thermal electricity storage,” *Applied Thermal Engineering*, vol. 53, no. 2, pp. 291–298, 2013.

[26] Y. Kim, D. Shin, S. Lee, and D. Favrat, “Isothermal transcritical CO2 cycles with TES (thermal energy storage) for electricity storage,” *Energy*, vol. 49, pp. 484–501, 2012.

[27] A. Benato and A. Stoppato, “Pumped Thermal Electricity Storage: A technology overview,” *Thermal Science and Engineering Progress*, vol. 6, pp. 301–315, 2018.

[28] M. Abarr, B. Geels, J. Hertzberg, and L. D. Montoya, “Pumped thermal energy storage and bottoming system part A: Concept and model,” *Energy*, pp. 1–12, 2016.

[29] T. Desrues, J. Ruer, P. Marty, and J. F. Fourmigué, “A thermal energy storage process for large scale electric applications,” *Applied Thermal Engineering*, vol. 30, no. 5, pp. 425–432, 2010.

[30] J. Howes, “Concept and development of a pumped heat electricity storage device,” *Proceedings of the IEEE*, vol. 100, no. 2, pp. 493–503, 2012.

[31] A. White, J. McTigue, and C. Markides, “Wave propagation and thermodynamic losses in packed-bed thermal reservoirs for energy storage,” *Applied Energy*, vol. 130, pp. 648–657, 2014.

[32] A. J. White, J. D. McTigue, and C. N. Markides, “Analysis and optimisation of segmented packed-bed thermal reservoirs for electricity storage applications,” in *Proc IMechE Part A: J Power and Energy*, vol. 230, pp. 739–754, 2016.

[33] J. McTigue, A. White, and C. Markides, “Parametric studies and optimisation of pumped thermal electricity storage,” *Applied Energy*, vol. 137, pp. 800–811, 2015.

[34] J. McTigue, *Analysis and Optimisation of Thermal Energy Storage*. PhD thesis, University of Cambridge, 2016.

[35] J. D. McTigue, C. N. Markides, and A. J. White, "Performance response of packed-bed thermal storage to cycle duration perturbations," *Journal of Energy Storage*, vol. 19, no. August, pp. 379–392, 2018.

[36] F. Ni and H. S. Caram, "Analysis of pumped heat electricity storage process using exponential matrix solutions," *Applied Thermal Engineering*, vol. 84, pp. 34–44, 2015.

[37] A. Smallbone, V. Jülch, R. Wardle, and A. P. Roskilly, "Levelised Cost of Storage for Pumped Heat Energy Storage in comparison with other energy storage technologies," *Energy Conversion and Management*, vol. 152, no. May, pp. 221–228, 2017.

[38] P. Farres-Antunez, "Modelling of Thermal Energy Storage for Bulk Electricity Storage," tech. rep., Cambridge University Engineering Department, Cambridge, 2015.

[39] P. Farres-Antunez and A. J. White, "Optimization of heat exchangers operating with real fluids for thermo-mechanical energy storage," in *Offshore Energy and Storage Symposium*, (Malta), 2016.

[40] P. Farres-Antunez and A. White, "Thermodynamic strategies for Pumped Thermal Exergy Storage with liquid reservoirs," in *UK Energy Storage Conference*, (Birmingham), 2016.

[41] J. Edge, "UK Energy Storage Conference," *Johnson Matthey Technology Review*, vol. 61, no. 3, pp. 222—-226, 2017.

[42] P. Farres-Antunez, H. Xue, and A. J. White, "Thermodynamic analysis of a combined pumped thermal and liquid air energy storage cycle," in *Offshore Energy and Storage Symposium*, (Cape Cod), 2017.

[43] P. Farres-Antunez, H. Xue, and A. J. White, "Thermodynamic analysis and optimisation of a combined liquid air and pumped thermal energy storage cycle," *Journal of Energy Storage*, vol. 18, no. Offshore Energy Storage, pp. 90–102, 2018.

[44] R. B. Laughlin, "Pumped thermal grid storage with heat exchange," *Journal of Renewable and Sustainable Energy*, vol. 9, no. 4, p. 044103, 2017.

[45] W. D. Steinmann, "The CHEST (Compressed Heat Energy STorage) concept for facility scale thermo mechanical energy storage," *Energy*, vol. 69, pp. 543–552, 2014.

[46] V. Zipf, A. Neuhäuser, D. Willert, P. Nitz, S. Gschwander, and W. Platzer, "High temperature latent heat storage with a screw heat exchanger: Design of prototype," *Applied Energy*, vol. 109, pp. 462–469, 2013.

[47] H. Pointner, W. D. Steinmann, and M. Eck, "Introduction of the PCM flux concept for latent heat storage," in *Energy Procedia*, vol. 57, pp. 643–652, 2014.

[48] R. B. Peterson, "A concept for storing utility-scale electrical energy in the form of latent heat," *Energy*, vol. 36, no. 10, pp. 6098–6109, 2011.

[49] S. Henchoz, F. Buchter, D. Favrat, M. Morandin, and M. Mercangöz, "Thermoeconomic analysis of a solar enhanced energy storage concept based on thermodynamic cycles," *Energy*, vol. 45, no. 1, pp. 358–365, 2012.

[50] A. Dietrich, F. Dammel, and P. Stephan, "Exergoeconomic analysis of a Pumped Heat Electricity Storage system with concrete thermal energy storage," *International Journal of Thermodynamics*, vol. 19, no. 1, pp. 43–51, 2016.

[51] G. F. Frate, M. Antonelli, and U. Desideri, "A novel Pumped Thermal Electricity Storage (PTES) system with thermal integration," *Applied Thermal Engineering*, vol. 121, pp. 1051–1058, 2017.

[52] H. Jockenhöfer, W. D. Steinmann, and D. Bauer, "Detailed numerical investigation of a pumped thermal energy storage with low temperature heat integration," *Energy*, vol. 145, pp. 665–676, 2018.

[53] M. Mercangöz, J. Hemrle, L. Kaufmann, A. Z'Graggen, and C. Ohler, "Electrothermal energy storage with transcritical CO2 cycles," *Energy*, vol. 45, no. 1, pp. 407–415, 2012.

[54] M. Morandin, F. Maréchal, M. Mercangöz, and F. Buchter, "Conceptual design of a thermo-electrical energy storage system based on heat integration of thermodynamic cycles - Part A: Methodology and base case," *Energy*, vol. 45, no. 1, pp. 375–385, 2012.

[55] M. Morandin, F. Maréchal, M. Mercangöz, and F. Buchter, "Conceptual design of a thermo-electrical energy storage system based on heat integration of thermodynamic cycles - Part B: Alternative system configurations," *Energy*, vol. 45, no. 1, pp. 386–396, 2012.

[56] M. Morandin, M. Mercangöz, J. Hemrle, F. Maréchal, and D. Favrat, “Thermoeconomic design optimization of a thermo-electric energy storage system based on transcritical CO2 cycles,” *Energy*, vol. 58, pp. 571–587, 2013.

[57] N. Tauveron, E. Macchi, D. Nguyen, and T. Tartière, “Experimental Study of Supercritical CO 2 Heat Transfer in a Thermo-Electric Energy Storage Based on Rankine and Heat-Pump Cycles,” *Energy Procedia*, vol. 129, pp. 939–946, 2017.

[58] S. A. Wright, A. Z. Graggen, and J. Hemrle, “Control of a supercritical CO2 electro-thermal energy storage system,” in *ASME Turbo Expo 2013*, (San Antonio), pp. 1–9, 2013.

[59] Y.-J. Baik, J. Heo, J. Koo, and M. Kim, “The effect of storage temperature on the performance of a thermo-electric energy storage using a transcritical CO2 cycle,” *Energy*, vol. 75, pp. 204–215, 2014.

[60] F. Ayachi, N. Tauveron, T. Tartière, S. Colasson, and D. Nguyen, “Thermo-Electric Energy Storage involving CO2 transcritical cycles and ground heat storage,” *Applied Thermal Engineering*, vol. 108, pp. 1418–1428, 2016.

[61] P. Vinnemeier, M. Wirsum, D. Malpiece, and R. Bove, “Integration of heat pumps into thermal plants for creation of large-scale electricity storage capacities,” *Applied Energy*, vol. 184, pp. 506–522, 2016.

[62] M. Abarr, J. Hertzberg, and L. D. Montoya, “Pumped Thermal Energy Storage and Bottoming System Part B: Sensitivity analysis and baseline performance,” *Energy*, 2016.

[63] B. Kantharaj, S. Garvey, and A. Pimm, “Compressed air energy storage with liquid air capacity extension,” *Applied Energy*, vol. 157, pp. 152–164, 2015.

[64] R. Morgan, S. Nelmes, E. Gibson, and G. Brett, “Liquid air energy storage - Analysis and first results from a pilot scale demonstration plant,” *Applied Energy*, vol. 137, pp. 845–853, 2015.

[65] G. L. Guizzi, M. Manno, L. M. Tolomei, and R. M. Vitali, “Thermodynamic analysis of a liquid air energy storage system,” *Energy*, vol. 93, pp. 1639–1647, 2015.

[66] E. M. Smith, “Storage of electrical energy using supercritical liquid air,” *Proceedings of the Institution of Mechanical Engineers*, vol. 191, no. 1977, pp. 289–298, 1977.

[67] K. Kishimoto, K. Hasegawa, and T. Asano, “Development of generator of liquid air storage energy system,” *Mitsubishi Juko Giho*, vol. 35, pp. 60–63, 1998.

[68] K. Chino and H. Araki, “Evaluation of energy storage method using liquid air,” *Heat Transfer - Asian Research*, vol. 29, no. 5, pp. 347–357, 2000.

[69] A. Sciacovelli, A. Vecchi, and Y. Ding, “Liquid air energy storage (LAES) with packed bed cold thermal storage. From component to system level performance through dynamic modelling,” *Applied Energy*, vol. 190, pp. 84–98, 2017.

[70] Highview Power, “Highview Power launches world’s first grid-scale liquid air energy storage plant,” 2018.

[71] P. Krawczyk, L. Szablowski, K. Badyda, S. Karellas, and E. Kakaras, “Impact of selected parameters on performance of the Adiabatic Liquid Air Energy Storage system,” *Journal of Power Technologies*, vol. 96, no. 4, pp. 238–244, 2016.

[72] S. Georgiou, N. Shah, and C. N. Markides, “A thermo-economic analysis and comparison of pumped-thermal and liquid-air electricity storage systems,” *Applied Energy*, vol. 226, no. June, pp. 1119–1133, 2018.

[73] C. Xie, Y. Hong, Y. Ding, Y. Li, and J. Radcliffe, “An economic feasibility assessment of decoupled energy storage in the UK: With liquid air energy storage as a case study,” *Applied Energy*, vol. 225, no. May, pp. 244–257, 2018.

[74] Y. Li, H. Cao, S. Wang, Y. Jin, D. Li, X. Wang, and Y. Ding, “Load shifting of nuclear power plants using cryogenic energy storage technology,” *Applied Energy*, vol. 113, pp. 1710–1716, 2014.

[75] Y. Li, X. Wang, Y. Jin, and Y. Ding, “An integrated solar-cryogen hybrid power system,” *Renewable energy*, vol. 37, no. 1, pp. 76–81, 2012.

[76] A. J. Pimm, S. D. Garvey, and B. Kantharaj, “Economic analysis of a hybrid energy storage system based on liquid air and compressed air,” *Journal of Energy Storage*, vol. 4, pp. 24–35, 2015.

[77] J. Howes and J. Macnaghten, “Hybrid energy storage system. GB 2537126 A,” 2016.

[78] W.-D. Steinmann, D. Laing, and C. Odenthal, “Development of the CellFlux Storage Concept for Sensible Heat,” *Journal of Solar Energy Engineering*, vol. 136, no. 1, p. 011011, 2013.

[79] W. Steinmann, "Thermal energy storage systems for concentrating solar power (CSP) technology," in *Advances in Thermal Energy Storage Systems*, ch. 21, pp. 511–531, Elsevier Ltd. Knovel, 2015.

[80] I. Bell, J. Wronski, S. Quoilin, and V. Lemort, "Pure and pseudo-pure fluid thermophysical property evaluation and the open-source thermophysical property library coolprop," *Industrial and Engineering Chemistry Research*, vol. 53, no. 6, pp. 2498–2508, 2014.

[81] MEGlobal, "Ethylene glycol. Product guide," tech. rep., 2008.

[82] A. Mawire, "Performance of Sunflower Oil as a sensible heat storage medium for domestic applications," *Journal of Energy Storage*, vol. 5, pp. 1–9, 2016.

[83] B. Esteban, J. R. Riba, G. Baquero, A. Rius, and R. Puig, "Temperature dependence of density and viscosity of vegetable oils," *Biomass and Bioenergy*, vol. 42, pp. 164–171, 2012.

[84] Shell Lubricants, "Shell Heat Transfer Oil S2. Technical Data Sheet," tech. rep., 2010.

[85] K. Vignarooban, X. Xu, A. Arvay, K. Hsu, and A. M. Kannan, "Heat transfer fluids for concentrating solar power systems - A review," *Applied Energy*, vol. 146, pp. 383–396, 2015.

[86] T. Bauer, N. Pfleger, N. Breidenbach, M. Eck, D. Laing, and S. Kaesche, "Material aspects of Solar Salt for sensible heat storage," *Applied Energy*, vol. 111, pp. 1114–1119, 2013.

[87] A. G. Mozgovoi, V. V. Roshchupkin, S. N. Skovorod'Ko, M. A. Pokrasin, and A. I. Chernov, "The Density of Liquid Sodium-Potassium Eutectic," *High Temperature*, vol. 41, no. 3, pp. 340–345, 2003.

[88] Tradingeconomics.com, "Propane prices, 2009-2018 data," 2018.

[89] Anglian Water, "Domestic water metered charges," 2018.

[90] U. Herrmann, B. Kelly, and H. Price, "Two-tank molten salt storage for parabolic trough solar power plants," *Energy*, vol. 29, no. 5-6, pp. 883–893, 2004.

[91] R. K. Shah and D. P. Sekulic, *Fundamentals of heat exchanger design*. New Jersey: John Wiley & Sons, 2003.

[92] D. Aquaro and M. Pieve, “High temperature heat exchangers for power plants: Performance of advanced metallic recuperators,” *Applied Thermal Engineering*, vol. 27, pp. 389–400, feb 2007.

[93] S. Baek, J. H. Kim, S. Jeong, and J. Jung, “Development of highly effective cryogenic printed circuit heat exchanger (PCHE) with low axial conduction,” *Cryogenics*, vol. 52, no. 7-9, pp. 366–374, 2012.

[94] E. Marquardt and R. Radebaugh, “Compact High Effectiveness Parallel Plate Heat Exchangers,” in *Cryocoolers 12* (R. Ross, ed.), pp. 507–516, Kluwer Academic, 2003.

[95] S. Ashman and S. G. Kandlikar, “A Review of Manufacturing Processes for Microchannel Heat Exchanger Fabrication,” in *ASME 4th International Conference on Nanochannels, Microchannels, and Minichannels*, pp. 855–860, ASME, 2006.

[96] B. Cárdenas, S. Garvey, B. Kantharaj, and M. Simpson, “Parametric investigation of a non-constant cross sectional area air to air heat exchanger,” *Applied Thermal Engineering*, vol. 113, pp. 278–289, 2017.

[97] F. Incropera, D. DeWitt, T. Bergman, and A. Lavine, *Fundamentals of Heat and Mass Transfer*. John Wiley and Sons, 7th ed., 2011.

[98] D. Southall, R. L. Pierres, and S. J. Dewson, “Design Considerations for Compact Heat Exchangers,” in *Proceedings of ICAPP 2008*, pp. 1953–1968, 2008.

[99] A. Bejan, “The concept of irreversibility in heat exchanger design: counterflow heat exchangers for gas-to-gas applications,” *Journal of Heat Transfer*, vol. 99, no. 3, p. 374, 1977.

[100] H. Dixon, *Fluid Mechanics and Thermodynamics of Turbomachinery (6th Edition)*. Elsevier, nov 2010.

[101] A. White, “Thermodynamic analysis of the reverse Joule-Brayton cycle heat pump for domestic heating,” *Applied Energy*, vol. 86, no. 11, pp. 2443–2450, 2009.

[102] C. Périlhon, S. Lacour, P. Podevin, and G. Descombes, “Thermal electricity storage by a thermodynamic process: Study of temperature impact on the machines,” *Energy Procedia*, vol. 36, pp. 923–938, 2013.

[103] W. Kays and A. London, *Compact heat exchangers*. New York: McGraw-Hill, third ed., 1984.

[104] S. Wrenick, P. Sutor, H. Pangilinan, and E. Schwarz, “Heat Transfer Properties of Engine Oils,” in *ASME World Tribology Congress III*, pp. 595–596, 2005.

[105] L. Zhou, J. S. Kapat, L. C. Chow, and X. Li, “Design of a High Effectiveness Micro Heat Exchanger for Mars Applications,” tech. rep., Society of Automotive Engineers, 2000.

[106] National Energy Technology Laboratory, “Process Equipment Cost Estimation, Final Report,” Tech. Rep. January, 2002.

[107] E. Hylton and H. Kimmel, “Exducer Turbines, the Optimized Solution for LNG Expanders,” in *Gastech 2oo2*, 2002.

[108] R. A. Waltz, J. L. Morales, J. Nocedal, and D. Orban, “An interior algorithm for nonlinear optimization that combines line search and trust region steps,” *Mathematical Programming*, vol. 107, no. 3, pp. 391–408, 2006.

[109] C. Odenthal, F. Klasing, and T. Bauer, “Demonstrating Cost Effective Thermal Energy Storage in Molten Salts: DLR’s TESIS Test Facility,” *Energy Procedia*, vol. 135, pp. 14–22, 2017.

[110] O. N. Igobo and P. a. Davies, “Review of low-temperature vapour power cycle engines with quasi-isothermal expansion,” *Energy*, vol. 70, pp. 22–34, 2014.

[111] C. Qin, E. Loth, P. Li, T. Simon, and J. Van De Ven, “Spray-cooling concept for wind-based compressed air energy storage,” *Journal of Renewable and Sustainable Energy*, vol. 6, no. 4, pp. 1–16, 2014.

[112] J. D. Van de Ven and P. Y. Li, “Liquid piston gas compression,” *Applied Energy*, vol. 86, no. 10, pp. 2183–2191, 2009.

[113] B. Yan, J. Wieberdink, F. Shirazi, P. Y. Li, T. W. Simon, and J. D. Van de Ven, “Experimental study of heat transfer enhancement in a liquid piston compressor/expander using porous media inserts,” *Applied Energy*, vol. 154, pp. 40–50, 2015.

[114] D. Wolf and M. Budt, “LTA-CAES - A low-temperature approach to adiabatic compressed air energy storage,” *Applied Energy*, vol. 125, pp. 158–164, 2014.

[115] C. Windmeier and R. F. Barron, “Cryogenic Technology,” in *Ullmann’s Encyclopedia of Industrial Chemistry*, pp. 1–71, Weinheim, Germany: Wiley-VCH Verlag GmbH & Co. KGaA, 2013.

[116] F. A. McClintock, “The design of heat exchangers for minimum irreversibility,” *ASME Paper*, vol. 51, 1951.

[117] A. Bejan, “General criterion for rating heat-exchanger performance,” *International Journal of Heat and Mass Transfer*, vol. 21, no. 5, pp. 655–658, 1978.

[118] A. Bejan, *Entropy generation minimization: the method of thermodynamic optimization of finite-size systems and finite-time processes*. CRC press, 1995.

[119] A. Bejan, “Entropy generation minimization: The new thermodynamics of finite-size devices and finite-time processes,” *Journal of Applied Physics*, vol. 79, no. 3, p. 1191, 1996.

[120] J. C. Ordonez and A. Bejan, “Entropy generation minimization in parallel-plates counter flow heat exchangers,” *International Journal of Energy Research*, vol. 24, no. August 1999, pp. 843–864, 2000.

[121] A. Bejan, “Fundamentals of exergy analysis, entropy generation minimization, and the generation of flow architecture,” *International Journal of Energy Research*, vol. 26, no. 7, pp. 0–43, 2002.

[122] L. C. Witte and N. Shamsundar, “A Thermodynamic Efficiency Concept for Heat Exchange Devices,” *Journal of Engineering for Power*, vol. 105, no. 1, 1983.

[123] a. L. London and R. K. Shah, “Costs of Irreversibilities in Heat Exchanger Design,” *Heat Transfer Engineering*, vol. 4, no. 2, pp. 59–73, 1983.

[124] D. P. Sekulić, “Entropy generation in a heat exchanger,” *Heat Transfer Engineering*, vol. 7, no. 1-2, pp. 83–88, 1986.

[125] K. Manjunath and S. C. Kaushik, “Second law thermodynamic study of heat exchangers: A review,” *Renewable and Sustainable Energy Reviews*, vol. 40, pp. 348–374, 2014.

[126] M. Yilmaz, O. Sara, and S. Karsli, “Performance evaluation criteria for heat exchangers based on second law analysis,” *Exergy, An International Journal*, vol. 1, no. 4, pp. 278–294, 2001.

[127] K. Chowdhury and S. Sarangi, “A second law analysis of the concentric tube heat exchanger: optimisation of wall conductivity,” *International Journal of Heat and Mass Transfer*, vol. 26, no. 5, pp. 783–786, 1983.

[128] M. E. Will and a. T. a. M. De Waele, “Heat exchanger versus regenerator: A fundamental comparison,” *Cryogenics*, vol. 45, pp. 473–480, 2005.

[129] P. P. P. M. Lerou, T. T. Veenstra, J. F. Burger, H. J. M. Ter Brake, and H. Rogalla, “Optimization of counterflow heat exchanger geometry through minimization of entropy generation,” *Cryogenics*, vol. 45, no. 10-11, pp. 659–669, 2005.

[130] E. S. Kim, C. H. Oh, and S. Sherman, “Simplified optimum sizing and cost analysis for compact heat exchanger in VHTR,” *Nuclear Engineering and Design*, vol. 238, no. 10, pp. 2635–2647, 2008.

[131] S.-j. Yoon, P. Sabharwall, and E.-s. Kim, “Analytical Study on Thermal and Mechanical Design of Printed Circuit Heat Exchanger,” Tech. Rep. September, Idaho National Laboratory, 2013.

[132] G. Harpole and J. Eninger, “Micro-channel heat exchanger optimization,” in *1991 Proceedings, Seventh IEEE Semiconductor Thermal Measurement and Management Symposium*, pp. 59–63, IEEE.

[133] J. Figley, X. Sun, S. K. Mylavarapu, and B. Hajek, “Numerical study on thermal hydraulic performance of a Printed Circuit Heat Exchanger,” *Progress in Nuclear Energy*, vol. 68, pp. 89–96, 2013.

[134] M. Chen, X. Sun, R. N. Christensen, S. Shi, I. Skavdahl, V. Utgikar, and P. Sabharwall, “Experimental and numerical study of a printed circuit heat exchanger,” *Annals of Nuclear Energy*, vol. 97, pp. 221–231, 2016.

[135] A. Vyatskikh, S. Delalande, A. Kudo, X. Zhang, C. M. Portela, and J. R. Greer, “Additive manufacturing of 3D nano-architected metals,” *Nature Communications*, vol. 9, no. 1, p. 593, 2018.

[136] R. W. Whitesides, “Process Equipment Estimating by Ratio and Proportion,” *Course notes, PDH Course G*, vol. 127, pp. 1–8, 2012.

[137] M. Tribe and R. Alpine, “Scale economies and the "0.6 rule",” *Engineering Costs and Production Economics*, vol. 10, pp. 271–278, mar 1986.

[138] A. Valero, M. A. Lozano, L. Serra, C. Frangopoulos, and M. R. V. Spakovsky, “CGAM problem: Definition and conventional solution,” *Pergamon Energy*, vol. 19, no. 3, pp. 279–286, 1994.

[139] Y. Kato, T. Nitawaki, and Y. Muto, "Medium temperature carbon dioxide gas turbine reactor," *Nuclear Engineering and Design*, vol. 230, no. 1-3, pp. 195–207, 2004.

[140] J. D. Denton, "Introductory review of basic principles," in *Cambridge Turbomachinery Course*, pp. 1–25, 2004.

[141] C. F. McDonald, "Helium turbomachinery operating experience from gas turbine power plants and test facilities," *Applied Thermal Engineering*, vol. 44, pp. 108–142, 2012.

[142] M. Adolfsson and S. Rashid, *Life Cycle Assessment and Life Cycle Cost of Heat Exchangers. A Case for Inter Terminals Sweden AB Located in Port of Gothenburg*. PhD thesis, Chalmers University of Technology, Sweden, 2016.

[143] H. Piili, A. Happonen, T. Väistö, V. Venkataramanan, J. Partanen, and A. Salminen, "Cost Estimation of Laser Additive Manufacturing of Stainless Steel," *Physics Procedia*, vol. 78, no. August, pp. 388–396, 2015.

[144] A. Traverso, A. F. Massardo, W. Cazzola, and G. Lagorio, "Widget-Temp: A novel web-based approach for thermoeconomic analysis and optimization of conventional and innovative cycles," *Proceedings of ASME-IGTI Turbo Expo*, 2004.

Appendix A

Outputs of the PTES numerical model

Gas states and liquid streams

```
PTES CYCLE (above-ambient regeneration)
---------------------------------------
Gas states:
      T [K]     p [bar]    h [MJ/kg] s [kJ/kg/K] mdot [kg/s]    Inlet of       Cycle
      551.5        24.4        0.57        6.53        10.0        comp          ch
      860.0       106.4        0.92        6.58        10.0         hex          ch
      559.5       105.3        0.58        6.10        10.0       regen          ch
      313.3       105.3        0.31        5.45        10.0     hex_ext          ch
      293.1       105.3        0.28        5.37        10.0         exp          ch
      197.3        24.7        0.19        5.41        10.0         hex          ch
      290.1        24.4        0.30        5.85        10.0     hex_ext          ch
      293.1        24.4        0.30        5.86        10.0       regen          ch
      551.5        24.4        0.57        6.53        10.0        comp          ch

      555.7        24.4        0.58        6.54        10.0       regen         dis
      362.2        24.4        0.37        6.08        10.0     hex_ext         dis
      293.1        24.4        0.30        5.86        10.0         hex         dis
      205.0        24.2        0.20        5.46        10.0        comp         dis
      356.2       133.8        0.35        5.52        10.0       count         dis
      356.2       133.8        0.35        5.52        10.0       regen         dis
      539.1       133.8        0.56        5.99        10.0         hex         dis
      840.1       132.4        0.90        6.49        10.0         exp         dis
      555.7        24.4        0.58        6.54        10.0       regen         dis

Hot fluid streams:
-->SolarSalt
     Tin[K]     Tout[K]  Δh [MJ/kg] Δs [kJ/kg/K]   mdot[kg/s]     Stream       Cycle
      550.0       850.7        0.47        0.68        7.24           1          ch
      850.7       550.0       -0.47       -0.68        7.27           1         dis

Cold fluid streams:
-->Methanol
     Tin[K]     Tout[K]  Δh [MJ/kg] Δs [kJ/kg/K]   mdot[kg/s]     Stream       Cycle
      293.1       200.3       -0.21       -0.88        4.81           1          ch
      200.3       288.6        0.20        0.84        4.79           1         dis
```

First law balance

```
FIRST LAW BALANCE
-----------------
CHARGE
Net power input:             2.5 MW
Charge time:                10.0 h
Energy(el) input:           25.5 MWh
Heat to hot tanks:          33.7 MWh
Heat from cold tanks:       10.3 MWh
DH working fluid:            0.0 MWh
Heat rejected:               2.1 MWh
NET:                         0.0 MWh

DISCHARGE
Net power output:            1.7 MW
Discharge time:             10.0 h
Energy(el) output:          16.6 MWh
Heat from hot tanks:        33.7 MWh
Heat to cold tanks:          9.7 MWh
DH working fluid:            0.0 MWh
Heat rejected:               7.4 MWh
NET:                         0.0 MWh

Round trip efficiency:      65.2 %

Energy density:             46.25 kWh/m3
Power density (charge):      3.77 MW/(m3/s)
Power density (disch):       2.45 MW/(m3/s)

STORAGE MEDIA
     SolarSalt volume:       8.47 m3/MWh
      Methanol volume:      13.15 m3/MWh

     SolarSalt mass:        15.67 tons/MWh
      Methanol mass:        10.41 tons/MWh
```

Appendix B

Gas-liquid heat exchangers

The analytical optimisation procedure presented in chapter 4 was applied to gas-gas heat exchangers, but it can equally be applied to gas-liquid (or, indeed, liquid-liquid) heat exchangers as long as the following assumptions remain valid: (i) the HEX is balanced (i.e. equal $\dot{m}c_p$ for both streams), (ii) it is nearly ideal (i.e. $\Delta T \ll T$, $\Delta p \ll p$ and has adiabatic external walls) (iii) c_p variation is negligible, and (iv) it operates in the laminar regime. Of the previous four assumptions, number (iii) is the only one relatively likely to stop being valid when employing liquid fluids, especially if there is a large temperature difference between inlet and outlet. If c_p variation becomes significant, numerical optimisation is necessary (see section 4.6). On the other hand, in cases where the four previous assumptions remain valid, the analytical procedure may be used after adapting the expressions of $K_{\Delta p1}$ and $K_{\lambda 1}$ in Eq. (4.32) (while $K_{\Delta T1}$ remains the same). $K_{\Delta p1}$ must be adapted because it contains the assumption of the fluid being an ideal gas, while $K_{\lambda 1}$ must be adapted only if the conductivity of the liquid is non-negligible with respect to the conductivity of the heat exchanger material. It is straightforward to prove that, for a liquid,

$$K_{\Delta p1} = \left(\frac{2a_\mathrm{L} A_* \mu \dot{m} v^2}{c_p T} \right)_1$$

and

$$K_{\lambda 1} = \left(\frac{\tau^2}{\dot{m} c_p A_*} \left[k_\mathrm{m} A_* + k \right] \right)_1$$

while the rest of the analysis remains the same.

There are two main reasons why liquid fluids are generally more efficient at exchanging heat than gases: (i) they tend to have a much higher thermal conductivity[1], and (ii) they

---

[1] E.g. the thermal conductivity of water falls from $0.68\,\mathrm{W/(m\,K)}$ to $0.025\,\mathrm{W/(m\,K)}$ when turning from liquid to vapour, while for oxygen it falls from $0.15\,\mathrm{W/(m\,K)}$ to $0.0084\,\mathrm{W/(m\,K)}$.

have a much higher density (i.e. smaller v). The higher k reduces the value of $K_{\Delta T1}$ (and increases slightly the value of $K_{\lambda 1}$), while the smaller v reduces the value of $K_{\Delta p1}$. The effect on $K_{\Delta p1}$ is particularly strong, such that some authors neglect the contribution of flow friction into $\dot{S}_{\mathrm{irr}}$ when operating with liquid fluids. As a result of these changes, an optimised HEX stream will tend to be longer and have smaller channels when operating with a liquid than when operating with a gas.

Appendix C

Cross-sectional area of the heat exchanger material

In order to compute the volume of heat exchanger material and the magnitude of axial conduction, one must find the ratio between the cross-sectional area of the material and the cross-sectional area of the fluid flowing through it. Consider the simple structure shown in Figure C.1. The structure contains a large number of circular channels of diameter D, separated from each other by a horizontal distance $2t$, and separated from the adjacent plates by a distance t. The design corresponds to horizontally placing a number of pipes of diameter D and thickness t and filling the gaps in between with extra material. The design is chosen as an example because of its simplicity and because of the high pressure containment capability of circular pipes, and could potentially be built employing traditional micro-channel manufacturing techniques, such as those described in [95], or more modern techniques such as additive manufacturing. However, a vast number of different structures are possible, including significantly intricate designs, such as the one proposed in [96].

In order to determine the minimum value of the thickness t, one must equate the hoop stress at the pipe wall (due to the internal pressure p) to the maximum allowable stress of the material. The result is,

$$\frac{t}{D} = \frac{p}{2\sigma_{\max}} \tag{C.1}$$

However, this might in some cases lead to unrealistic results. For example, taking $p = 5\,\text{bar}$ and $\sigma_{\max} = 1000\,\text{bar}$ (reference value for stainless steel) gives $t/D = 2.5 \cdot 10^{-3}$, which could be in conflict with manufacturing or structural constraints. Therefore, setting a minimum t/D becomes necessary. Once this ratio is known, the cross-sectional area of HEX material associated with each stream can be found from:

$$A_{\mathrm{m}} = \left[(D+t)^2 - \frac{\pi D^2}{4}\right] N = A_{\mathrm{f}} \left[\frac{4}{\pi}\left(1+\frac{t}{D}\right)^2 - 1\right] \tag{C.2}$$

where Equation (4.41) was used for the total number of channels. Thus, A_{m} becomes equal to the flow cross-sectional area times a non-dimensional parameter which is a function of t/D, which itself is either a constant or a function of p/σ_{max}. The ratio between A_{m} and A_{f} is defined as A_* (Eq. (4.26)), and is also equal to the ratio between the volume of material and the flow volume.

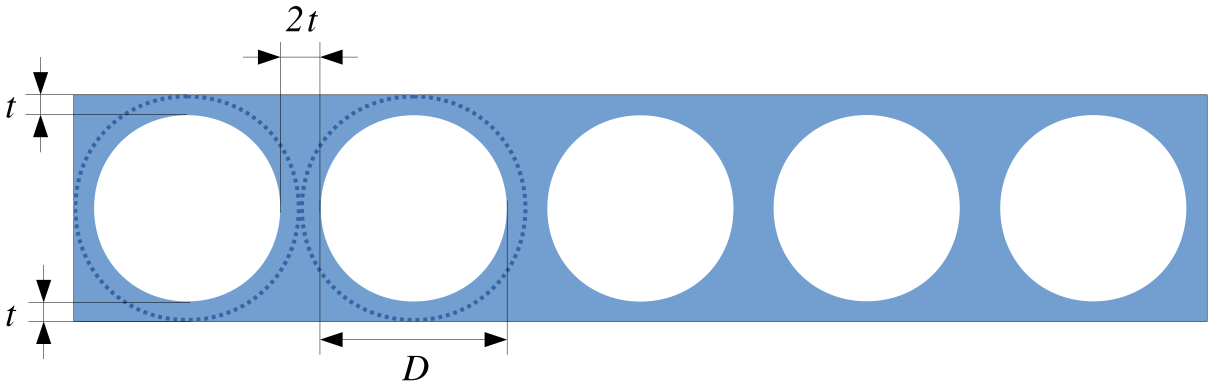

Figure C.1: Detail of a section of a possible HEX stream.

Appendix D

Thermal resistance of the heat exchanger material

One assumption which is commonly made in the analysis of heat exchangers is that the thermal resistance of the wall separating the fluid streams is negligible compared to the thermal resistance of the fluid streams themselves. Here the validity of this assumption is verified. The thermal resistance of a fluid stream is (assuming laminar flow and employing Eq. (4.5)):

$$R_{\mathrm{t,f}} = \frac{1}{hA} = \frac{D}{b_{\mathrm{L}} k A} \tag{D.1}$$

On the other hand, the thermal resistance of the heat exchanger wall can be expressed as:

$$R_{\mathrm{t,m}} = \frac{t_{\mathrm{eff}}}{A k_{\mathrm{m}}} \tag{D.2}$$

where t_{eff} is an effective thickness that depends on the geometry of the channels. For example, for a flat plate, t_{eff} is simply the plate thickness, while for a circular pipe $t_{\mathrm{eff}} = \ln(1+2t/D)\,D/2$, which again reduces to $t_{\mathrm{eff}} = t$ for $t \ll D$. The ratio between the two thermal resistances is:

$$\frac{R_{\mathrm{t,m}}}{R_{\mathrm{t,f}}} = \frac{b_{\mathrm{L}} t_{\mathrm{eff}}}{D} \frac{k}{k_{\mathrm{m}}} \tag{D.3}$$

where the first term on the right hand side depends on the geometry of the HEX and is likely to be $\lesssim 1$, while the second term depends on the conductivities of the fluid and of the wall. In the case of the fluid being a gas and the wall being metallic, $k/k_{\mathrm{m}} \ll 1$ and therefore neglecting R_{m} is justified. For instance, a combination of helium (gas with high k) and stainless steel (metal with low k_{m}) leads to $k/k_{\mathrm{m}} \approx 0.01$, while much lower values are obtained for other gas/metal combinations (e.g. argon and aluminium).

Nevertheless, in cases where R_{m} is non negligible, its effect on the entropy generation can be easily accounted by including its contribution into $K_{\Delta T}$ in Eq. (4.32). It is straightforward to prove that, in this case,

$$K_{\Delta T1} = \left(\frac{\tau^2 A_* \dot{m} c_p}{4} \left(\frac{1}{b_L k} + \frac{t_{\text{eff}}}{k_{\text{m}} D} \right) \right)_1$$

where the t_{eff}/D ratio is, in many cases, a constant that depends on the internal pressure of the flow and the allowable stress of the material. The minimum possible value of N_{s1} (Eq. (4.37)) becomes, then,

$$N_{s1,\min} = 3 \left(\frac{a_{\text{L}} \tau^4 A_*^2}{2} \left(\frac{k_{\text{m}}}{b_L k} + \frac{t_{\text{eff}}}{D} \right) \frac{R}{c_p} \frac{\mu v}{p} \frac{\dot{m}}{V_{\text{m}}} \right)_1^{1/3}$$

where, noticeably, the inclusion of the t_{eff}/D term prevents the appearance of a physically unrealistic result: that $N_{s1,\min}$ could be made infinitesimally small by choosing a heat exchanger material with extremely low thermal conductivity.

Appendix E

Summary of optimised parameters for two exemplary regenerators

Table E.1: Inputs of the analytical optimisation procedure, for two regenerators (one employing helium, the other employing argon) with an effectiveness of 99 %.

		Helium-Helium	Argon-Argon
Parameter	Unit	Value	
p_1	bar	5	
p_2	bar	50	
T_1	K	200	
T_2	K	290	
σ_{max}	bar	1000	
k_{m}	W/m/K	15	
L_{min}	mm	200	
$(t/D)_{\mathrm{min}}$	-	0.05	
$V_{\mathrm{m}}/\dot{W}$	$\mathrm{m}^3/\mathrm{MW}_{\mathrm{el}}$	0.039	0.328

Table E.2: Outputs of the analytical optimisation procedure, for two regenerators (one employing helium, the other employing argon) with an effectiveness of 99 %.

		Helium-Helium	Argon-Argon
Parameter	Unit	Value	
N_s	-	$2.09 \cdot 10^{-3}$	
N_{s1}	-	$1.59 \cdot 10^{-3}$	$1.64 \cdot 10^{-3}$
N_{s2}	-	$0.50 \cdot 10^{-3}$	$0.45 \cdot 10^{-3}$
$N_{s\Delta T} = N_{s\Delta p} = N_{s\lambda}$	-	$0.70 \cdot 10^{-3}$	
D_1	mm	0.514	0.515
D_2	mm	0.164	0.151
L	mm	216	627
t_1	mm	0.026	0.026
t_2	mm	0.008	0.008
G_1	$\mathrm{kg}/\left(\mathrm{s} \cdot \mathrm{m}^2\right)$	1.42	4.71
G_2	$\mathrm{kg}/\left(\mathrm{s} \cdot \mathrm{m}^2\right)$	4.45	13.43
Re_1	-	42.1	126.1
Re_2	-	41.5	98.1
A_{*1}	-	0.404	
A_{*2}	-	0.404	
$A_{\mathrm{f}1}/\dot{W}$	$\mathrm{m}^2/\mathrm{MW}_{\mathrm{el}}$	0.34	1.00
$A_{\mathrm{f}2}/\dot{W}$	$\mathrm{m}^2/\mathrm{MW}_{\mathrm{el}}$	0.11	0.29
$\left(A_{\mathrm{f}} + A_{\mathrm{m}}\right)/\dot{W}$	$\mathrm{m}^2/\mathrm{MW}_{\mathrm{el}}$	0.63	1.82
$(\Delta p/p)_1$	%	0.13	0.14
$(\Delta p/p)_2$	%	0.042	0.047
ε	%	99	